Studies on Recombinant Protein and Peptides derived from Diphtheria Toxin

Thesis submitted by

MAHESH AGARWAL

For the award of the degree

of

Doctor of Philosophy

DEPARTMENT OF BIOSCIENCES AND BIOENGINEERING

INDIAN INSTITUTE OF TECHNOLOGY GUWAHATI

GUWAHATI - 781039, ASSAM, INDIA

OCTOBER, 2017

This thesis is dedicated to

my family

who inspired me to do this.

Department of Biosciences and Bioengineering

Indian Institute of Technology Guwahati

STATEMENT

I do hereby declare that the matter embodied in this thesis entitled "**Studies on Recombinant Protein and Peptides derived from Diphtheria Toxin**" is the outcome of research work carried out by me in the Department of Biosciences and Bioengineering, Indian Institute of Technology Guwahati, India, under the supervision of Dr. Biplab Bose.

In keeping with the general practice of reporting scientific observations, due acknowledgement has been made whenever work described here has been based on the findings of other investigators.

October, 2017

Mahesh Agarwal
(Roll No. 126106022)

Department of Biosciences and Bioengineering

Indian Institute of Technology Guwahati

Date: 20.10.2017

CERTIFICATE

This is to certify that the thesis entitled "**Studies on Recombinant Protein and Peptides derived from Diphtheria Toxin**", is being submitted by **Mahesh Agarwal (Roll No. 126106022)** for the award of degree of Doctor of Philosophy is an authentic record of the results obtain from the research work carried out under my supervision in the Department of Biosciences and Bioengineering, Indian Institute of Technology Guwahati, India.

The results embodied in this thesis have not been submitted to any other University or Institute for the award of any degree.

October, 2017

Dr. Biplab Bose

(Research Supervisor)

Acknowledgements

I would like to thank all the people bestowed in some sense to mention the work in this thesis. Foremost, I would like to express my sincere gratitude to my thesis advisor Dr. Biplab Bose for his outstanding support during the Ph.D. study. I have learned many new things from him. His door was always open whenever I had questions about my research and writings. I am thankful to him for giving me the opportunity to work in diverse exciting projects. He has also supported me to attend various conferences and engaged me with new research ideas. Because of him, I was fortunate to work on state of the art facility, center for excellence (DBT Program Support Laboratory), Department of Biosciences and Bioengineering, IIT Guwahati.

Additionally, I am extremely thankful to my doctoral committee member Prof. K. Pakshirajan, Prof. S.S.Ghosh and Dr. L.M. Kundu for their valuable suggestions. I am grateful to these members for their patience and encouragement to overcome obstacles facing through my research.

I am very grateful to our collaborator, Dr. Bhubaneswar Mandal and his student Tanmay Mondal at Department of chemistry, IIT Guwahati for their remarkable experimental support. A special note of thanks to Dr. Amaresh Kumar Sahoo for his unconditional support in my work. I gained a lot from his vast knowledge of nanotechnology and scientific curiosity.

I would like to acknowledge present and past HODs of the department, Prof. K. Pakshirajan, Prof. Venkata Dasu Veeranki, Prof. A. Goyal and Prof. P. Goswami for developing excellent instrumental facility and research environment. Organization of regular Bio-Talk helps me to interact with the scientific community. My sincere thanks to Prof. G. Krishnamoorthy, Head of the central instrumentation facility for giving me an opportunity to work as AFM operator and also allowed me to use sophisticated instruments.

I express my profound gratitude to my seniors Dr. Ashok Kumar and Dr. Pojul Loying for their guidance, support, and inspiration. They are the solid source of practical scientific knowledge. Thank you for troubleshooting many of my experimental problems. I also extend thanks to Dr.

Thyagrajan, Dr. Archita, Dr. Manab, Dr. Mithun, Dr. Ankana, Dr. Priyamvada for their helping hands.

I would like to thank my fellow lab mates Poulami Datta, Namami Goswami, Vimalathian, Satendra, Yashwant for their feedback, cooperation, and friendship. I also continue thanks to all my friends Sandipan, Poulami, Priya, Aseif, Neha, Anil, Srirupa, Sanjeev, Babina, Navin, Sayan, Balajee, Gaurav, Rahul.

A special gratitude goes to MHRD for institute fellowship and SERB-DST for funding my international conference. I express my gratitude to the departmental and institutional staff for their cooperation and friendly behavior throughout my Ph.D.

I am highly thankful to my M.Sc supervisor, Dr. Arun Kumar Dhaylan for motivating me to do biological research. I also want to acknowledge all my mentors and teachers who taught me reading and writing during the education journey.

I am grateful to family members and friends who have provided me with moral and emotional support in my life.

Thanks to God, the Almighty, for showers of blessings to complete the research work successfully.

October, 2017 ***Mahesh Agarwal***

Contents

Abbreviations

ANOVA	Analysis of variance
bp	Base pair
BSA	Bovine serum albumin
BSA-NPs	BSA-coated Nanoparticles
CD	Circular Dichroism
CMA	Contact map analysis
DT	Diphtheria toxin
DAPI	4', 6-Diamino-2-phenylindole dihydrochloride
DEPC	Diethyl pyrocarbonate
DLS	Dynamic light scattering
DMEM	Dulbecco's Modified Eagle Medium
DMSO	Dimethyl sulfoxide
DNA	Deoxyribonucleic acid
dNTP	Deoxyribonucleotide triphosphate
EDTA	Ethylene-diamine-tetraacetic acid
EDC	1-ethyl-3-(3-dimethylamino-propyl)carbodiimide hydrochloride
ELISA	Enzyme-linked immunosorbent assay
EGF	Epidermal growth factor
EGFR	Epidermal growth factor receptor
ERK	Extracellular signal-regulated kinase
FBS	Fetal bovine serum
FESEM	Field Emission Scanning Electron Microscopy
FITC	Fluorescein isothiocyanate
FT-IR	Fourier-transform infrared spectroscopy

HB-EGF	Heparin-binding epidermal growth factor
HPLC	High performance liquid chromatography
h	Hour
HRP	Horseradish peroxidase
IPTG	Isopropyl β-D-thiogalactopyranoside
kDa	Kilodalton
K_a	Association rate constant
K_d	Dissociation rate constant
K_D	Dissociation constant
KLD	Kinase, Ligase, *Dpn I*
MAPK	Mitogen-activated protein kinases
MBP	Maltose binding protein
mg	Milligram
min	Minutes
ml	Milliliter
mM	Millimolar
MTT	3-(4,5-Dimethylthiazol-2-yl)-2,5-diphenyl-tetrazolium bromide
NHS	N-hydroxysuccinimide
ng	Nanogram
nm	Nanometer
nM	Nanomolar
NPs	Nanoparticles
OPD	O-phenylenediamine dihydrochloride
PBS	Phosphate buffered saline
PCR	Polymerase chain reaction
PI3K	Phosphatidylinositol 3-kinase
PLGA	Poly (D,L-lactide-co-glycolide)
PMSF	Phenylmethanesulfonylfluoride

PDB	Protein database
PVA	Polyvinyl alcohol
PVDF	Polyvinylidene fluoride
RDT	Receptor-binding domain of Diphtheria toxin
RDT-NPs	RDT-coated Nanoparticles
Rg	Radius of gyration
RIPA	Radioimmunoprecipitation assay
RMSD	Root means square deviation
RMSF	Root means square fluctuation
RNA	Ribonucleic acid
rpm	Revolutions per minute
RT	Room temperature
RU	Response unit
SDS-PAGE	Sodium dodecyl sulfate polyacrylamide gel electrophoresis
SPR	Surface Plasmon Resonance
TEM	Transmission electron microscopy
Tf-FITC	Transferrin-FITC
µg	Microgram
µl	Microliter
µM	Micromolar

Abstract

Diphtheria toxin (DT) is a well characterized AB-toxin with three independent domains: C-domain for catalysis and toxicity, T-domain for translocation through the membrane and R-domain or receptor-binding domain. The toxicity of DT has been investigated extensively and is utilized to create therapeutic agents, like immunotoxins, which kill cells. However, the receptor-binding ability of DT is not extensively explored and used for therapeutic purposes.

The receptor of DT is Heparin-binding EGF-like growth factor (HB-EGF). It is expressed as a membrane-bound molecule, which is eventually released by ectodomain shedding. HB-EGF is a growth factor. It is overexpressed in various cancer cells and activates different oncogenic signaling pathways. Therefore, HB-EGF on the cell surface can be targeted for cell-specific drug delivery. It can also be targeted to modulate its oncogenic signaling.

In the current work, we have manipulated the receptor-binding domain of Diphtheria toxin (RDT) in two ways. First, we have used recombinant RDT to deliver drug-loaded nanoparticles to specific cells that express Human HB-EGF. In the second part, we have established that a short stretch of 26 amino acids in RDT is adequate for binding to HB-EGF with moderate affinity.

We have synthesized polymeric PLGA nanoparticles (NPs) and coated those with recombinant RDT. These RDT-coated NPs (RDT-NPs) were characterized by TEM, SEM, DLS, FTIR, and ELISA. Using flow cytometer and spectrofluorimetry-based experiments, we show that RDT-NPs has enhanced uptake in cells expressing human HB-EGF and such uptake involve Clathrin-dependent receptor-mediated endocytosis. We further show that this receptor-targeted delivery through RDT-NPs increases the potency of a chemotherapeutic agent.

Subsequently, we have attempted to create RDT-derived peptides that would bind to HB-EGF. Such peptides can be utilized for HB-EGF-targeted drug delivery or to modulated HB-EGF signaling. We analyzed the structure of RDT and identified a stretch of 26 amino acids that is crucial for binding to HB-EGF. Based on such structural information, we designed three 26 amino acid long peptides. We performed docking and molecular dynamic simulations to understand possible structural features and the receptor-binding ability of these peptides. We synthesized these peptides by solid phase synthesis and characterized those through several techniques like ESI mass spectrometry, and CD spectroscopy. Subsequently, we show that these peptides bind to HB-EGF. Further, we expressed these peptides in *E. coli* as MBP-tagged peptides. All three MBP-tagged peptide retained HB-EGF binding, and SPR-based analysis showed that these MBP-tagged peptides bind to HB-EGF with moderate affinities.

1 Introduction

Almost 130 years back, Diphtheria toxin (DT) was discovered. Since then, extensive work has been done to understand its structure, and function. Diphtheria toxin binds to its receptor and enters a cell through receptor-mediated endocytosis. Subsequently, it kills the cells by blocking protein synthesis. This old foe was turned into a friend when it was used to create an immunotoxin against cancer cells.

The toxicity of Diphtheria toxin has been used to create several immunotoxins. However, the receptor-binding ability of Diphtheria toxin remains mostly unexplored for therapeutic purposes. Interestingly, the receptor of Diphtheria toxin, HB-EGF, is a growth factor and is expressed in a membrane-bound form. HB-EGF is highly expressed in different types of cancer cells, including glioma, gastric, liver, and pancreatic cancer. Therefore, HB-EGF is a good target for therapeutic purposes. Targeting HB-EGF can attain two objectives: targeted drug delivery and blocking of oncogenic signaling of HB-EGF. HB-EGF can be targeted using antibodies against it. However, one can also use Diphtheria toxin or its fragment for targeting HB-EGF. It has been earlier shown that the receptor-binding domain of DT is non-toxic and binds to HB-EGF with high affinity, even in the absence of other domains of the toxin.

In current work, the receptor-binding domain of DT (RDT) is used as a receptor-targeted homing agent for drug-loaded polymeric nanoparticles. We have shown that coating with RDT increases cellular uptake of PLGA NPs. Further, we have shown that RDT-coated NPs are internalized through Clathrin-dependent, receptor-mediated endocytosis in HB-EGF-expressing cells. RDT-coated NPs showed cell specific, enhanced potency of the drug loaded in the NPs. Based on structural information of DT-HB-EGF complex, we have designed a short peptide and its variants that bind to HB-EGF. These peptides were fused to a large protein, MBP, to create recombinant MBP-tagged peptides. These MBP-tagged peptides showed moderate binding affinity with HB-EGF. Moreover, we have demonstrated that these MBP-tagged peptides can modulate the mitogenic effect of HB-EGF.

This thesis is organized into several sections. After this introductory chapter, the Review of Literature is presented in chapter 2. In this chapter, prior research works related to Diphtheria toxin and its uses in therapeutics are described. Chapter 3 consists of the Materials and Methods with details of experimental protocols used in this work. The Results and Discussions are presented in Chapter 4. This chapter is further divided into two sections. The first section deals with the use of the receptor-binding domain of Diphtheria toxin for targeted drug delivery. The second section illustrates the design of short peptides from Diphtheria toxin for receptor binding. The conclusions drawn from present work, along with future scopes are discussed in Chapter 5. The supplementary information on common reagents, experimental kits, and cells used for various experiments are given in the Appendix at the end of the thesis.

2 Review of Literature

2.1 Diphtheria Toxins: Structure and function

Diphtheria toxin is an exotoxin secreted from pathogenic bacterium, *Corynebacterium diphtheria.* DT inhibits eukaryotic translation protein machinery by inactivating elongation factor 2 (EF-2) (1). It is a globular protein composed of a single polypeptide chain of 535 amino acid residue with approx. molecular weight of 63 kDa. DT is synthesized as single, intact proenzyme having two fragments connected by a loop containing a proteolysis site and a disulfide bond. DT is activated by the proteolytic nicking of the polypeptide and reduction of disulfide bonds (2).

DT is an AB type toxin in which subunit A has catalytic function and subunit B has receptor binding ability (3). DT consists of three distinct domains: (1) N-terminal catalytic domain (C, 1-190 residues) with ADP-ribosyltransferase enzymatic activity; (2) Central trans-membrane domain (T, 191-379 residues) that facilitates translocation of catalytic domain into the cytoplasm; (3) C-terminal receptor binding domain (R, 379-535 residues) (4). Subunit A consists of C-domain and Subunit B carries two domains: T-domain and R-domain (5). The structure of DT is shown in Figure 2.1.

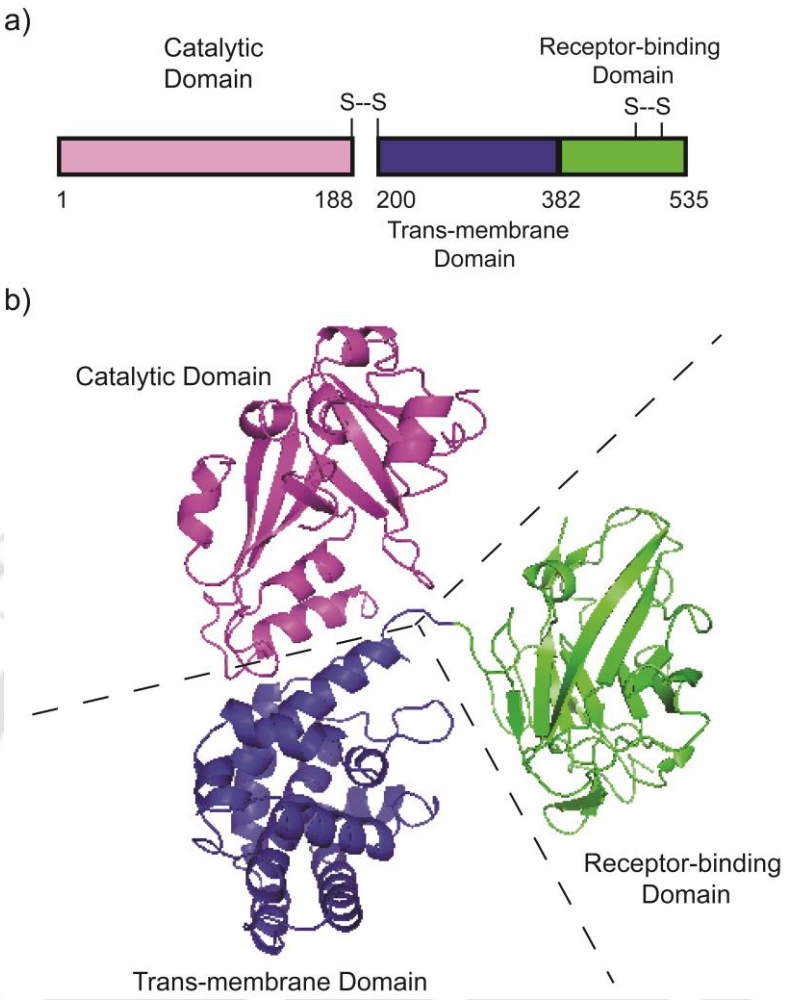

Figure 2.1: Structure of Diphtheria toxin (DT). (a) Schematic diagram showing different parts of DT. DT has three domains, a catalytic (1-188 a.a residues), a trans-membrane domain (200-382 a.a residues) and a receptor-bonding domain (382-535 a.a residues). (b) Ribbon diagram of X-ray crystal structure of DT (PDB ID: 1F0L).

The mechanism of cell killing by DT involves four distinct steps (Figure 2.2). The receptor of DT is cell surface bound Heparin-binding EGF-like growth factor (HB-EGF) (6). HB-EGF is a growth factor. It is expressed as a membrane-bound form (pro-HB-EGF) and is subsequently released by ectodomain shedding (7).

DT binds to membrane-bound pro-HB-EGF and internalized through receptor-mediated endocytosis (3). The endosomal vesicle causes structural changes in DT due to an acidic environment. The translocation domain gets inserted into the endosomal membrane facilitating

passage of catalytic domain across cell membrane (8). Subsequently, C-domain catalyzes the transfer of an ADP-ribosyl group from NAD^+ to a specifically modified histidine (diphthamide) on the elongation factor (EF-2) (9). This halts protein synthesis causing cell death.

Each domain of DT has independent functions. The R-domain of DT mediates the binding of diphtheria toxin to its cell surface receptor, HB-EGF. This binding may be facilitated by the diphtheria toxin receptor associated protein 27, DTRAP 27, a homolog of human CD9 antigen (10). The DT bound HB-EGF is concentrated in Clathrin-coated pits and internalized into Clathrin-coated vesicles (CCVs), which are then converted into early endosomal vesicles (11). Another protein components, including Arf-1 and COPI complex, replace the Clathrin triskeleton and pH of vesicles is lowered. Acidification of vesicle lumen causes the dynamic unfolding of the transmembrane domain (T-domain) which allows its insertion into the endosomal vesicle membrane forming a pore (12). Then, C-domain is translocated from the cis (luminal) to trans (cytosolic) side of the early endosomal vesicles membrane. Still, the precise mechanism of translocation event is not known. But, it is a hypothesis that translocation of C-domain through the pore is facilitated by a Cytosolic Translocation Factor (CTF) complex (13). Another hypothesis suggested that nascent chaperone-like activity of the partially unfolded T-domain mediates the translocation (14). Translocation is followed by reduction of disulfide bond between fragment A and B result in release of C-.domain into the cytoplasm (15). In cytosol, C-domain regains enzymatically active conformation and catalyzes the NAD+-dependent ADP-ribosylation of elongation factor 2 (EF-2). This inhibits protein synthesis causing cell death (16). The mechanism of action of DT is shown in Figure 2.2.

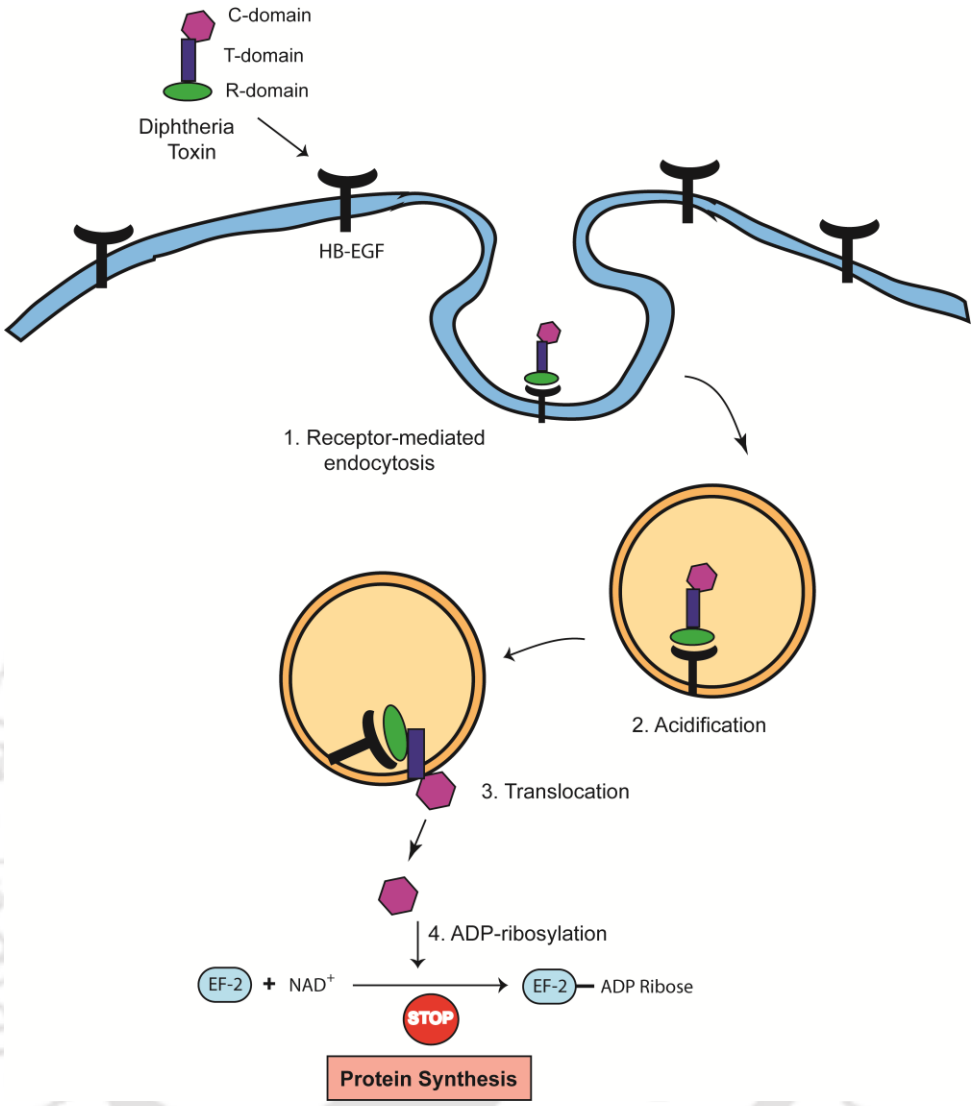

Figure 2.2: Mechanism of action of DT. (1) DT binds to cell surface HB-EGF through R-domain and gets internalized into cell by receptor-mediated endocytosis. (2) Subsequently, acidification in endosome causes structural change in DT (3) Translocation of C-domain is facilitated by T-domain (4) C-domain catalyzes ADP ribosylation on EF-2. This inhibits protein synthesis and leads to cell death.

2.2 HB-EGF as therapeutic target

Cell surface Heparin-Binding EGF like Growth Factor (HB-EGF) is the receptor of DT. It is a growth factor which synthesized as a membrane-bound molecule and subsequently released by ectodomain shedding in soluble form (17). HB-EGF binds to EGFR/ErbB1/HER1 and

ErbB4/HER4 and activates downstream signaling pathways (18). Low expression of HB-EGF is found in some normal adult tissues like brain, heart, lung and skeletal muscle (19). HB-EGF plays important role in several biological functions such as skin wound healing, blastocyst implantation, eyelid formation, and heart development (20-23). HB-EGF is overexpressed in various kinds of cancer such as pancreatic, glioma, breast, gastric, colon and liver cancer (24-29). The different clinical studies show that HB-EGF is also involved in the progression of atherosclerosis, tumor formation, metastasis, and drug resistance (30, 31). Specifically, targeted inhibition of HB-EGF emerged as a potential therapeutic target to suppress the tumor progression.

HB-EGF can be used as a dual target: (1) blocking mitogenic signaling pathway and (2) specific delivery of payloads to HB-EGF overexpressing cells. The anti-HBEGF monoclonal antibodies (Y-142) have been developed against HB-EGF to inhibit cell proliferation and angiogenesis (32). *In vivo* study shows anti-HB-EGF chimeric antibody, cKM3566, is effective against ovarian cancer (33). Anti-HBEGF antibody modified liposomes (Immunoliposomes) were developed for enhance and specific delivery of drug for the effective treatment of breast cancer (34, 35). Okamoto A *et al.* have developed lipid nanoparticles (LNP) encapsulating siRNA and surface modified with Fab' fragments of anti-HB-EGF antibody for targeted therapeutics (36).

2.3 Structure and interaction partners of HB-EGF:

HB-EGF is glycosylated EGF family member having 208 amino acid residues with apparent molecular weight 22 kDa. It is synthesized as a single peptide type I transmembrane protein (pre-proHB-EGF) consisting of N-terminal signal peptide domain (1-23 aa), a propeptide domain (24-62 aa), mature HB-EGF domain (63-149 aa), juxtamembrane domain (150-160 aa), a transmembrane domain (161-184 aa) and a short cytoplasmic domain (185-208 aa) (37). The domain architecture of HB-EGF is shown in Figure 2.3.

The mature HB-EGF consists of heparin-binding domain and EGF like domain. Similar to another member of EGF family, HB-EGF has a highly conserved six cysteine residue which forms three intermolecular disulphide bonds. ProHB-EGF functions as the cellular receptor for diphtheria toxin, mediating the entry of that toxin into the cytoplasm (38). proHB-EGF associates with tetraspanin CD9 and integrin-α3β1 (39). Thus, proHB-EGF plays an important role in direct cell–cell communication in a juxtacrine manner.

The membrane-bound form of HB-EGF (proHB-EGF) cleaved at the juxtamembrane domain by metalloproteinases, including the matrix metalloproteinases (MMPs) and members of the ADAM (disintegrin and metalloprotease) family (40). This results in the shedding of soluble ectodomain HB-EGF (sHB-EGF) (41). This proteolytic cleavage process is called 'ectodomain shedding'. HB-EGF binds to and activates ErbB1 and ErbB4 (42). HB-EGF has a high affinity for heparin and heparin sulfate proteoglycans (HSPG) (43). HSPGs act as co-receptors for HB-EGF and modulate HB-EGF bioactivity. sHB-EGF can also bind to N-arginine dibasic convertase (NRD1), a cell-surface-associated enzyme that involves in cell migration (44). sHB-EGF is a potent mitogen and chemoattractant for several cell types, including vascular smooth-muscle cells, fibroblasts, and keratinocytes (43). Both proHB-EGF and sHB-EGF can bind to diphtheria toxin (2, 10).

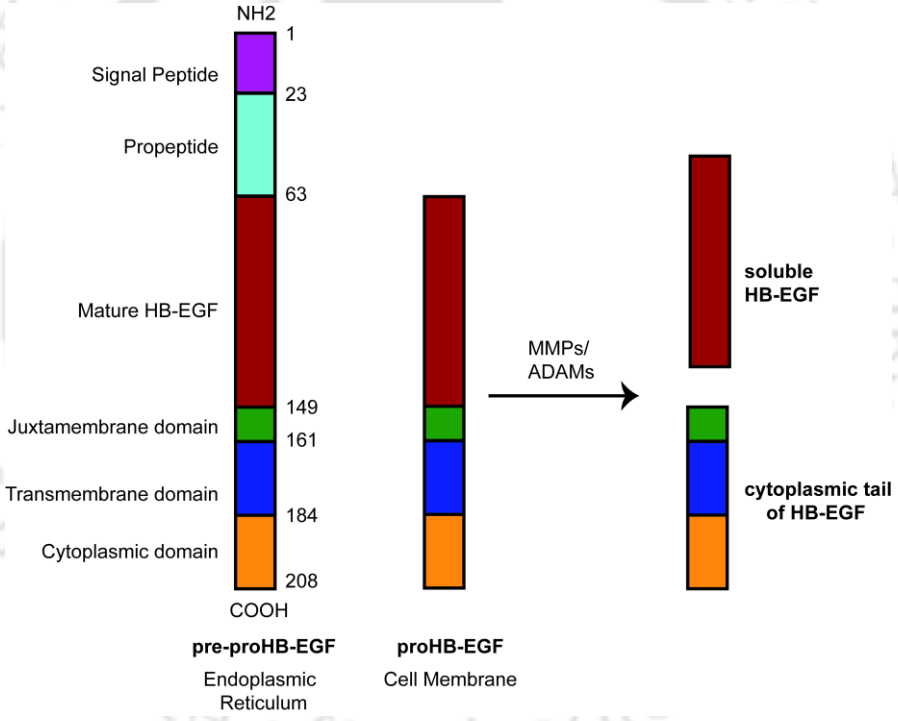

Figure 2.3: Basic structure and processing of HB-EGF. The precursor HB-EGF consists of N-terminal signal peptide domain (1-23 aa), a propeptide domain (24-62 aa), mature HB-EGF domain (63-149 aa), juxtamembrane domain (150-160 aa), a transmembrane domain (161-184 aa) and a short cytoplasmic domain (185-208 aa). The membrane-bound form of HB-EGF (proHB-EGF) cleaved by metalloproteinases or ADAMs family results in ectodomain shedding of sHB-EGF.

2.4 Role of HB-EGF in physiological and pathological processes:

The several mutant mice lacking HB-EGF expression have shown that HB-EGF plays an essential role in various physiological and pathological processes in conjunction with ErbB receptors. It is involved in skin wound healing, kidney collecting-duct morphogenesis, heart development and function, eyelid closure, blastocyst implantation, lung development, atherosclerosis, glomerulonephritis, and tumor formation in ovarian cancer (20, 22, 31, 45-50).

HB-EGF is found in wound fluid and is involved in stimulation of fibroblast and keratinocyte growth in *in vivo* model (51). It is an essential growth factor for epithelialization in skin wound healing and renal epithelial cell survival (20, 52). HB-EGF induces expression of the vimentin, a mesenchymal protein and decreased expression of E-cadherin, an epithelial protein in keratinocytes which promotes cutaneous wound healing (53). In synergy with TGF-α, HB-EGF activates EGFR and ERK pathways that are required for epithelial cell migration during eyelid closure in mice embryos (22). HB-EGF plays a predominant role in the maintenance of homeostasis in the adult heart, development of cardiac valve and myocardial remodeling (46, 54). The HB-EGF null mice exhibit enlarged size of cardiomyocytes, ventricular dilation, myofiber hypertrophy and signs of severe cardiac dysfunction (23). Recent studies showed HB-EGF induced heart fibrosis and proliferation of cardiac fibroblasts occurs through activation of the Akt/mTor/p70s6k pathway (19). HB-EGF suppresses distal lung cell proliferation and involved in perinatal distal lung development (48). HB-EGF is an important growth factor for successful implantation since it involved in the interaction between the blastocyst and uterus. HB-EGF is expressed in the uterine luminal epithelium at the site of the blastocyst and facilitates cell-cell interaction between endometrium and conceptus during embryo implantation. (21). HB-EGF expression is upregulated in myogenesis. A DNA binding transcription factor, MyoD activates HB-EGF expression in skeletal muscle cell differentiation (55). HB-EGF is expressed in the ureteric bud of embryonic kidneys and induces branching of tubulogenesis in ureteric bud cells. In cooperation with TGF-α, HB-EGF involve in morphogenesis of the collecting duct system in developing kidneys (45). HB-EGF is involved in several blood vessel physiologies. Phenylephrine-induced

cell growth and endothelin-1-induced vasospastic contraction are impaired in HB-EGF-lacking arteries (55, 56). These processes are regulated by GPCR-dependent EGFR-transactivation through HB-EGF shedding. HB-EGF is also involved in other non-cancerous pathological processes. It plays an important role in the development and invasiveness of cholesteatoma (57). HB-EGF is expressed in glomerular epithelial cells (podocytes) and causes rapidly progressive glomerulonephritis, renal failure and kidney dysfunction (49). HB-EGF is a potent antiapoptotic protein that allows cells or tissues to survive hypoxic, oxidative, and nutritional stresses. It has been investigated that HB-EGF has a therapeutic role in Intestinal ischemia/reperfusion (I/R) injury (58).

HB-EGF is also involved in genesis and progression of cancer. In cancer, HB-EGF is involved in cell proliferation, migration, and tumorigenesis (30). HB-EGF is highly expressed in various kinds of cancer including glioblastoma, breast, pancreatic, gastric, ovary and colon (59). A soluble form of HB-EGF induces expression of metalloproteases such as MMP-9 and MMP-3 and leads to enhanced cell migration. sHB-EGF stimulates tumor growth and exert an angiogenic effect but pro-HB-EGF fail to do so (31). HB-EGF is involved in epithelial-mesenchymal transition in gastric pancreatic and ovarian cancer (57, 60, 61). It has been reported that chemotherapeutic drugs induce ectodomain shedding of HB-EGF in colon cancer. A chemotherapeutic drug, SN-38, upregulates HB-EGF shedding through activator protein-1 (AP-1) and NF-kappaB activation. This results in EGFR activation and apoptotic resistance to chemotherapy (62). The inhibition of ectodomain shedding of HB-EGF results in the upregulation of E-cadherin through inhibition of ZEB1, a transcriptional repressor of E-cadherin. This leads to cellular morphologic changes, decreased cell motility and enhanced apoptotic sensitivity in response to EGFR-inhibitor treatment in pancreatic cancer cells (57).

2.5 Signaling pathways of HB-EGF:

A different EGF family member binds to and activates ErbB receptor ligands. The ErbB family of receptor tyrosine kinases (RTKs) consists of four receptors: EGFR/ErbB1/HER1, ErbB2/HER2/neu, ErbB3/HER3, and ErbB4/HER4. HB-EGF binds to and activates EGFR (ErbB1) and ErbB4 directly (42, 63). HB-EGF activates Ras/Erk-MAP kinase and PI3K/Akt pathways that are involved in growth, proliferation, and survival (Figure 2.4) (64).

When HB-EGF binds to ErbB receptor, it results in dimerization, following autophosphorylation of specific tyrosine residues within their cytoplasmic domains that mediate intracellular signaling cascades (65). The phosphorylated receptor interacts with an adaptor protein, Grb2 (Growth factor receptor-bound protein 2) through SH2 (Src Homology 2) domain and recruits another protein SOS (son of sevenless) to activate RAS (66). The exchange of GDP with GTP by SOS causes a conformational change in RAS, which turns on RAS activity (67). Activated RAS binds to N-terminal domain of RAF-1 (cRAF), a Ser/Thr kinase. RAF-1 binds to and phosphorylated MEK, a Tyr/Ser kinase which further activates ERK or MAP kinase, a Ser/Thr kinase (68). ERK or MAP kinase phosphorylates variety of proteins present in cytosol and nucleus that mediate diverse cellular responses. In cytosol, it can activate RSK1 (p90 ribosomal S6 kinase 1) and in nucleus, it can activate different transcription factors such as ELK-1, ETS, SP-1, c-FOS and c-JUN (69). These transcription factors play critical role in promoting cell growth, survival, and proliferation.

HB-EGF also activates PI3K-Akt signaling pathway. Ras-GTP then activates the p110 subunit of PI3K (70). The activated PI3K catalyzes phosphorylation of Phosphatidylinositol (4,5) bisphosphate (PIP2) to form Phosphatidylinositol (3,4,5) trisphosphate (PIP3). PIP3 binds Akt (Protein kinase B) and PDK1 for translocation of Akt to membrane. The multiple proteins including PDK2, ILK, mTORC, DNA-PK are involved in activation of Akt (70). Activated Akt phosphorylates wide range of intracellular proteins which involved in cell survival, growth, proliferation, cell migration and angiogenesis. The activated Akt regulates some transcription factor such as degradation of IκB and nuclear translocation of NF-κB and promotes expression of caspase inhibitors, c-Myb and Bcl-xL (71, 72). Akt promotes G1-S phase cell cycle progression by phosphorylating and inactivating glycogen synthase kinase 3 (GSK-3). This prevents the phosphorylation and degradation of cyclin D1 (73).

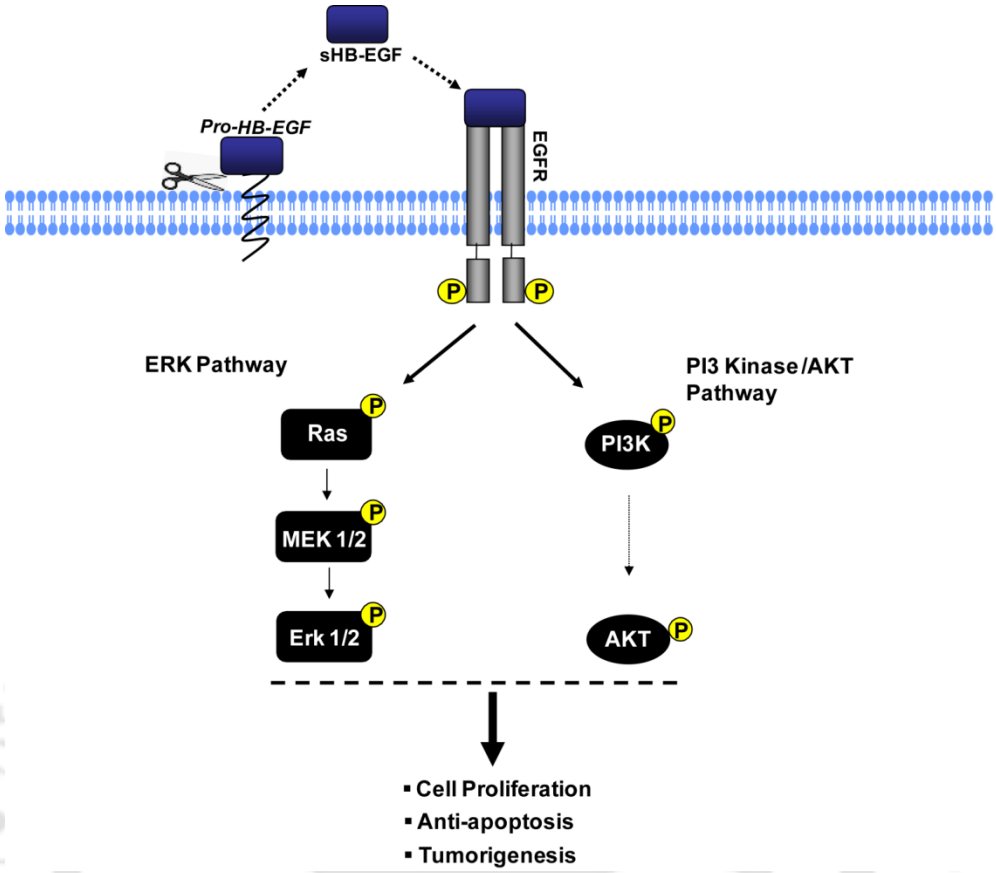

Figure 2.4: HB-EGF activates MAPK and AKT signaling pathway. HB-EGF binds and activates EGFR. Trans-activation of EGFR further activates Erk1/2 and Akt. These pathways are involved in cell proliferation through regulation of cell cycle.

2.6 DT in therapeutics:

The toxicity of Diphtheria toxin has been used to develop therapeutic molecules. DT has been fused to antibodies or some other homing protein to achieve targeted toxicity. In such molecules, either the C-domain of DT is used or the R-domain is mutated to prevent binding of DT to its receptor.

In diseased condition, specific growth factor receptors/antigens are overexpressed on the cell surface. Antibodies recognizing these receptors/antigens can be conjugated to modified toxins called immunotoxins. These immunotoxins can be used for targeting such receptors. Bacterial toxins (Diphtheria toxins and Pseudomonas exotoxin), Plant toxins (Ricin and the ribosome inactivating proteins) are commonly used for development of immunotoxins.

The first targeted toxin, DAB389-IL-2 was developed by fusion of a mutated DT and interleukin-2 (IL2) targeting the CD25 subunit of the IL2 receptor (74, 75). This cytotoxin is approved by FDA for the treatment of a human cutaneous T cell lymphoma (CTCL) (76). A point mutated DT (CRM107) is coupled with human transferrin has shown the cytotoxic effect in metastatic brain tumor in early clinical trials (77). Diphtheria toxin based anti-CD3 immunotoxins were developed for the various clinical applications including autoimmune disease therapies, T-cell leukemias, and organ transplantation (78). An Immunotoxins, LMB-2 was developed by conjugating antibody molecule (recognizing CD25) to the toxin produced by *Pseudomonas* bacteria. This immunotoxin is used for the treatment of hairy cell leukemia (79). Similar immunotoxin, BL22 targets the CD22 cell surface receptor, used for the treatment of lymphomas (80). Immunotoxins face some challenging problem such as immunogenicity, undesired toxicity and limited half-life (81).

Though toxicity of DT has been utilized for developing therapeutic molecules, receptor binding ability of DT remains under-utilized. Receptor binding ability of DT can be used in therapeutics in two ways: a) it may be used to achieve targeted delivery of drugs to cells overexpressing HB-EGF and b) it may be used to bind soluble HB-EGF and block its signaling.

A single G-to-E transition at 52 positions is present within fragment A of DT in CRM197. This mutation causes loss of ribosyltransferase activity, may be due to alteration of NAD^+ binding site (82). CRM197 maintains the secondary structure and bind to HB-EGF (83). A non-toxic mutated Diphtheria toxin, CRM197 was utilized for both targeting payloads and to block HB-EGF signaling.

CRM197 was already used to modify the surface of polymeric nanoparticles and liposomes for delivering drug to brain. Targeting to brain or central nervous system is possible via HB-EGF, an endogenous transport receptor in the blood–brain barrier (84). An *in vivo* study shows loperamide loaded PLGA nanoparticles were modified with CRM197 has potential of targeted drug delivery in central nervous system (85). In another study, zidovudine (AZT) loaded polybutyl-cyanoacrylate nanoparticles modified with CRM197 has capability to across blood–brain barrier (86). The cardiolipin containing liposomes was synthesized and surface modified with CRM197 to carry neuron growth factor across the blood–brain barrier for treatment of neurological diseases (87). CRM197 is also utilized for delivery of small interfering RNAs (siRNAs). The RNA interference allows to specifically knowndown of overexpressing gene in diseased conditions. Polyethylenimine is a carrier for efficient nucleic acid delivery. Pleiotrophin

growth factor is overexpressed in tumor cells including glioblastoma. Höbel *et al.* used polyethylenimine/siRNA complex modified with CRM197 to target overexpressing pleiotrophin growth factor into glioblastoma cells (88).

DT causes cytotoxicity through catalytic domain whereas only receptor binding domain of DT (RDT) is non-toxic. Only RDT can also be used for targeted therapeutics. Previously, our lab has shown RDT binds to HB-EGF with a similar dissociation constant of full-length DT. The RDT-curcumin complex showed enhance cellular uptake in HB-EGF overexpressing human glioblastoma cells (89).

Apart from targeted therapeutics, CRM197 and RDT were also utilized for blocking HB-EGF signaling. A non-toxic mutated form of diphtheria toxin, CRM197 has shown reduced cell proliferation and antitumor effect in oral cancer (83). Intravenous administration of CRM197 in mice has shown anti-tumor effect for triple-negative breast cancer (90). It has been shown that CRM197 can reverse resistance to chemotherapeutic agents such as paclitaxel and cisplatin in chemo-resistant ovarian carcinoma cell line (91, 92). Thus, CRM197 is effective in treatment of HB-EGF targeted chemoresistance ovarian carcinoma which overexpresses HB-EGF (93). The combination of CRM197 with shRNA interference of vascular cell adhesion molecule-1 (VCAM-1) inhibited the growth, migration, invasion, and apoptosis of glioblastoma cells (94). Doxorubicin enhances the expression of both HB-EGF and EGFR. The combination of CRM197 and doxorubicin increased the cytotoxicity in a T-cell acute lymphoblastic leukemia (95).

Several mutants of CRM197 and R-domain were created for higher binding to HB-EGF. Recently, a more potent DT mutant than CRM197 was developed. A point mutation in R-domain (R460H) of CRM197 has higher affinity to HB-EGF than wild-type CRM197. This R-domain mutant suppresses cell proliferation through HB-EGF more effectively than wild-type R domain (96). Gillet et. al have mutated several amino acids (Y380K, Q387E, L390T, A395T, F389Y, and G510A) in the R-domain of Diphtheria toxin and created a recombinant R-domain of DT (DTR8) that has higher binding affinity than CRM197 (97). These mutants are involved in inhibition of HB-EGF signaling. Therefore, it can be used for the treatment of diseases associated with activation of the HB-EGF/EGFR pathway. In R-domain of DT, some amino acid residues are found to be critical to binding with receptor. It has been reported that K516 and F530 of DT play a critical role in receptor recognition (98). Additionally, mutations at these sites, K516A and F530A exhibit receptor-blocking activity. In the region between S516 and F530 of DT, four other

residues (Tyr-514, Val-523, Asn-524, and Lys-526) are involved in receptor binding (98). A short peptide corresponding to this region can be further studied for the therapeutics applications.

2.7 Drug delivery system

In conventional drug delivery system, therapeutic agents are distributed non-specifically in a body through the systemic blood circulation. As a result, most of the drugs are not reached to the affected body site. In case of chemotherapy, 99% of anti-cancer drugs do not reach at target body site and affect normal cells too. Moreover, traditional drugs have several limitations such as rapid degradation and clearance of drugs, poor bioavailability, low-water solubility, and side effects result in normal healthy cells through nonspecific accumulation (99). A newly engineered drug formulation may be an effective technique to combat these problems.

The targeted drug delivery system believed to more effective by reducing side effects. These systems can be used to deliver drug at a particular site. The numerous fundamental studies and molecular understanding granted discovery of important pathway in cell biology. These pathways opened the door for newer drugs for disease treatment. Delivery of carriers to target cells could be done by passive and active targeting.

In passive targeting, drug carrier circulates systemically in blood for longer time period. In tumor cells, endothelial lining of blood vessel wall is more permeable than normal cells. As a result, more drug-loaded particles accumulate around the tumors. This is called enhanced permeation and retention (EPR) effect (100). The majority of administered drug particles accumulate at undesired sites of the body. So, it can't be considered as selective targeting.

The specific ligand–receptor interaction between drug/drug carrier and the target cells is called active targeting. Receptor-mediated delivery is an effective strategy to specifically deliver therapeutics to the defined target cells. The receptor-targeted delivery mechanism utilizes small ligands, antibody, peptides or toxins which are chemically or physically conjugated with drugs. The ligand, antibody or the peptides are recognized by the specific cell surface antigens/receptors and are internalized via receptor-mediated endocytosis. The drugs or the toxins exert their cytotoxicity activity and kill the specific cells without causing any toxic effects to the normal, healthy cells (101). The schematic diagram of passive and active targeting is shown in Figure 2.5.

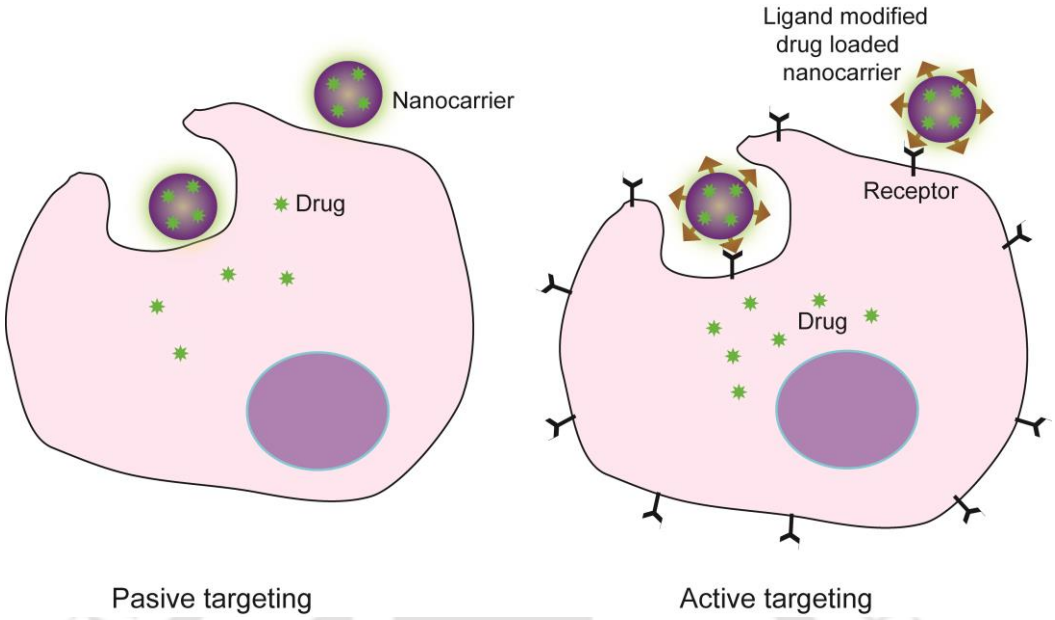

Figure 2.5: Drug delivery system. In passive targeting, drug carrier circulates systemically for longer time period. Active targeting is the specific ligand–receptor interaction between drug/drug carrier and the target cells. Here, delivery of drug carrier is enhanced and specific to a target site.

Drug nanocarrier

Nanocarriers provide stability to drugs so that drugs can be delivered to inaccessible sites around the body. It also helps in the effective delivery of hydrophobic drug in the body. Nanocarriers include lipid based carriers (liposomes, micelles), dendrimers, magnetic nanoparticles, gold nanoparticles, polymeric nanoparticles, etc.(102). These nanocarriers are biocompatible and help in the easy conjugation of ligands without changing the biological property for targeted therapy. The diagrammatic representations of these nanocarriers are shown in Figure 2.6.

A liposome is a spherical vesicle having aqueous solution core surrounded by a hydrophobic membrane. It is composed of mainly phospholipid and can be loaded with hydrophobic and/or hydrophilic molecules. Liposomes are promising drug delivery carrier due to property of biodegradable, biocompatible and non-immunogenic (103). An FDA approved, Doxorubicin entrapped in pegylated liposomes (Doxil) are used to treat some cancer including metastatic ovarian cancer and AIDS-associated Kaposi's sarcoma (104). Other formulations like non-

pegylated liposomal doxorubicin, liposomal cytarabine, liposomal daunorubicin and liposomal cisplatin are approved for treatment of various types of cancers (105).

Micelles are amphiphiles or surfactants molecule, efficient in delivery of hydrophobic molecules. Genexol-PM is a paclitaxel-loaded polymeric micelles approved for use in breast and lung cancer (106).

Dendrimers are repetitively branched 3D molecules. It is a polymer-based drug delivery vehicle with advantages of nanoscale size (2-10 nm), polyvalency, high water solubility, low polydispersity, and biocompatibility (107). Polyamidoamine (PAMAM) dendrimers is an effective carrier molecule for the delivery of siRNA in gene therapy (108, 109). SPL7013 (VivaGel), a formulation of “polyanionic lysine G4 dendrimer” that shows antiviral activity against HIV and HSV. It is currently in phase III clinical trials (110, 111).

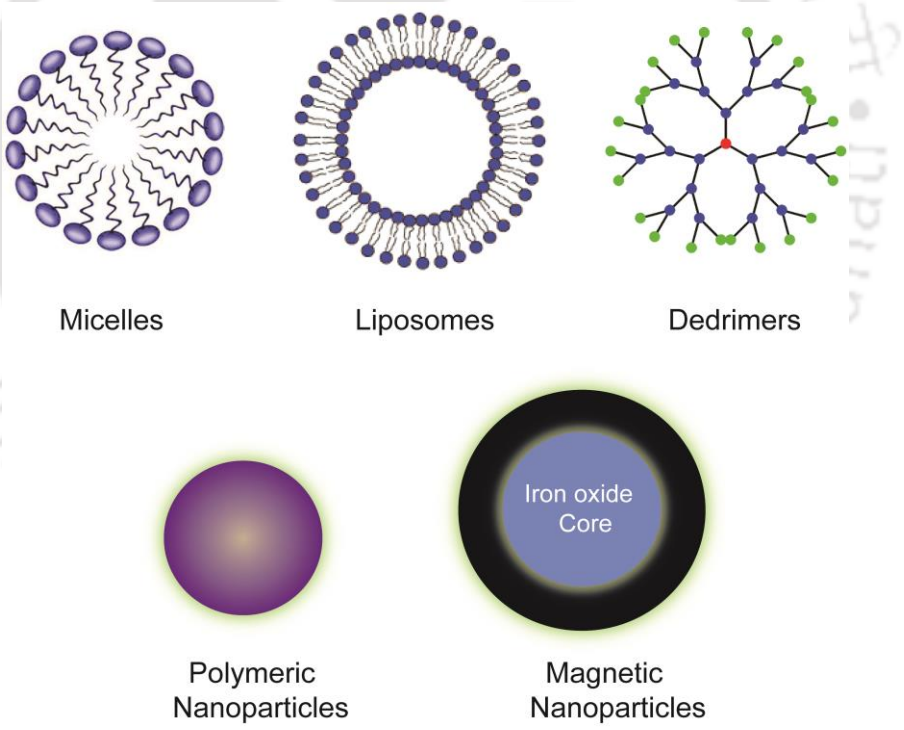

Figure 2.6: Different types of drug nanocarriers. It includes micelles, liposomes, dendrimers, polymeric nanoparticles and magnetic nanoparticles.

Magnetic nanoparticles are made up of two components, a magnetic material (Iron, Nickel, and Cobalt) and chemical component for functionality. A biocompatible magnetic carrier (ferrofluids) is attached to cytotoxic drug and delivers at a specific target site within the body by high-gradient magnetic fields (112). Octreotide conjugated superparamagnetic iron oxide nanoparticles are used in MRI and increases the sensitivity for the early detection of breast carcinoma (113). Currently, magnetic nanoparticles are not approved for clinical practice in drug delivery.

Gold nanoparticles are synthesized by the chemical reduction of chloroauric acid ($HAuCl_4$). It exhibits physical, chemical, optical, and electronic properties. The gold surface is highly stable and can be chemically modified to target drug or probes (114).

Poly(lactic-co-glycolic acid) (PLGA) is a copolymer of lactic acid and glycolic acid. PLGA is FDA approved biodegradable polymer (115). PLGA nanoparticles are internalized in cells through fluid phase endocytosis. Additionally, the surface can be modified using specific ligand for enhanced uptake of nanoparticle through receptor-mediated endocytosis. The PLGA-based nanoparticles as drug delivery systems are listed in Table 2.1.

Table 2.1: List of PLGA-based nanoparticles as drug delivery systems

Receptors	**Ligands**	**Drug**	**References**
Folate receptor	Folate	Paclitaxel	(116)
Transferrin receptor	Lactoferrin	Urocortin	(117)
Prostate specific receptor	PSMA	Cisplatin	(118)
αvβ1 integrins	RGD/RGDp LDV/LDVp	Ovalbumin	(119)
Opioid receptor	Simil-opioid peptide	Loperamide	(120)
HER-2	rhuMAbHER2	PE38KDL	(121)

2.8 Targeted drug delivery

The traditional drugs are associated with non-specific side effects that can be overcome by targeted drug delivery. There are different ways to specifically target drug or nanocarriers to cell

or organ. Overexpressed cell surface molecules are often used as a target to deliver drug. Targeted delivery is commonly used in diagnosis and therapy. The monoclonal antibodies, peptides, toxins, viral proteins are known to act as homing molecules.

Monoclonal antibodies in targeted drug delivery

Monoclonal antibody (MAb) binds specifically to cell surface receptor. The monoclonal antibodies conjugated to chemotherapeutic drugs are called antibody-drug conjugates (ADCs). The advantage of ADCs is that it allows targeted accumulation of drug to a specific site. The development of efficient ADCs is dependent upon two factors such as drug potency and conjugation of the suitable linker molecule to antibody (122). High potency drug molecules such as microtubules inhibitors (uristatins and maytansinoids) and DNA damaging agent (calicheamycin or duocarmycin analogs) are effective for successful ADCs (123). Gemtuzumab ozogamicin (Mylotarg) first ADC approved by the FDA (in 2000), in which humanized monoclonal antibody is conjugated to calicheamycin. It targets CD33 and approved for treatment of relapsed acute myelogenous leukemia. Ado-trastuzumab emtansine or T-DM1 (Kadcyla) is FDA approved (in 2003) for the treatment of HER2-positive metastatic breast cancer (124). Other ADCs, Inotuzumab ozogamicin (Besponsa) is a CD22-directed antibody-drug conjugate (125). Recently in August 2017, it is approved for the treatment of adults with refractory B-cell precursor acute lymphoblastic leukemia. Mapatumumab in conjugation with paclitaxel and carboplatin is under clinical trial phase II for the treatment of non-small-cell lung cancer (NSCLC) (126). Multiple challenges are associated with the successful clinical translation of ADCs. It includes the discovery of novel cancer cell specific antigens, internalization through receptor-mediated endocytosis, proper linker site for drug attachment in antibody, limited penetration of antibody into solid tumor (122).

Antibody-conjugated drug-loaded nanoparticles can release large amounts of a drug to the specific cells. Trastuzumab (Herceptin) is well known monoclonal antibody attaches to HER2 receptor which is overexpressed in breast cancer. Anticancer drug, paclitaxel is loaded in PLGA nanoparticles and modified with Trastuzumab showed effective treatment of breast cancer (127). Kou G *et al.* have shown that targeting can also be achieved with single chain antibody (scFv). SM5-1 is overexpressed on melanoma, hepatocellular carcinoma, and breast cancer cells. The paclitaxel loaded in PLGA nanoparticles and coated with SM5-1 scFv showed enhanced *in vitro* cytotoxicity in human squamous carcinoma cell line (128). *In vivo* studies

show anticancer MAb, 2C5 conjugated to doxorubicin loaded liposomes can reduce size of brain tumor (129).

Peptides in targeted drug delivery

There are several advantages of using peptide as carrier over antibodies. Prior knowledge of target molecule is not required and target does not need to be antigenic. Binding affinity, conjugate stability, and drug activity can be maintained after the conjugation of drug to peptide. The addition of unnatural amino acid can enhance stability of drug. The mass of peptide carrier is much lower than antibodies. So, it has enhanced ability of tumor penetration. The peptide drug conjugates induce efficient cellular uptake through receptor-mediated endocytosis. The chemical degradation of linker molecule is possible in endosome or lysosome as a result drug is release out in cytoplasm. The production cost is less as compared to antibodies (122). GRN1005 is a paclitaxel conjugated angiopeptin-2 that targets lipoprotein receptor protein-1. It is under clinical assessment for treatment of solid tumor cells (130). But, till now peptide drug conjugates have not received regulatory approval (122).

A peptide, octreotide is eight amino acid analog binds with high affinity to somatostatin receptors (SSTR2) (129). Octreotide is internalized through receptor-mediated endocytosis. Chemically modified octreotide is used as drug carriers and magnetic resonance imaging (MRI) contrast agents (131). This peptide is conjugated with radioisotopes for tumor diagnosis and peptide receptor radiotherapy (132, 133). Octreoide is chemically conjugated to anti-cancer drugs for enhanced delivery of drugs to tumor cells (134).

A three amino acid sequence, Arginine-Glycine-Aspartic acid (RGD) derived from fibronectin plays critical role in cell recognition site for integrin α5β (135). High expressions of integrins are associated with tumor progression. It involved in many biological processes such as angiogenesis, invasion and metastasis (136). Different drug nanocarriers were conjugated to RGD peptide for enhanced delivery of drug to specific sites. Anticancer drug, doxorubicin encapsulated within poly(amidoamine) dendrimers and conjugated to RGD for targeted therapy of cancer cells (137).

Bacterial toxins for targeted drug delivery

Bacterial toxins including diphtheria, anthrax, tetanus, botulinum, cholera, and shiga enter the cell through specific cell surface receptors. Some of these receptors are highly expressed in diseased condition. These toxins have two subunits, so called as AB toxins. B-subunits bind to

the cell surface receptors and A-subunit having catalytic activity causing toxicity. The receptor-binding ability of these toxins can be used to deliver a therapeutic load to specific cells.

Tumor endothelial marker 8 (TEM 8) is overexpressed on tumor endothelial and cancer cells (138). The 13-mer peptide, KYNDRLPLYISNP derived from the protective antigen of anthrax toxin showed binding with an extracellular domain of TEM. This synthetic peptide was labeled with 18F for positron emission tomography (PET) imaging of TEM8 in cancer (1, 139). The KYND motif obtained from Anthrax toxin function as cell penetrating peptide and enhances the cellular uptake of KYND modified PEGylated liposomes (140).

The carboxy-terminal of heavy chain (also known as tetanus toxin C fragment, TTC) of tetanus toxin binds to ganglioside (GT1b) on the neuronal membrane and it has potential of targeted therapeutics (141). *In vitro* study shows, the nanoparticles conjugated to TTC with a crosslinker neutravidin involves in selective targeting of neuroblastoma cells (142). TTC conjugated nanoparticles can be used for delivering therapeutics to neurons affected by neurodegenerative diseases. The 12-mer peptide, “HLNILSTLWKYR”, Tet1 derived from tetanus toxin which has an affinity to neurons and possesses retrograde transportation properties. Tet-1 coupled to curcumin-loaded PLGA nanoparticles showed enhanced uptake in glial cells (143). Curcumin encapsulated-PLGA nanoparticles destroy amyloid aggregates and exhibit anti-oxidative property which can be used for treating Alzheimer's disease. The Tet1-poly(ethylenimine) (Tet1-PEI) polyplexes binds specifically and uptake by neuron-like PC-12 cells (144). Tet1-PEI can be developed for non-viral gene delivery vehicles into the central nervous system.

Botulinum toxin, BoNTs is also A-B type toxin which comprises enzymatically active subuint, ‘A’ and cell binding subunit, ‘B’. The subdomain of C-terminal heavy chain of BoNTs binds to luminal domain of synaptic vesicle (SV) glycoproteins SV2A, SV2B, and SV2C (isoforms) while polysialogangliosides, behave as low-affinity receptor facilitating its binding (145). The C-terminal of heavy chain, non-toxic fragment has a potential candidate for targeting non-viral drug carrier to central nervous system (146). Dobrenis K *et al.* have shown the effective lysosomal targeting of human enzyme, beta-N-acetyl hexosaminidase A coupling to TTC in the rat neuronal cell line (147). The delivery of biomolecules to neurons is highly efficient to treat missing enzyme activities in oxidative injury and lysosomal storage diseases.

The non-toxic B subunit of Cholera toxin (CTB) binds to GM1 ganglioside present on neuronal membrane (148). CTB modified mesoporous silica nanoparticles encapsulated within a lipid bilayer (protocells) was developed which allows higher loading capacity and cargo release in

targeted drug delivery. The CTB modified protocells is an efficient drug delivery system to motor neuron and further, it can be developed for the treatment of neuromuscular disorders (149).

Shiga toxin binds to human cell surface receptor, a glycosphingolipid, Gb3/CD77 (150). The expression of Gb3 is limited to human neuronal and endothelial cells (151) but it is highly expressed in different type of cancer such as breast, stomach, pancreatic, ovary, and colon (152-155). The non-toxic B fragment of STX (STxB) has potential to specifically target delivery of chemotherapeutic agents to tumor cells. The STxB coupled covalently to active metabolite of Topoisomerase inhibitor I, SN38 has shown hundred times more cytotoxicity effect than Irinotecan alone in pancreatic cancer cells and gastric cancer cells (153, 155, 156). STxB used for targeting photosensitizing drug such as TPP $(p\text{-}O\text{-}\beta\text{-}D\text{-}GluOH)_3$, and chlorine 6 into tumor cells. The STxB covalently conjugated porphyrin-based compound showed higher photocytotoxic effect as compare to photosensitizer alone. This is due to retrograde plasma membrane-to-Golgi apparatus transport (157, 158). Peripheral benzodiazepine receptors are potential targets for cancer therapeutics. STxB showed efficient delivery of prodrug, benzodiazepine RO5-4864 which is ligand for benzodiazepine receptors of mitochondria (159).

Viral proteins for targeted drug delivery

Similar to bacterial toxins, some viral proteins can specifically binds to cell surface receptors. Rabies virus glycoprotein (RVG) allows entry of virus specifically into neuron through acetylcholine receptor. RVG derivatives such as rabies virus- derived peptide (RDP) and RVG-29 has potential for targeted drug delivery (160). The RDP is short peptide corresponding to 330-357 amino acids derived from RVG. When it fused with brain derived neurotrophic factor (BDNF), it showed rapid and specific delivery in nerve cells causing neuroprotective activity such as reduction of stroke volume (161). The 29 amino acid peptide derived from RVG fused with 9 D-arginine residues (RVG29-9dR) was used to deliver siRNA for gene silencing in macrophages and microglia cells which express acetylcholine receptor (162). RVG29 peptide is efficient in BBB crossing and showed higher accumulation of itraconazole payload in neuronal cells when conjugated to albumin nanoparticles (163). A specific and effective drug delivery to brain is a challenging process in treatment of neurological diseases. Different peptides derived from viral proteins are new approach for targeting drug delivery to CNS.

3 Materials and Methods

3.1 Bacterial cell culture:

The glycerol stock (20%) of *Escherichia coli* strains and recombinant clones were stored in -80 ˚C. These were cultured in LB medium or 2xTY medium containing suitable antibiotics as per requirement. The details of *Escherichia coli* strains and media composition is given in Table A2 and A3, respectively in Appendix.

3.2 Expression of RDT:

Earlier, in our lab, RDT was cloned into pET-22b vector (89). The recombinant plasmid construct i.e pET-22b-RDT was transformed into competent *E.coli* BL21 (DE3) cells (100 µl) by standard heat shock method. Transformed cells were plated on LB agar plate containing ampicillin (100 µg/ml). A single colony was inoculated in 5 ml 2xTY media containing ampicillin (100 µg/µl) and 1% glucose. It was incubated overnight at 37 ˚C with shaking (180 rpm). Then, it was further sub-cultured (1:200 dilution) into 100 ml 2xTY media containing ampicillin. It was incubated at 37 ˚C with shaking (180 rpm) till its OD_{600} reached 0.6-0.8. The expression of recombinant protein was induced by Isopropyl β-D-thiogalactopyranoside (IPTG, 0.5 mM) for 8 hour at 28 ˚C. Cells were harvested by centrifugation and re-suspended uniformly in PBS (pH 7.4). The whole cell lysate was prepared by sonication for 5 cycles each of 60 s, at 25% amplitude on ice using ultrasonic processor (Hielscher). Homogenate was clarified by centrifugation at 10,000 rpm for 15 min at 4 ˚C. The supernatant was saved and stored at -20 ˚C for further processing.

The recombinant His-tagged proteins, RDT were purified by Ni-NTA affinity chromatography on His-Trap FF affinity column (GE healthcare) as per manufacture's protocol. Briefly, the protein lysate was diluted with binding (equilibration) buffer, pH 7.4 containing imidazole (40 mM). The diluted protein sample was passed through the column at flow rate of 2 ml/min. Subsequently, the column was thoroughly washed with wash (binding) buffer having Imidazole (40 mM). The protein was eluted using elution buffer containing imidazole (500 mM). The residual imidazole was removed by dialysis against PBS for overnight at 4 ˚C with slow stirring. The detailed

compositions of buffers are given in Table A5 of the Appendix. The protein concentration was estimated using Bradford assay.

3.3 Protein estimation by Bradford's assay:

The concentration of purified protein samples (RDT or MBP-peptides) were estimated by Bradford assay (Sigma) (164). Amount of protein adsorbed on NPs was determined by Bradford assay according to a protocol used by Kockbek *et al.* (165). Coated or uncoated NPs were resuspended in 200 µl of PBS. Bradford reagent (200 µl) was added to each sample and incubated for 10 minutes at room temperature. Subsequently, absorbance was measured at 595 nm. Solutions of BSA with known concentrations were prepared to generate a standard curve. The amount of protein attached to NPs was estimated by using standard graph.

3.4 Mammalian cell culture:

Human glioblastoma cell lines, U-87 MG; mouse macrophage cell line, RAW 264.7; human breast cell line, MDA-MB 468 were procured from NCCS, Pune, India. These cells were cultured in DMEM growth medium with high glucose (HiMedia) supplemented with 10% fetal bovine serum (Gibco) and antibiotics (Anti-anti, Gibco). The cells were sub-cultured by trypsinization once it reached 80-90% confluency. The adherent cells were washed with sterile PBS (pH 7.4) and detached with 0.25% Trypsin-EDTA (Gibco). After a few minutes, trypsin was removed out of the flask and cells were flushed with the fresh medium to make a uniform cell suspension. Cells were centrifuged at 2,400 rpm for 6 min at 4 ˚C. The pellet was resuspended in 1 ml complete media. Cells density was estimated using trypan blue dye exclusion procedure. The dead cells don't take dye, but viable cells do. 10 µl of resuspended cells were mixed with 10 µl of 0.4% trypan blue (Invitrogen). Then, 10 µl of mixed sample is loaded in cell counting chamber slide (Invitrogen). This slide was inserted in automated cell countess (Invitrogen). Total numbers of cells, including viable and dead cells, were recorded. The desire cell density was reseeded on another 25 cm^2 flask or 6 or 96 well plates. The cells were maintained in humidified 5% CO_2 incubator at 37 °C.

The cells were also cryopreserved for a longer period in freezing media. Freezing media is composed of 95% serum and 5% dimethyl sulfoxide (DMSO). DMSO acts as cryoprotectant which minimizes cell damage occur during the freezing process. Cells were resuspended in 1 ml freezing media and placed in liquid nitrogen (-196 ˚C) for longer storage. Medium and other reagents used in mammalian cell culture are given in Table A4 in the Appendix.

3.5 Synthesis of poly (lactic-co-glycolic acid) PLGA Nanoparticles:

The synthesis of poly (lactic-co-glycolic acid) PLGA nanoparticle (NPs) was carried out by using previously developed emulsification solvent evaporation method (166). 5 mg of PLGA was dissolved in either 1 ml dichloromethane (DCM, Merck) or 1 ml chloroform (Merck). Different solvent results in different sizes of nanoparticles. Further, PLGA solution was added dropwise in 0.5% Polyvinyl alcohol in water under continuous sonication at 30% amplitude for 2 min at room temperature (RT). Here, PVA was used as a non-ionic emulsifying agent. During synthesis, either dye or drug was loaded. Fluorescein or Rhodamine 123 (5 µM) was incorporated to make these nanoparticles fluorescent. Dye was dissolved in 0.5% PVA in water. An Anti-cancer drug, Irinotecan was used for the experiments. For drug-loaded nanoparticles, Irinotecan in water was mixed with PLGA solution and sonicated well to create a well formed emulsion. This was subsequently added dropwise to PVA solution. NPs were washed thrice with water to remove the excess solvent. Subsequently, it was dried by vacuum drying. The protein-coated NPs was formed by incubating recombinant receptor binding domain of DT (RDT, 100 µg/ml) in PBS (pH 7.4) with NPs (5 mg/ml) for 2 h at 37 ˚C. A schematic diagram of NP synthesis is given in Figure 3.1.

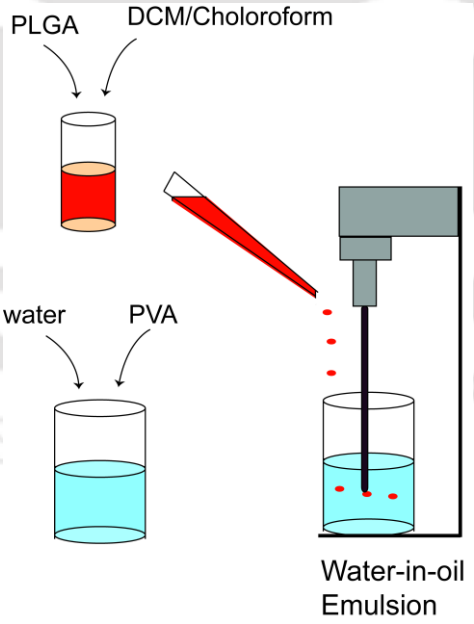

Figure 3.1: Synthesis of NPs. PLGA was dissolved either in dichloromethane or chloroform and added dropwise to 0.5% polyvinyl alcohol solution under continuous sonication at 30 Kpsi for 2 min at room temperature.

3.6 Transmission Electron Microscope (TEM):

The size and morphology of PLGA NPs (NPs) and RDT coated NP (RDT-NPs) were observed by Transmission Electron Microscope, (TEM; JEM 2100; Jeol). Sample of RDT-NPs was prepared by incubating NPs with RDT protein for 2 h and then centrifuged at 8,000 rpm for 5 min at RT. The supernatant was removed and pellet was diluted in distilled water. The samples were added in the carbon coated copper grid and kept for drying for 4 h at room temperature. TEM was operated at an accelerating voltage of 200 KV. The size of NPs was calculated by ImageJ software (167).

3.7 Field Emission Scanning Electron Microscope (FESEM):

The size and surface morphology of NPs and RDT-NPs were observed by Field Emission Scanning Electron Microscope (FESEM; Zeiss, model sigma). The samples were diluted in water and drop cast into the aluminum foil wrapped coverslip and dried for overnight. Sputter coating is applied using ultra-thin gold coating over the polymeric nanoparticle. Sputter coating provides thermal conductivity to sample and reduce microscope beam damage. Samples were imaged with an accelerating voltage of 3 kV. The size of NPs was calculated by ImageJ software (167).

3.8 Dynamic light scattering (DLS):

The size of particles is determined by the random movement of particles in a liquid medium using dynamic light scattering (DLS; Zetasizer; Nano ZS, Malvern). NPs and RDT-NPs were resuspended in filtered water. The particle size, size distribution, polydispersity index (PDI) and zeta potential of NPs and RDT-NPs were analyzed using DLS.

3.9 UV-Visible absorption spectroscopy:

The association of RDT with nanoparticles (NPs) is detected using UV-Vis absorption spectroscopy. The fixed amount of NPs (500 µg) is incubated with different concentration of recombinant RDT (0-25 µg/ml) in PBS (pH 7.4) for 2 h. Then, NPs were centrifuged at 8,000 rpm for 5 min. The pellet having NPs coated with RDT (RDT-NPs) was dissolved in 1 ml water. The absorbance of RDT-NPs is measured at 280 nm. Water is used as a blank solution and its reading was subtracted from samples.

The absorbance spectrum of Irinotecan was measured using UV-Visible spectrophotometer (Beckman coulter, DU 730). 10 µg/ml of Irinotecan dissolved in water. The spectrum was recorded from 210 to 600 nm using 10 mm pathlength quartz cuvette.

3.10 Fourier transform infrared spectroscopy (FT-IR):

FT-IR spectroscopy was used for characterization of NPs and protein-coated NPs. The NPs and RDT-NPs were mixed separately with IR grade, potassium bromide (Sigma) in the ratio of 1:100. Pellets were prepared by applying 5.5 metric ton pressure with a hydraulic press. The infrared absorption spectra were collected in an inert atmosphere over a wave number range of 450-4000 cm^{-1} in FT-IR instrument (Perkin Elmer; Spectrum Two).

3.11 ELISA to detect extent of coating of NPs by RDT:

The coating of recombinant RDT on NPs was detected by ELISA. Recombinant RDT has His-tag. It was detected using anti-His antibody. NPs were incubated with varying concentration of RDT in PBS for 2 h at 37 ˚C. Subsequently, NPs were separated by centrifugation and resuspended in 1 ml PBS. 100 µl of resuspended NPs was taken in 1.5 mL tubes and separated by centrifugation. The supernatant was discarded. NPs were resuspended and incubated in blocking buffer (2% BSA in PBS), for 2 h at room temperature. Subsequently, NPs were separated by centrifugation, resuspended, and washed with PBS. These NPs were resuspended in 100 µL of 2% BSA in PBS (pH 7.4) with mouse anti-His antibody (1:1000 dilution, Calbiochem) and incubated for 1 h at room temperature. NPs were collected by centrifugation, washed with PBS, and resuspended in 100 µl of HRP-conjugated anti-mouse antibody (1:1000 dilution, Sigma-Aldrich) in 2% BSA-PBS. After 1 h of incubation at room temperature, NPs were harvested by centrifugation, washed with PBS, and resuspended in 400 µL of o-Phenylenediamine dihydrochloride (OPD) substrate. After a few minutes of incubation at room temperature, 100 µL of the sample was transferred to wells of ELISA plate. Reaction was stopped by adding 50 µL of 8 N H_2SO_4, and absorbance was measured at 492 nm. The composition of substrate solution is given in table A5 (Appendix).

Stability of RDT adsorbed on NPs was also determined by ELISA. For this, RDT-coated NPs were resuspended in serum-free media and incubated for different time durations at 37 °C. Subsequently, NPs were separated by centrifugation and resuspended in 1 ml PBS. 100 µl of resuspended NPs was taken in 1.5 mL tubes and separated by centrifugation. The supernatant was discarded. NPs were resuspended and incubated in blocking buffer (2% BSA in PBS), for 2

h at room temperature. Subsequently, NPs were separated by centrifugation, resuspended, and washed with PBS. These NPs were resuspended in 100 µl of 2% BSA in PBS (pH 7.4) with mouse anti-His antibody (1:1000 dilution, Calbiochem) and incubated for 1 h at room temperature. NPs were collected by centrifugation, washed with PBS, and resuspended in 100 µl of HRP-conjugated anti-mouse antibody (1:1000 dilution, Sigma-Aldrich) in 2% BSA-PBS. After 1 h of incubation at room temperature, NPs were harvested by centrifugation, washed with PBS, and resuspended in 400 µl of o-Phenylenediamine dihydrochloride (OPD) substrate. After few minutes of incubation at room temperature, 100 µl of sample was transferred to wells of ELISA plate. Reaction was stopped by adding 50 µl of 8 N H2SO4, and absorbance was measured at 492 nm. The composition of substrate solution is given in table A5 (Appendix).

3.12 RNA isolation:

Total RNA was isolated from mammalian cell line for the preparation of cDNA. Total RNA is extracted by TRI reagent (Sigma). 1 ml of TRI reagent was added in 25 cm^2 culture flasks having 1 x 10^6 cells. The cells were pooled and passed several times through a syringe to form a homogeneous lysate. The samples were kept at room temperature for 5 min to ensure complete dissociation of nucleoprotein complexes. Then, 200 µl of chloroform per ml of TRI reagent was added. After, 30-60 s of vigorous shaking, sample was allowed to stand for 10 min at room temperature. This mixture was then centrifuged at 12,000 g for 15 min at 4 ˚C. The RNA present in upper aqueous phase was transferred to fresh tube. 500 µl of 2-propanol is added to the tube and mix properly. Samples were kept for 10 min in room temperature. Then, it was centrifuged at 12,000 rpm for 10 min at 4 ˚C. Supernatant was removed and RNA pellet washed with 1ml 75% ethanol. Then, samples were centrifuged at 12,000 rpm for 10 min at 4 ˚C. Supernatant was removed and RNA pellet was air-dried. Finally, RNA pellet was resuspended in water (20-30 µl)

3.13 Synthesis of cDNA:

The cDNA is prepared using verso cDNA synthesis kit (Thermoscientific). Reverse transcriptase is an RNA dependent DNA polymerase with attenuated RNase activity. It synthesizes long cDNA strand up to 11 kb. 1 µg of total RNA (10 µl) is heated at 65 ˚C for 5 min in a thermal cycler (Bio-Rad, C1000). This step will remove all the secondary structure present in RNA. Then, 10 µl master mix was added to the tube. The mixture of total RNA and master mix is again placed in a thermal cycler for 60 min at 42 ˚C. The enzyme was inactivated at 95 ˚C for 2 min. The composition of master mix is given below:

Components	Volume
5X cDNA synthesis Buffer	4 µl
Verso Enzyme mix	1 µl
Random Hexamer (500 ng/µl)	1 µl
dNTPs (5 mM each)	2 µl
Water	2 µl
Total volume	10 µl

3.14 RT-PCR (Reverse-transcriptase PCR)

The expression of HB-EGF in U 87-MG cells was determined using RT-PCR. The cDNA prepared from U 87-MG cells is used as a template. The HB-EGF specific primer is used and primer detail is given in table A7 of Appendix. The composition of master mix and PCR program are given below:

Components	Volume
cDNA	1 µl
2X Master mix	10 µl
HBEGF FP (200nM)	1 µl
HBEGF RP (200nM)	1 µl
Water	7 µl
Total volume	20 µl

PCR program:

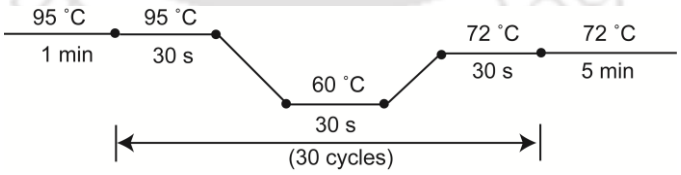

3.15 Spectrofluorometer:

The leaching of dye, Rhodamine 123 from NPs was checked by Spectrofluorometer. This experiment was used to assess the extent of leaching of the dye with time. PLGA NPs with Rhodamine 123 or without the dye were resuspended in serum-free culture media and

incubated at 37 ˚C, for different durations, with mild shaking. Subsequently, NPs were separated by centrifugation and resuspended in PBS. Fluorescent intensity of these NPs were measured by spectrofluorimetry with pathlength of 1 cm, excitation wavelength of 505 nm (Slit width = 1 nm) and emission wavelength of 528 nm (Slit width = 5 nm).

The mechanism of RDT-NPs internalization is elucidated using Spectrofluorometer. The U-87 MG cells were seeded on T-25 flask at a density 2 x 10^5 cells/flask. The cells were treated with different endocytosis inhibitors. After 2 h treatment, cells were washed with PBS twice and then trypsinized. Cells were resuspended in 1 ml serum media and then centrifuged at 3,000 rpm for 7 min at room temperature. The pellet was collected and washed with PBS followed by centrifugation. The pellet was resuspended in 200 µl PBS. The cells were lysed by using ultrasonicator (Hielscher) at amplitude 20 % for 10 s. The cell lysate were further diluted in PBS and fluorescence intensity of Rhodamine 123 was measured by Fluoromax-4 (Horiba scientific) with λ_{Ex} = 505 nm, λ_{Em} = 528 nm, Pathlength = 1 cm. The slit width of excitation and emission were 1 and 5 nm, respectively.

The uptake of Transferrin-FITC was also measured using Spectrofluorometer. The U 87-MG cells were treated with transferrin-FITC (0.1 µM and 0.25 µM) along with or without chlorpromazine (5 µM). The cell lysate was prepared as above. The fluorescence intensity of Rhodamine 123 was measured by Fluoromax-4 (Horiba scientific) with λ_{Ex} = 492 nm, λ_{Em} = 518 nm, Pathlength = 1 cm. The slit width of excitation and emission were 1 and 5 nm, respectively.

3.16 Flow cytometer:

The uptake of NPs was also determined by flow cytometer. The U-87 MG or RAW 264.7 cells were seeded in 6 well plates (1 x 10^5 cells/well) and maintained in humidified 5% CO_2 incubator at 37 ˚C. After 48 h incubation, cells were treated with uncoated NPs; BSA- or RDT-coated NPs in serum-free medium for 2 h at 37 ˚C. After trypsinization, cells were harvested by centrifugation and re-suspended in 1 ml Serum free media. The fluorescence intensity of Rhodamine 123 was measured by flow cytometer in FL-1 channel (FACSCalibur, BD, USA) and data analyzed by FCS-express software.

3.17 Fluorescence Imaging:

The U-87 MG (1 x 10^5) cells were seeded over cover slip in each 35 mm petri plate having 2 ml complete media. Cells were incubated for 48 h in humidified 5% CO_2 incubator at 37 ˚C. Cells were treated with different sample in serum-free medium for 2 h. After treatment, media was

removed and cells were washed with PBS. The nuclear staining was done by using 4',6-diamidino-2-phenylindole (DAPI). DAPI (4 µg/ml in PBS) was added to the cells and incubated for 5 min at room temperature. Excess of stain was removed by multiple washing with PBS. The cells were fixed with 3.7% formaldehyde in PBS for 20 minutes at room temperature. After washing with PBS, cells were imaged using inverted Epi-fluorescence microscope (Eclipse TiU, Nikon). The uptake of Rhodamine 123 loaded NPs were detected using a filter for green fluorescence (B-2E/C, Nikon) and DAPI using (UV-2E/C, Nikon). The composition of 3.7% formaldehyde is given in table A5 of the appendix.

3.18 Cell viability assay:

Cell viability was estimated by MTT assay (168). The U 87-MG cells (10^4/well) or MDA MB 468 cells (5 x 10^3/well) were seeded in 96 well plates. The cells were cultured for 48 h at 37 °C in 5% CO_2. Later, cells were treated with different sample for a specific duration in serum-free medium. Subsequently, 3-(4, 5-dimethylthiazol-2yl)-2, 5-diphenyltetrazolium bromide (MTT) solution (10 µl, 5 mg/ml in PBS) was added to each well. Further, Plate was incubated for 2 h at 37 °C in 5% CO_2, wrapped in aluminum foil. After incubation, MTT-containing medium was replaced by 100 µl dimethyl sulfoxide (DMSO, Merck) to solubilize MTT-formazan crystals. After incubation for 10 min at 37°C, absorbance was measured at 570 nm and reference reading at 690 nm was recorded by a microplate reader (Infinite 200 PRO, Tecan). Cell viability (%) was measured with respect to untreated cells.

$$\text{Cell viability (\%)} = \frac{(O.D_{570} - O.D_{690})_{Treated}}{(O.D_{570} - O.D_{690})_{Untreated}} \times 100$$

3.19 In-vitro drug release assay:

During NP synthesis, 1.65 mg of Irinotecan was loaded in 2.5 mg PLGA NP. The Irinotecan-loaded NPs (2.5 mg) were dispersed in 1 ml of PBS (pH 7.4) and incubated at 37 ˚C with gentle shaking. At different time point, Irinotecan-loaded NPs was harvested by centrifugation at 10, 000 rpm for 5 min at room temperature. Release of Irinotecan was assayed by measuring absorbance of supernatant at 255 nm and 370 nm. A standard curve was made by measuring absorbance of Irinotecan solution of different concentrations. Release of the drug percentage from NPs was calculated from the absorbance data using the standard curve.

3.20 Synthesis of peptides:

200 mg of Rink amide MBHA resin (loading 0.7 mmol) was taken with a syringe containing frit and was allowed to swell with DCM solvent first and then with DMF solvent. After that, Fmoc group of the resin was cleaved with 20% pip/DMF. The resin was then washed with DMF solvent. Then, 2.0 equivalent of Fmoc-Gly-OH, 2.5 equivalent of o-NosylOXY (coupling reagent) and 4.5 equivalent of DIPEA (base) were dissolved in DMF solvent and added to the syringe. The syringe was allowed to rotate at SPPS rotator for coupling. After that, the reaction mixture in the syringe was washed with DMF and DCM. It was then acetylated (capping) with 2 equivalent of Ac2O, 2 equivalent of NMI in DCM solvent. Again Fmoc cleavage of the amino acid attached with resin was carried out with 20% pip/DMF and the peptide sequence was continued in the same procedure said above. At last, Fmoc group was cleaved with 20% pip/DMF. Finally, cocktail cleavage was carried out with 2ml of TFA: DCM (8.5:1.5) and one drop of H2O for 5h to cleave C-terminus of the peptide from rink amide resin. After completion of reaction, the mixture was precipitated in cold diethyl ether solvent to get the crude peptide.

3.21 Liquid chromatography:

Crude peptides were dissolved in Acetonitrile/Water (1:1) and purified by RP-HPLC (Waters 600E) using a C18-μ Bondapak column at a flow rate of 4 mL/ min. Binary solvent system was used, solvent A (0.1 % Trifluoroacetate in H_2O) and solvent B (0.1 % Trifluoroacetate in Acetonitrile). A Waters 2489 UV detector was used with an option of dual detection at 214 and 254 nm. A total run time of 20 min. was given and gradient used for purification was 5−100 % acetonitrile for 18 min followed by 100% acetonitrile till 20 min.

The purity of the peptide DTP28 was confirmed using Waters 600E Analytical HPLC system, Ascentis C18 analytical column at a flow rate of 1 ml/min, linear gradient of 5-100% acetonitrile over 18 minutes in a total run time of 20 min. Dual wavelength was selected at 214 nm and 254 nm. The purity of the other three peptides, DTP28A, DTP28AE and DTP28Neg were confirmed using Agilent-Q-TOF 6500 instrument, in ESI-LCMS positive mode, Agilent eclipse plus C18 analytical column at a flow rate of 0.3 ml/min, linear gradient of 5-100% CH_3CN over 6 minutes in a total run time of 7 min. Wavelength was selected at 214 nm.

3.22 Mass spectrometry:

The mass of the peptide samples were analyzed on Agilent-Q-TOF 6500 instrument, in electrospray ionization (ESI) positive mode, equipped with the Mass hunter work station software.

MALDI mass of the peptide samples were analyzed using CHCA matrix on BRUKER autoflex speed instrument which consists of a MALDI ionization source for samples in the solid state and a TOF/TOF mass analyzer, equipped with Bruker daltonics flex analysis software. To prepare CHCA matrix, 1.0 mg of CHCA was dissolved in 100 µl of CH_3CN/H_2O (1:1) containing 0.1% TFA.

3.23 Tricine SDS-PAGE:

Tricine SDS-PAGE is commonly used to separate protein in the mass range 1-100 kDa. The purity of short peptides of molecular weight ~2.9 kDa is checked by tricine SDS-PAGE. Tricine SDS-PAGE was run according to the protocol of Hermann Schagger (169). Briefly, an acrylamide gel was prepared by introducing a 10% 'spacer gel' between 4% stacking and 16% separating gels to sharpen the peptide bands. Anode buffer as the lower electrode buffer and cathode buffer as the upper electrode buffer were used in vertical electrophoresis apparatus. The gel was run at constant voltage of 30 V until sample crosses the stacking gel and then voltage was increased to 90 V and run up to the end. Peptides were visualized by silver staining. Buffer compositions of Tricine SDS-PAGE are given in Appendix (Table A5).

3.24 Silver staining:

The Tricine SDS-PAGE gel was stained by silver staining. Protein detection using silver staining is 50 times higher sensitive than coomassie brilliant blue staining. Tricine SDS-PAGE gel was incubated in fixing solution for 30 min. Subsequently, incubation solution was added and incubated for 30 min. Then the gel was washed with distilled water for 3 times (5 min each). Silver staining solution was added and incubated for 50 min. Gel was developed using developing solution. Once bands appear, stop solution was added. The gel image was taken by gel documentation system (Bio-Rad, ChemiDoc XRS+). The Buffer compositions of silver staining are given in Appendix (Table A5).

3.25 Circular Dichroism (CD):

The secondary structure of peptides was determined using a CD spectrometer (Jasco-J815). The three scan recorded from 185 to 300 nm using 5 mm optical pathlength at ambient temperature (25˚C). The peptide concentrations were 15 µM (40 µg/ml) in 1% Ethanol. Spectra were corrected for background reading by subtracting a spectrum measured with 1% Ethanol in water, without peptide. CD spectra are given as the molar CD extinction coefficient ($\Delta\varepsilon_M$) in terms of M^{-1} cm^{-1}. Spectra were analyzed using K2D3 program to predict composition of secondary structures (170). (http://cbdm-01.zdv.uni-mainz.de/~andrade/k2d3//).

3.26 Molecular docking:

The designed peptides were docked on HB-EGF using CABS-dock (171). The structure of HB-EGF was extracted from the X-ray crystallographic structure of Diphtheria toxin-bound HB-EGF (PDB ID: 1XDT) and used as an input for CABS-dock. The amino acid sequences of the peptides were the other input for docking. Blind docking, with 200 simulation cycles, were performed for each peptide without any information on the secondary structure of peptides, possible binding sites and flexibility of the receptor. CABS-dock reports 10 best models. These structures were visualized and analyzed using UCSF Chimera (172).

3.27 Molecular dynamic simulation:

The stability and dynamics of peptide derived from Diphtheria toxin are studied using molecular dynamic simulation. The PDB file is generated by excising 505-531 fragment of the DT complex with HB-EGF (PDB ID: 1XDT). GROMACS (173) was used to perform molecular dynamics simulation with GROMOS 43a1force field. The structures were energy minimized by the steepest descent algorithm in vacuum and water for maximum 2000 steps before a production run. The solvent molecules (SPC water) were then added and other energy minimization procedure was carried out in water prior to the simulation run. A 10 ns simulation was carried out under NVT ensemble having temperature 300K. A 2 fs time step used in the numerical integration. After the completion of the simulation, output data were analyzed according to the root mean square deviation (RMSD), root mean square fluctuation (RMSF) and radius of gyration (Rg). Structures were visualized using UCSF Chimera (172).

3.28 Cloning of short peptide (DTP28) into bacterial expression vector:

The short fragment of receptor binding domain of Diphtheria toxin (RDT) named as DTP28 was sub-cloned into His-MBP vector. RDT cloned in pET-22b-RDT vector was used as a template for amplification of DTP28 (89). The sub-cloned fragment corresponding to 505¨531 of DT with additional glycine at each end. The primers were used for PCR have restriction enzyme sites for *Nde I* and *Xho I* at 5' and 3' end respectively. Sequences of primers are given in Table A7 of Appendix. The PCR product and His-MBP plasmid (vector) was double digested separately with *Nde I* and *Xho I* (NEB). The restriction digested vector and insert were eluted out using Nucleospin Gel and PCR clean up kit (Macherey-Nagel). Both the double digested products were ligated to form His-MBP-DTP28 recombinant plasmid. The recombinant plasmid was transformed into chemically competent *Escherichia coli* DH5α using the standard heat shock method. Transformed cells were plated on LB agar containing ampicillin plate. The plates are incubated at 37 ˚C for overnight. The different colonies were picked and plasmid was isolated using HiMedia, HiPurA plasmid DNA miniprep purification kit. Recombinant clones were confirmed by PCR, double digestion and DNA sequencing. Sequencing was done by dideoxy method using universal T7 reverse primers (Appendix table A7). Sequencing was performed by Eurofins Genomics India Pvt. Ltd. Further, recombinant His-MBP-DTP28 plasmid transformed to *Escherichia coli* BL21 (DE3) for protein expression.

3.29 Polymerase chain reaction (PCR):

PCR was performed using a thermal cycler (Bio-Rad, C1000). The standard PCR program was followed which involved initial denaturation for 5 min at 95 ˚C, followed by 30 cycles of 30 s at 95 ˚C, 30 s at 60 ˚C, 30 s at 72 ˚C and the final extension was performed for 5 min at 30 s at 72 ˚C. Sequence of primers and reaction conditions used are given in appendix (Table A7).

Reaction mixture:

Components	Volume
2X Master mix (HiMedia)	50.0 µl
DTP28F (200 nM)	4.0 µl
DTP28R (200 nM)	4.0 µl
pET-RDT (template) (5 ng)	8.0 µl
Water	34.0 µl
Total volume	100.0 µl

The 100 µl PCR reaction mixture is equally distributed in 4 tubes and placed in a thermal cycler (Bio-Rad, C1000). The PCR program is given below:

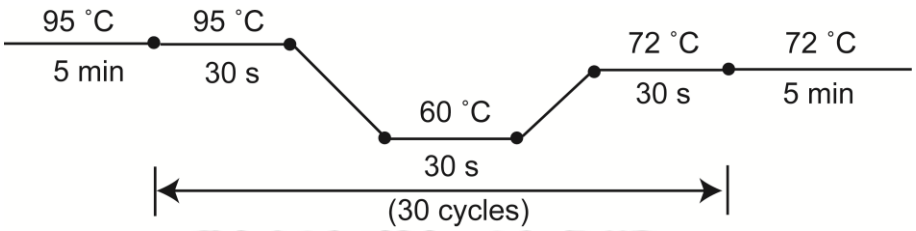

3.30 Plasmid Isolation:

Plasmid was isolated using HiPurA plasmid DNA miniprep purification kit (HiMedia). 3 ml overnight grown *E.coli* culture is taken into a tube and centrifuged at 12,000 rpm for 1 min. The bacterial pellet was resuspended in 250 µl resuspension solution (HP1) and then 250 µl lysis solution (HP2) was added. Mix thoroughly by gently inverting the tube 4-6 times. Subsequently, 350 µl neutralization solutions were added and mix thoroughly by gently inverting the tube 4-6 times. Samples were centrifuged at 12,000 rpm for 10 min at room temperature to obtain compact white pellet. Supernatant is carefully transferred into HiElute miniprep spin column and then centrifuged at 12,000 rpm for a min at room temperature. Column is washed twice with 500 µl wash solutions (HPB) and centrifuged at 12,000 rpm for a min at room temperature. Flow through liquid was discarded and centrifuged the empty tube to remove the excess wash solution. Water (30 µl) is added in column and allowed to stand for 2 min at room temperature followed by centrifugation at 12,000 rpm for a min. Eluted plasmid stored at -20 ˚C.

3.31 Agarose gel electrophoresis:

DNA samples were resolved by agarose gel electrophoresis. Agarose gel (0.8-1.5%) was prepared containing ethidium bromide (0.5 µg/ml) in 1X TAE buffer. After loading samples, gel was run at 80 V for a few hours at room temperature. The DNA fragments were visualized using gel documentation system (Bio-Rad, ChemiDoc XRS+). Composition of the buffer and staining solutions are given in Appendix (Table A)

3.32 Restriction digestion:

PCR amplified product (DTP28/Insert) and Plasmid (MBP vector) were digested with restriction endonucleases (NEB). The reaction mixture was incubated at 37 ˚C for 2 h. The composition of reaction mixture is given below:

	Vector (MBP Plasmid)	Insert (DTP28)
DNA sample	20.0 µl (2 µg)	20.0 µl (1.2 µg)
10X CutSmart buffer	4.0 µl	4.0 µl
Nde I (20U/µl)	1.0 µl	0.5 µl
Xho I (20U/µl)	1.0 µl	0.5 µl
Water	14.0 µl	15.0 µl
Total reaction volume	40.0 µl	40.0 µl

The reaction was terminated by heat inactivation at 65 ˚C for 20 min. The restriction digested product was resolved by Agarose gel electrophoresis.

3.33 Ligation:

The restriction digested vector and insert were eluted out using Nucleospin Gel and PCR clean up kit (Macherey-Nagel). The gel eluted products were ligated using Quick ligase (NEB). The ligation reaction mixture is given below:

Components	Sample	Negative control
MBP Vector (*Nde I*/*Xho I*)	7.0 µl (90 ng)	7.0 µl (90 ng)
DTP28 Insert (*Nde I*/*Xho I*)	1.4 µl (30 ng)	Nil
2X Quick Ligase Buffer	10.0 µl	10.0 µl
Quick Ligase (NEB)	1.0 µl	1.0 µl
Water	0.4 µl	2.0 µl
Total reaction volume	20.0 µl	20.0 µl

The ligation was carried for 1 h at 25 ˚C. The ligated mixture (5 µl) was transformed in competent *E. coli* DH5α cells (100 µl) by the standard heat shock method. Transformed cells were plated on ampicillin containing LBA plate. After overnight growth at 37 ˚C, three different colonies were picked and inoculated in 5 ml LB media. Plasmid was isolated from all the samples and recombinant clones checked by PCR and double digestion. The glycerol stock of recombinant clones was prepared and stored in -80 ˚C.

3.34 Quantification of DNA and RNA:

The UV-Vis spectrophotometry is used to quantify DNA and RNA. Samples were diluted in water and absorbance was measured at 260 nm and 280 nm. The optical density at 260 nm (A_{260}) equals 1.0 for a 50 µg/mL solution of dsDNA and 40 µg/mL solution of RNA for a 1 cm pathlength.

$$\text{dsDNA concentration} = 50\ \mu g/mL \times A_{260} \times \text{dilution factor}$$

$$\text{RNA concentration} = 40\ \mu g/mL \times A_{260} \times \text{dilution factor}$$

3.35 Preparation of competent cell:

Competent *Escherichia coli* cells were prepared by the $CaCl_2$ method. A single colony was inoculated in 5 ml LB media and incubated overnight at 37 ˚C with shaking. 500 µl of primary culture was inoculated into 25 ml of LB media and grown till its OD_{600} reached 0.4-0.5. The pellet was resuspended uniformly in 12.5 ml of chilled sterile 50 mM $CaCl_2$ and kept on ice for 45 min. The cells were harvested at 3,000 rpm for 10 min at 4 ˚C and pellet was re-suspended in 2 ml chilled 50 mM $CaCl_2$. Sterile glycerol (20% final volume) was added to the cell suspsension and aliquots of 100 µl each were made in sterile vials and stored in -80 ˚C for further use. The composition and preparation of sterile $CaCl_2$ and glycerol is given in table A5 of Appendix.

3.36 Transformation in bacterial cells:

The plasmid was transformed into chemically competent *Escherichia coli* cells by the standard heat shock method. Plasmid (50 ng) or ligation mixture (10 µl) was added in 100 µl competent cells and incubated in ice for 45 min. The cells were subjected to heat shock at 42 ˚C in water bath for 60 s and chilled on ice immediately afterwards. 900 µl of LB media was added and the cells were incubated for 1 h at 37 ˚C with shaking. Cells were harvested by centrifugation at

5000 rpm for 8 min at 4 ˚C and resuspended in 100 µl LB media. The cells were plated on LB agar (LBA) plate containing ampicillin followed by incubation at 37 ˚C for 12-16 h. Subsequently, the colonies were picked and inoculated in 5 ml LB media containing ampicillin. Further, plasmid was isolated using HiPurA plasmid DNA miniprep purification kit (HiMedia).

3.37 Sodium dodecyl sulfate polyacrylamide gel electrophoresis (SDS-PAGE) of protein:

The protein samples as well as standard SDS PAGE protein maker were resolved following the method of Laemmli (174). The 4% stacking and 12% separating gels of thickness 0.75 mm was prepared. The electrophoresis was run at constant voltage of 120 V for both stacking and separating gel in a MiniVE vertical electrophoresis system (G.E Healthcare). The electrophoretic run was monitored with tracking dye, bromophenol blue present in sample buffer. After the completion of electrophoresis, the gels were stained with the coomassie brilliant blue (CBB). The buffer composition of SDS-PAGE is given in Table A5 of Appendix.

3.38 Expression and Purification of MBP tagged peptide

The recombinant construct of DTP28 in MBP vector was transformed into competent *E. coli* BL21 (DE3) cells (100 µl) by the standard heat shock method. Transformed cells were plated on LBA plate containing ampicillin. A single colony was inoculated in 5 ml 2xTY media containing ampicillin (100 µg/µl) and 1% glucose. It was incubated overnight at 37 ˚C with shaking (180 rpm). Then, it was further sub-cultured (1:200 dilution) into 100 ml 2X TY media containing ampicillin. It was incubated at 37 ˚C with shaking (180 rpm) till its OD_{600} reached 0.6-0.8. The expression of recombinant protein was induced by Isopropyl β-D-thiogalactopyranoside (IPTG, 0.4 mM) for 4 h at 37 ˚C. Cells were harvested by centrifugation and re-suspended uniformly in PBS (pH 7.4). The whole cell lysate was prepared by sonication for 5 cycles each of 60 s, at 25% amplitude using Ultrasonic processor (Hielscher). Homogenate was clarified by centrifugation at 10,000 rpm for 15 min at 4 ˚C. The supernatant was saved and stored at -20 ˚C for further processing.

The MBP vector carries N-terminal His-tag downstream to the MCS. The recombinant His-tagged proteins (MBP-DTP28 and its mutants) were purified by Ni-NTA affinity chromatography on His Trap FF affinity column (GE healthcare) as per manufacture's protocol. Briefly, the protein lysate was diluted with binding (equilibration) buffer, pH 7.4 containing imidazole (30 mM). The diluted protein sample was passed through the column at a flow rate of 2 ml/min. Subsequently, the column was thoroughly washed with wash (Binding) buffer having Imidazole

(30 mM). The protein was eluted using elution buffer containing imidazole (250 mM). The residual imidazole was removed by dialysis against PBS for overnight at 4 ˚C with slow stirring. The cellulose dialysis tubing, benzoylated (Sigma-Aldrich) is used with molecular weight cut off (MWCO) of 2 kDa. The detailed compositions of buffers are given in Table A5 of the appendix. The protein concentration was estimated using Bradford assay.

3.39 Site directed mutagenesis

The different mutants of MBP-DTP28 were created by using a protocol of Q5 site-directed mutagenesis kit (NEB, E0554). The first mutant named as MBP-DTP28A has a mutation G510A and another mutant, MBP-DTP28E has two mutations i.e. G510A and T517E. A negative control mutant MBP-DTP28Neg consists of three mutations, including V511P, Q515G and K526P. The DNA sequence of mutants was PCR amplified using specific template and the forward primer with mutation at desire site. The details of primers and annealing temperature are mentioned in Table A7 of Appendix. The site directed mutagenesis (SDM) control plasmid provided in kit was used to ensure successful working of PCR.

PCR program:

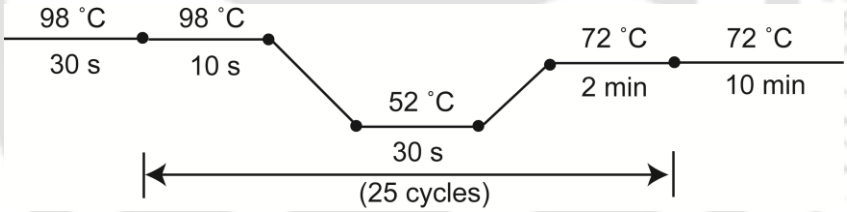

The PCR product was treated with KLD (Kinase, Ligase, *DpnI*) mix for ligation and template removal. The composition of KLD reaction mixture is given below:

Components	Volume
2X KLD buffer	5 µl
KLD enzyme	1 µl
PCR product	2 µl
Water	2 µl
Total volume	10 µl

The KLD reaction mixture (5 µl) was transformed into *Escherichia coli* DH5α by standard chemical transformation. Transformed cells were plated on LBA/Amp plate. The plates are

incubated at 37 ˚C for overnight. The different colonies were picked and plasmids were isolated using HiPurA plasmid DNA miniprep purification kit (HiMedia). Recombinant clones were confirmed by sequencing. Sequence of primers and reaction conditions used are given in appendix (Table A7).

3.40 Solid-phase ELISA:

The binding of peptides or recombinant proteins (MBP-peptides) to HB-EGF was checked by solid-phase ELISA in 96-well plate. An ELISA plate was coated with synthetic peptides or purified MBP-peptides. After overnight incubation at room temperature and 2 h incubation of blocking buffer containing 2% BSA in Phosphate Buffer Saline (PBS), samples were washed once. For binding, 200 ng/well recombinant human HB-EGF (R&D Systems) was used and incubated for 4 h at room temperature. The bound HB-EGF was detected using Anti-HBEGF antibody (R&D Systems) and followed by goat Anti-mouse HRP conjugate (Sigma-Aldrich) secondary antibody. ELISA was developed by using o-phenylenediamine dihydrochloride (OPD, sigma) substrate solution and stopped with 50 µl 8N H_2SO_4. The absorbance was taken at 492 nm in a microplate reader (TECAN, Infinite M200 PRO). The composition of substrate solution is given in table A5 (Appendix).

For competitive assay, the 2 µg/well peptide was coated for overnight at room temperature. After blocking (2% BSA in PBS), HB-EGF (200 ng/well) along with increasing concentration of RDT (0-2 µg/well) or mutant peptides (0-20 µg/well) were added for binding. ELISA was performed as mentioned above.

3.41 Surface Plasmon Resonance

The kinetic of binding study was estimated using SPR-based biosensor (Biacore X100 system (Biacore, GE). The recombinant human HB-EGF was covalently immobilized on CM5 chip by using an amine coupling kit according to manufacture protocols. Briefly, immobilization involves activation of carboxymethyl groups on a dextran-coated chip by reaction with N-hydroxysuccinimide, followed by covalent bonding of the ligands to the chip surface via amide linkages and blockage of excess activated carboxyl with ethanolamine.

The sensor chip was equilibrated with 10 mM phosphate buffer (pH 7.4). The surface was activated by passing 1:1 mix of 0.4 M EDC & 0.1 M NHS, at a flow rate of 10 µl/min for 7 min. Recombinant HB-EGF in PBS was added to 10 mM sodium acetate coupling buffer (final conc. of protein = 50 µg/ml, pH = 5.5) and immobilized for 10 min with default flow rate. The

immobilized amount of ligand was approximately 1400 RU to secure efficient binding. Excess activated groups were blocked using a 7 min injection of 1 M ethanolamine, pH 8.5, at a flow rate 10 µl/min. The detailed compositions of buffers are given in Table A5 of the appendix.

The analyte such as MBP-DTP28 and its mutant were injected with varying concentration from 0 to 1 µM at 25˚ C. The data recorded for 3 min of association and 10 min of dissociation. To remove non-specific interaction, the assay channel was subtracted by control channel. The kinetic constant was determined by BIAevaluation 3.1 software with nonlinear fitting, the 1:1 (Langmuir) binding model was used where $K_D=k_d/k_a$.

3.42 Protein extraction from mammalian cells

Total protein from mammalian cell lines was isolated using RIPA buffer (Appendix table A5). RIPA buffer contains a cocktail of protease inhibitor, PMSF (1 mM); phosphatase inhibitor, sodium orthovanadate (1 mM) and sodium fluoride (50 mM). The DMEM media were discarded from culture plates and cells were washed with ice-cold PBS to remove the residual media. 150 µl RIPA buffer was added to each flask and incubated on ice for 5 min. Then, cells were scrapped and pooled in a tube. Cells were lysed by sonication at 20% amplitude for 10 s. Subsequently, it was centrifuged at 10, 000 rpm for 15 min at 4 ˚C. The supernatant was saved and pellet discarded. SDS-PAGE sample loading buffer was added in 100 µl protein lysate, followed by boiling for 3 min at 100 ˚C and stored at -80 ˚C. The protein concentration was estimated using Lowry's method.

3.43 Protein estimation by Lowry's method

The concentrations of protein lysate used for western blotting were estimated by Lowry's method (175). 10 µl of protein lysate is added in 190 µl water. Then, 100 µl diluted protein sample was mixed with 250 µl of freshly prepared complex forming reagent (Lowry C). The composition of Lowry C is given in Table A5 of Appendix. The samples were mixed properly and incubated at room temperature for 10 min. Folin–Ciocalteu reagent (25 µl) which consists of sodium tungstate molybdate and phosphates was added and mix well. This reaction mixture was incubated for 30 min at room temperature in the dark. After incubation, 150 µl of the reaction mixture from each sample was transferred to 96-well plate and the absorbance was measured at 660 nm.

3.44 Western blotting

The MDA-MB-468 cells were seeded (2 x 10^5 cells/well) in 6 well plates (Nunc, Thermoscientific). The MBP-peptides (20 nM), RDT (20 nM) and only MBP (20 nM) pre-incubated with HB-EGF (0.5 nM) for 2 h at 4 ˚C. Cells were treated with these samples for 15 min at 37 ˚C in 5% humidified CO_2 incubator. After treatment, media were removed and cells were washed with TBS. Cells were lysed with RIPA buffer followed by sonication at 25% amplitude, for 10 s and centrifuged at 12,000 rpm at 4˚C for 15 min. The protein concentration was determined by Lowry's method. Protein lysate (5 µg) were separated by 12% SDS-PAGE and transferred to polyvinylidene fluoride membranes (FloroTrans, PALL). Nonspecific binding was blocked with 3% bovine serum albumin in PBS (pH 7.4) (Sigma Aldrich) containing 0.1% Tween 20 (HiMedia) for 2 h at room temperature. The membrane is incubated with rabbit phospho-p44/42 MAPK (phospho-ERK1/2) (1:3000 dilution; CST) or rabbit p44/42 MAPK (ERK1/2) (1:3000 dilution; CST) overnight at 4˚C, followed by incubation with goat anti-rabbit IgG HRP linked secondary antibodies (1:5000 dilution; CST). Histone H3 primary antibodies (1:4000 dilution; CST) used as internal control. Protein level was detected using super signal west dura kit (Thermo scientific). The detailed compositions of buffers are given in Table A5 of the appendix.

3.45 Data Analysis

SigmaPlot was used to create graphs and for all statistical analysis. Wherever required, means of multiple data points, from repeated experiments, are shown. Error bars represent standard deviation in the data. One-way ANOVA was used.

*Details of common reagents used in this work along with their source are given in the appendix.

4 Results and Discussion

SECTION I:

Development and characterization of drug delivery system using RDT

Synthesis of PLGA Nanoparticles

↓

Coating of PLGA Nanoparticles with RDT

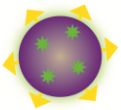

↓

Characterization of PLGA Nanoparticles

↓

Studies on cellular uptake of RDT coated NPs

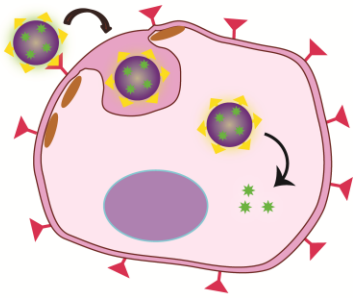

↓

Studies on receptor mediated cellular uptake of RDT-coated NPs

↓

Effect of enhanced uptake of drug through RDT- coated NPs on drug potency

4.1.1 Synthesis of polymeric nanoparticles

Nanoparticles were synthesized using organic polymer poly (D,L-lactide-co-glycolide) (PLGA). PLGA is FDA approved, biodegradable and non-toxic polymer (176). PLGA nanoparticles (NPs) were synthesized by the emulsification solvent evaporation method (166). We have synthesized PLGA NPs using two different methods.

In the first method, PLGA dissolved in dichloromethane was added dropwise in 0.5% polyvinyl alcohol (PVA) under continuous sonication. Here, PVA was used as a non-ionic emulsifying agent. During synthesis, fluorescent dye was added for tracking the cellular uptake of NPs. Excess of solvent was removed by washing with water. Subsequently, NPs was dried by vacuum drying.

In another method, PLGA dissolved in chloroform was added dropwise in 0.5% polyvinyl alcohol (PVA) under continuous sonication. During synthesis either fluorescent dye, Rhodamine 123 was added for tracking the cellular uptake or drug, Irinotecan was loaded for cytotoxicity studies. Excess of solvent was removed by washing with water. Subsequently, NPs was dried by vacuum drying. The schematic diagram of nanoparticle synthesis is shown in Figure 4.1.

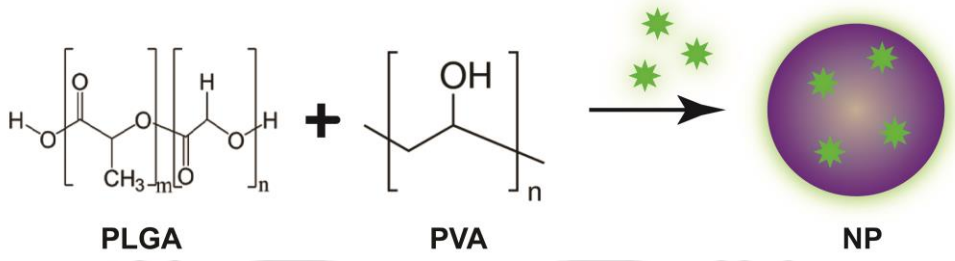

Figure 4.1: Schematic representation of nanoparticle synthesis. PLGA nanoparticles (NPs) were synthesized by the emulsification solvent evaporation method. Rhodamine 123 or drug is loaded for different purpose of a study. Recombinant RDT was surface adsorbed on NPs.

Comparison of NPs size prepared by different methods:

The size and surface morphology of NPs synthesized by the method I and method II were analyzed by TEM. From TEM analysis, average diameter of NPs from Method I and Method II were observed as 307.11 ± 35 nm and 17.51 ± 2.18 nm, respectively (Figure 4.2). The organic phase is emulsified under sonication in a dispersing phase consisting of PVA in water. During this process, organic solvent evaporates form solid spherical particles are formed. The size of the particles would depend upon rate of evaporation of organic solvent, rate of coalescence of emulsified droplets, extent or duration of sonication.

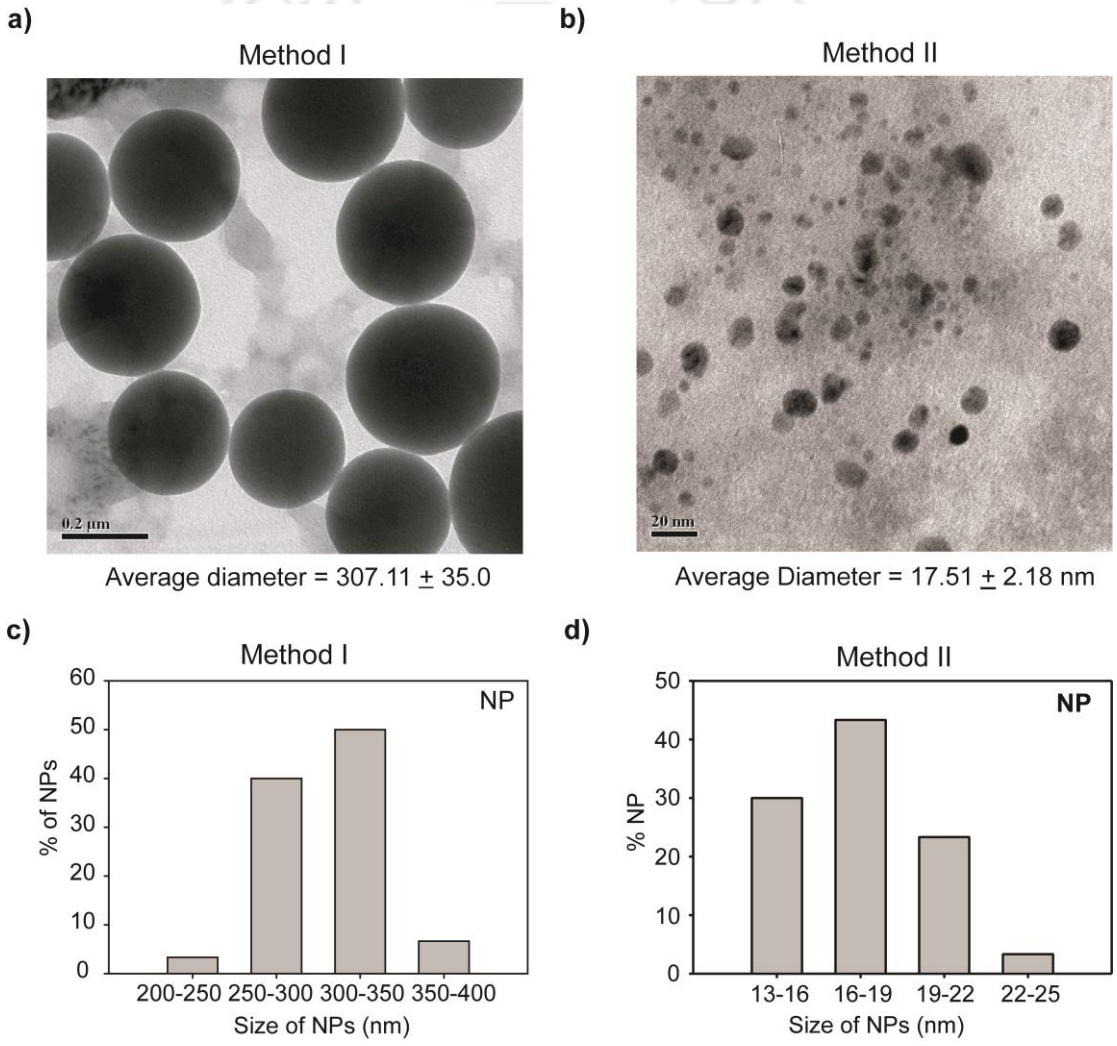

Figure 4.2: TEM to compare size of NPs. TEM images of NPs synthesized from a) Method I b) Method II. Histogram showing size distribution of NPs synthesized from c) Method I d) Method II. The size of NPs synthesized from the method I was larger than the method II.

The boiling point of DCM and chloroform are 39.6 ˚C and 61.2 ˚C, respectively. Therefore, DCM evaporates faster than chloroform and does not give enough time for the sonication to break the emulsified droplets in smaller one. This results in nanoparticles of bigger size. Therefore, NPs synthesized from method I is larger than method II.

Furthermore, hydrodynamic diameter of NPs synthesized from the method I and Method II were calculated using dynamic light scattering (DLS). The average hydrodynamic diameter of NPs synthesized from the method I and method II were 354.9 nm and 154.9 nm, respectively (Figure 4.3).

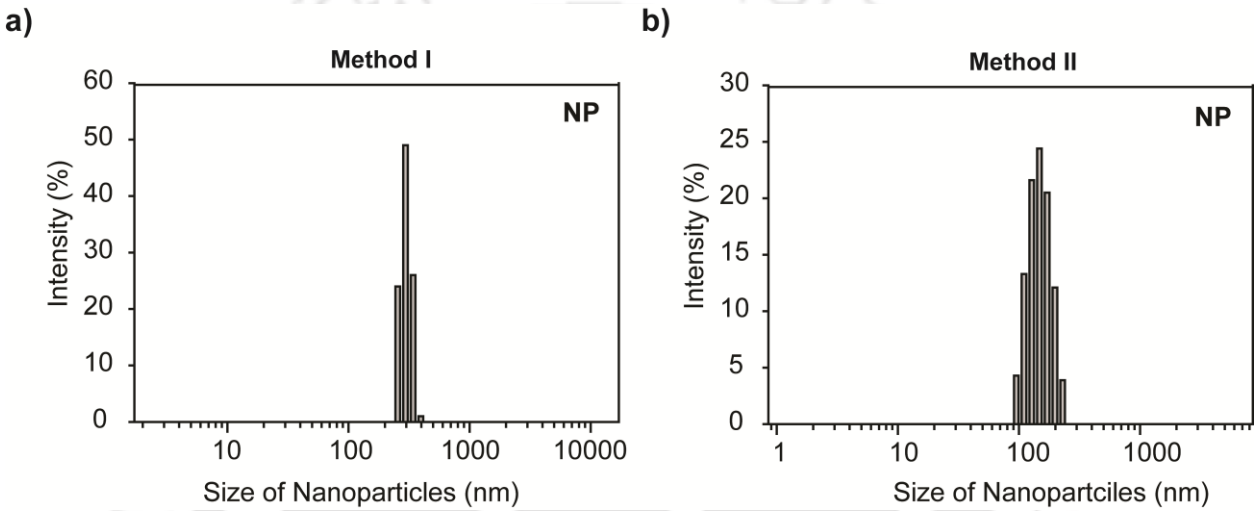

Figure 4.3: DLS to compare the hydrodynamic diameter of NPs. Histogram shows size distribution of a) Method I and b) Method II.

The cellular uptake of nanoparticles depends on the size of nanoparticles (177, 178). The nanoparticles synthesized from method II are of small size, which is best suited for cellular uptake studies. Therefore, smaller size nanoparticles were used to perform all the experiments.

4.1.2 Coating of PLGA nanoparticles with recombinant receptor binding domain of Diphtheria toxin, RDT

Expression and purification of recombinant RDT:

Diphtheria toxin consists of three independent domains: N-terminal catalytic domain (C-domain), C-terminal receptor-binding domain (R-domain), and T-domain (3). The R-domain is non-toxic and binds to human HB-EGF (89). Earlier in our lab, recombinant receptor binding domain of DT (RDT) was cloned into pET-22b vector. pET-22b has pel B leader sequence at N-terminal and

His-tag at C-terminal. RDT was cloned between *BamH I* and *Xho I* restriction sites in a frame with pel-B leader sequence and His-tag. The pET-22b-RDT construct is shown in Figure 4.4a. The construct was transformed in *Escherichia coli* BL21 (DE3) by standard chemical transformation. RDT was expressed by induction with 0.5 mM IPTG for 8 hours at 28 ˚C. The cells were harvested by centrifugation and purified using affinity chromatography. The whole cell lysate was purified using His-Trap FF affinity column (GE Healthcare) as per the manufacturer's protocol. RDT was eluted with 500 mM Imidazole. Residual imidazole was removed by dialysis against PBS (pH 7.4). The recombinant RDT was analyzed by SDS-PAGE as shown in Figure 4.4b. The expected molecular weight is ~20 kDa.

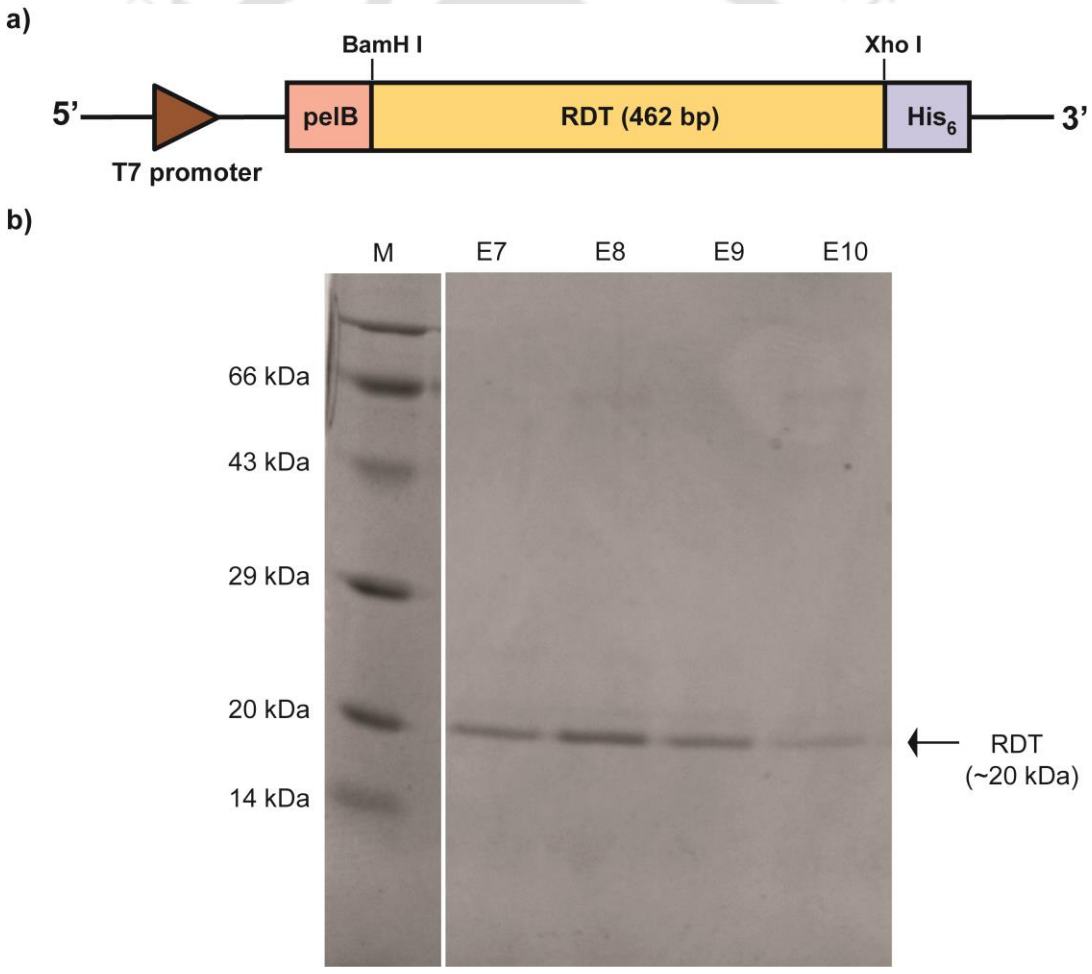

Figure 4.4: Expression of recombinant RDT. (a) Design of the construct of pET-22b RDT (b) SDS-PAGE of purified RDT in eluted fractions E7 to E10. M: protein marker.

Coating of PLGA nanoparticles by RDT:

The synthesized nanoparticles were coated with recombinant RDT. The NPs (500 µg) were incubated with 200 µl RDT (50 µg/ml) for 2 h at 37 ˚C. The RDT gets adsorbed on NPs. The schematic diagram of nanoparticle synthesis is shown in Figure 4.5.

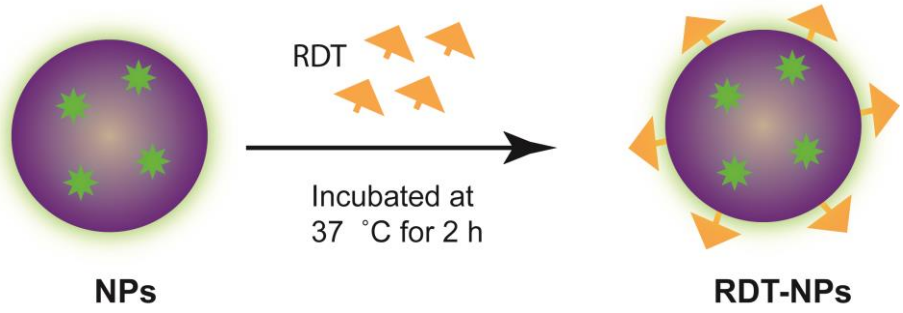

Figure 4.5: Coating of PLGA nanoparticles by RDT. The synthesized NPs were coated with RDT by incubation at 37 ˚C for 2 hours.

Further, coating of NPs with RDT was confirmed by different techniques such as UV-spectroscopy, FT-IR spectroscopy, and ELISA.

Detection of RDT on NPs by UV-Visible spectroscopy:

In UV-spectroscopy, the fixed amount of nanoparticles (500 µg) was incubated with varying concentration of recombinant RDT (0-25 µg/ml). After 2 h of incubations, RDT-coated NPs were centrifuged at 8,000 rpm for 5 min at room temperature. The uncoated protein present in supernatant was discarded and pellet was resuspended in 1 ml PBS (pH 7.4). The absorbance of resuspended NPs is measured at 280 nm. It has been observed that there is an increase in absorbance at 280 nm with increase in the concentration of RDT used (Figure 4.6). This shows that NPs were coated with increasing amount of RDT.

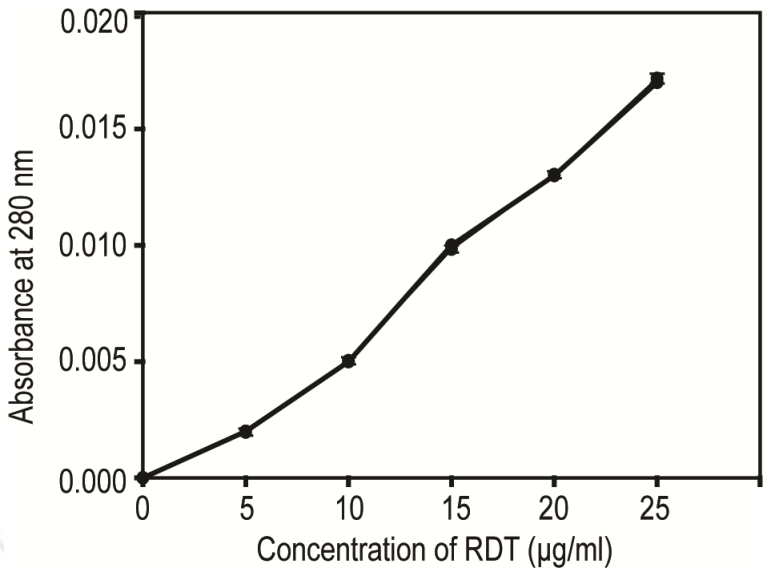

Figure 4.6: Adsorption of RDT on PLGA NPs was detected by UV-Vis spectroscopy. NPs incubated with increasing concentrations of RDT for coating. Coated NPs were resuspended in PBS and absorbance was measured at 280 nm. The absorbance of an equivalent amount of uncoated NPs was subtracted for correction in reading.

Detection of RDT on NPs by ELISA:

Coating of NPs by RDT was further confirmed by ELISA. The recombinant RDT used in this work has His-tag. PLGA NPs were incubated with increasing amount of RDT for 2 h, and bound RDT was detected by mouse anti-His antibody, followed by anti-mouse HRP-conjugate (Figure 4.7a). The data of this experiment is shown in Figure 4.7b. It shows dose-dependent adsorption of RDT on NPs. The dose-dependent binding of RDT to NPs has a hyperbolic behavior similar to Langmuir adsorption model. With this experiment, we have also optimized the amount of RDT required for coating NPs. We have used 10 µg of RDT to coat 500 µg of nanoparticles for routine experiments.

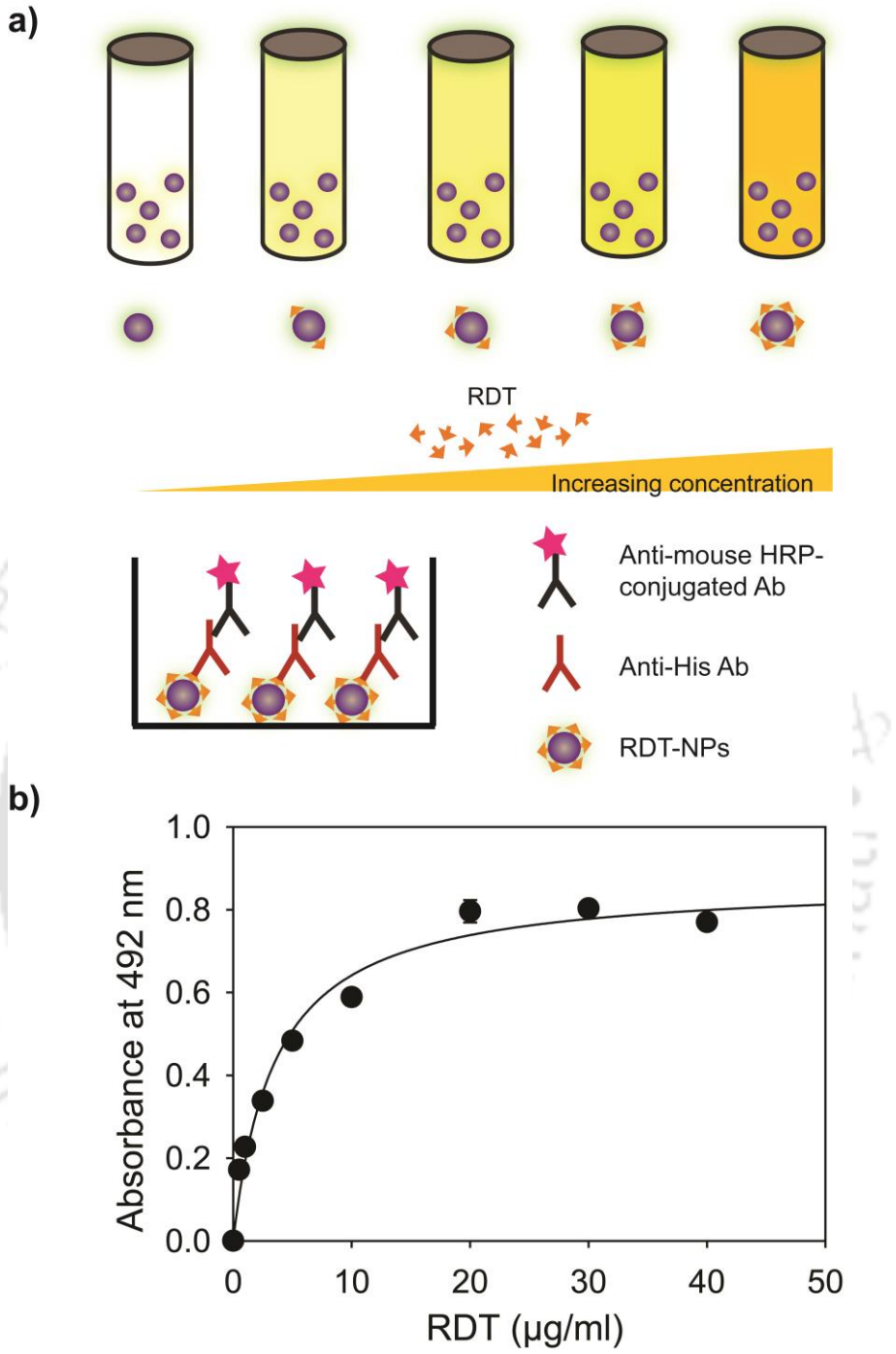

Figure 4.7: RDT adsorbed on NPs was detected by ELISA. (a) Cartoon diagram showing dose-dependent experiment in which fixed amount of NPs was incubated with different concentration of RDT. RDT-NPs detected using anti-His antibody followed by anti-mouse HRP conjugated antibody. b) Data showing the increase in absorbance of RDT-NPs with increase in concentration of RDT. Filled circles represent average of data from three wells. The data was fitted to a rectangular hyperbola (solid line).

Detection of RDT on NPs by FT-IR spectroscopy:

FT-IR spectroscopy was also used to check coating of NPs by RDT. In FT-IR spectroscopy, it has been reported that PLGA shows a prominent peak of carbonyl stretching in the range of 1690–1760 cm^{-1}. In addition to that, PLGA shows strong C–O stretching band near 1100 cm^{-1} (179) In our analysis, PLGA NPs shows peak of C═O stretching bond appears at 1755.05 cm^{-1} (Figure 4.8a). RDT-NPs shows exclusive peaks of amide bonds due to protein coating. A peak at 1647.00 cm^{-1} is due to amide I having dominant C═O stretching bond and peak at 1546.18 cm^{-1} is due to amide II bond having N–H bend and C–H stretch (Figure 4.8b) (180).

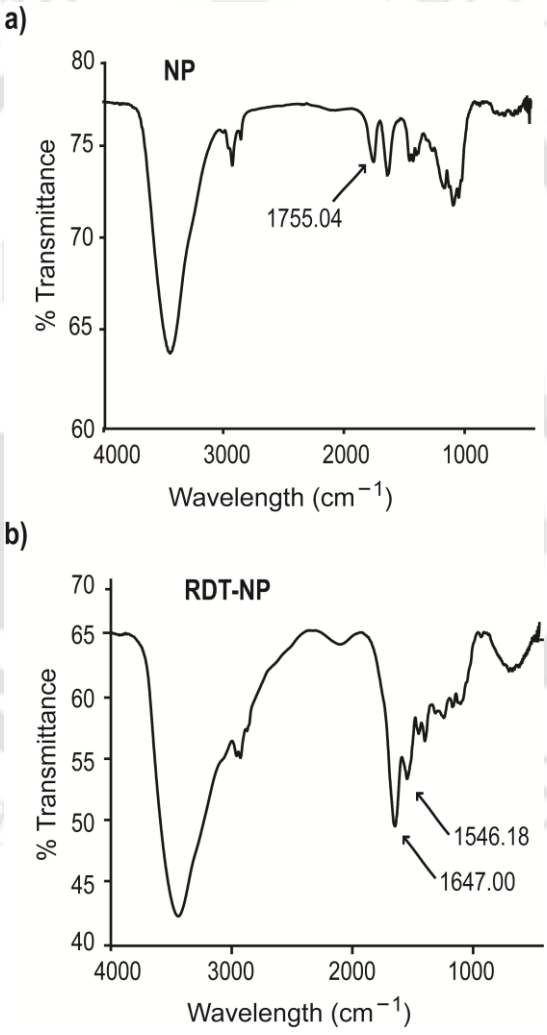

Figure 4.8: Confirmation of NPs coating by RDT using FT-IR spectroscopy. (a) and (b) show FT-IR spectra of PLGA NPs and RDT-coated PLGA NPs, respectively. PLGA NPs showed a peak of C═O stretching bond at 1755.05 cm^{-1} and RDT-NPs shows peaks at 1647.00 cm^{-1} due to amide I and at 1546.18 cm^{-1} due to amide II bond.

Estimation of RDT on NPs by Bradford's reagent:

In general, we used 10 µg of RDT to coat 500 µg of nanoparticles. But, 100% of RDT may not get utilized for coating over NPs. Some percentage of RDT would remain unbound to NPs. Therefore, we have calculated the amount of RDT bound to NPs using Bradford assay. A standard graph was plotted using BSA solution as standard as shown in Figure 4.9. Bradford's reagent was added in NPs and RDT-NPs resuspended in PBS. The absorbance was taken at 595 nm. It has been calculated that 6.3 µg of RDT was surface absorbed on 500 µg of nanoparticles. From the standard curve, we calculated that 6.3 µg of RDT was adsorbed on 500 µg of nanoparticles. This is equivalent to 12.6 ng RDT per microgram of NPs.

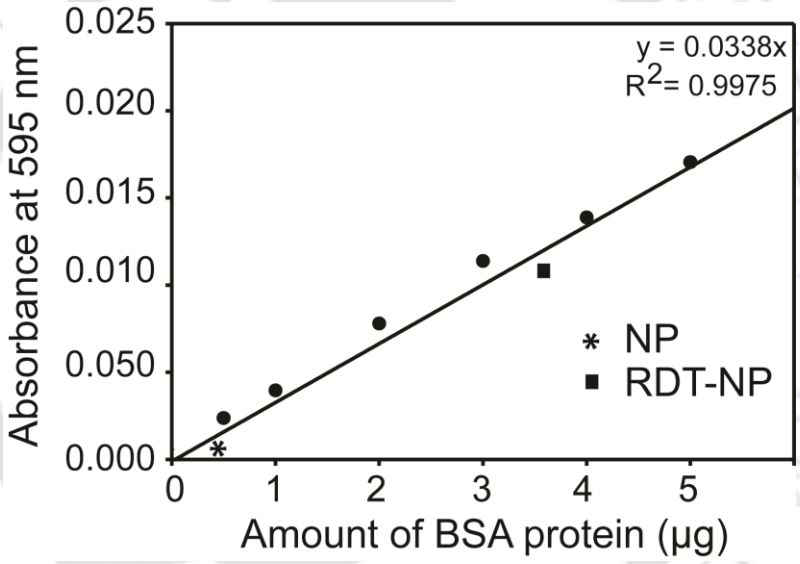

Figure 4.9: The amount of protein bound to NPs was estimated using Bradford assay. A standard graph was plotted using BSA solution as standard (filled circle and straight line). NPs (star) and RDT-NPs (filled square) were resuspended in PBS and Bradford's reagent was added and absorbance was measured. Amount of protein was calculated from the standard curve. The estimate of adsorbed RDT was corrected for reading from NPs alone.

Stability of RDT coating on NPs by ELISA:

We investigated the stability of coating by RDT on NPs using ELISA. Nanoparticles coated with RDT were incubated for different durations in serum-free media at 37 °C. Subsequently, RDT bound to NPs was detected by ELISA. As shown in Figure 4.10, coating of RDT on NPs is stable even after 24 h of incubation in serum-free media.

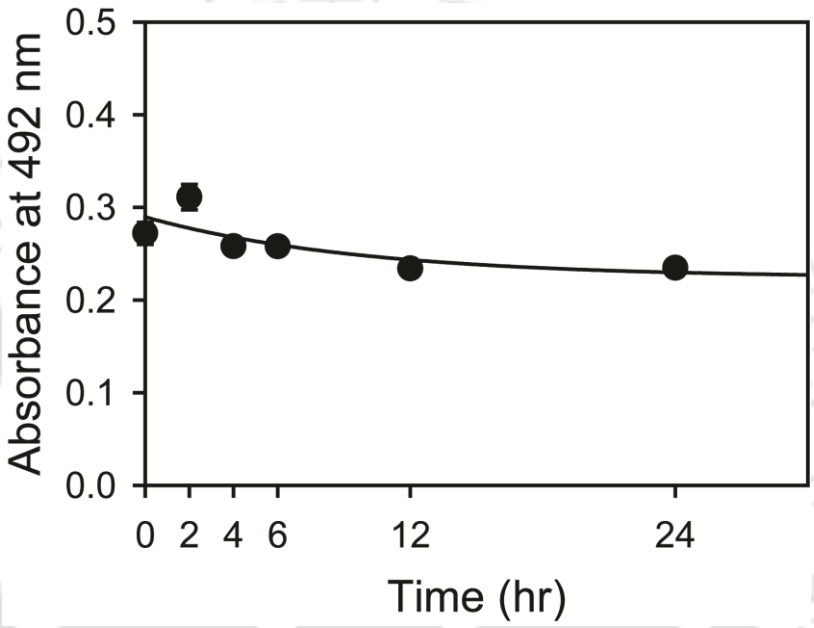

Figure 4.10: Stability of RDT coating on NPs. Time-dependent experiment in which NPs coated with RDT were incubated in serum-free media for different durations. Filled circles are experimental data points. Filled circles represent average of data from three wells. The data were fitted to an exponential decay curve.

4.1.3 Size distribution of RDT-NPs:

The size distribution of NPs and RDT-NPs were determined using TEM and FESEM. The hydrodynamic diameter was calculated using dynamic light scattering (DLS).

The size and surface morphology of NPs and RDT-NPs, synthesized by method II, were analyzed by TEM and FESEM. TEM analysis showed that average diameters of NP and RDT-

NP are 17.51 ± 2.18 nm and 44.32 ± 2.84 nm, respectively (Figure 4.11a). The size distribution of NPs and RDT NPs was also observed (Figure 4.11b).

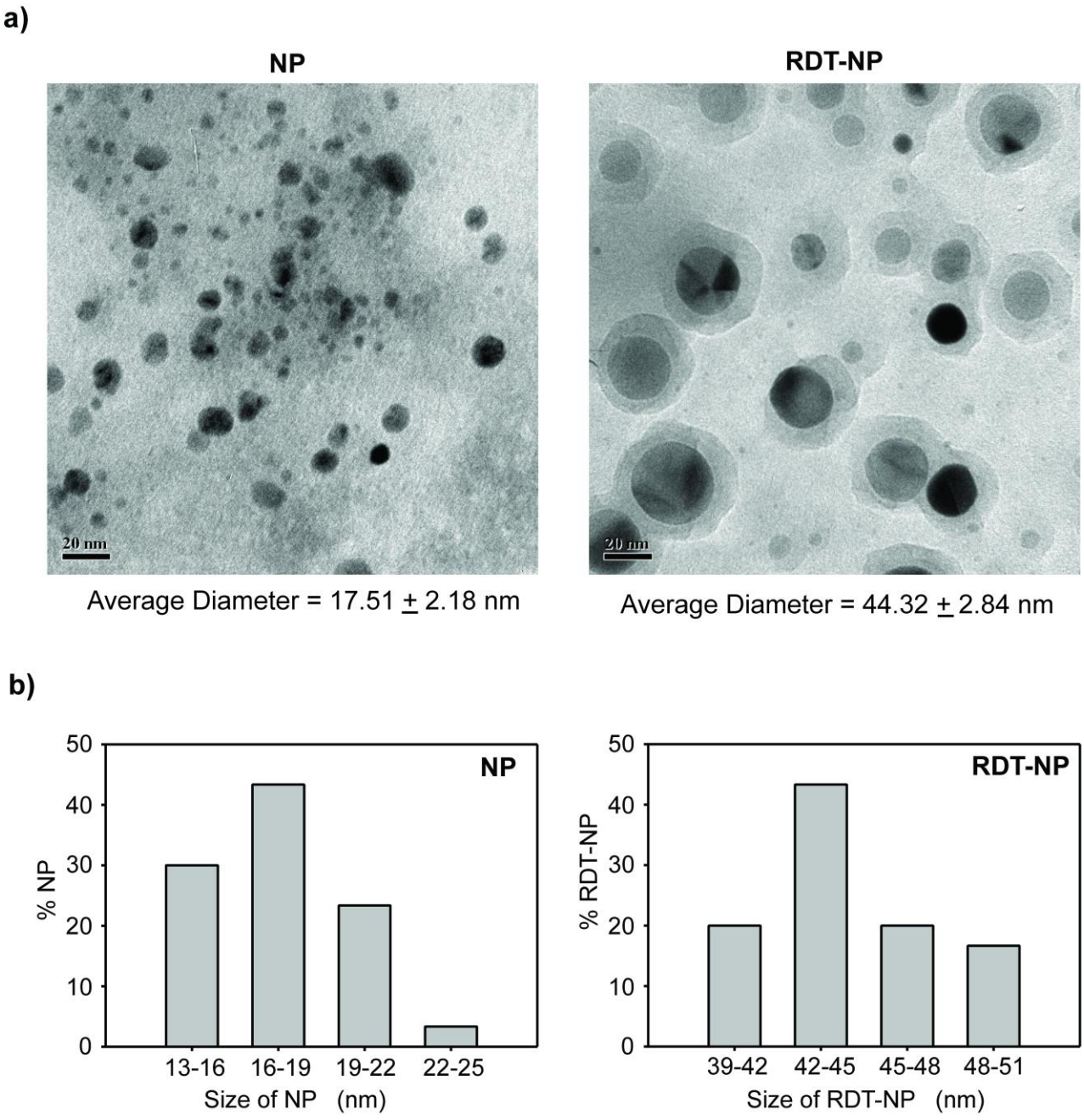

Figure 4.11: TEM to characterize uncoated and RDT-coated PLGA NPs. (a) TEM images of NPs and RDT-coated NPs. (b) Histogram showing size distribution of NPs and RDT NPs as observed in TEM images.

From FESEM analysis, an average diameter of NP and RDT-NP was observed as 33.10 ± 7.29 nm and 54.42 ± 5.14 nm, respectively (Figure 4.12a). The sizes of RDT-NPs are slightly bigger than NPs probably due to protein layer. The size distribution of NPs and RDT NPs was also observed (Figure 4.12b).

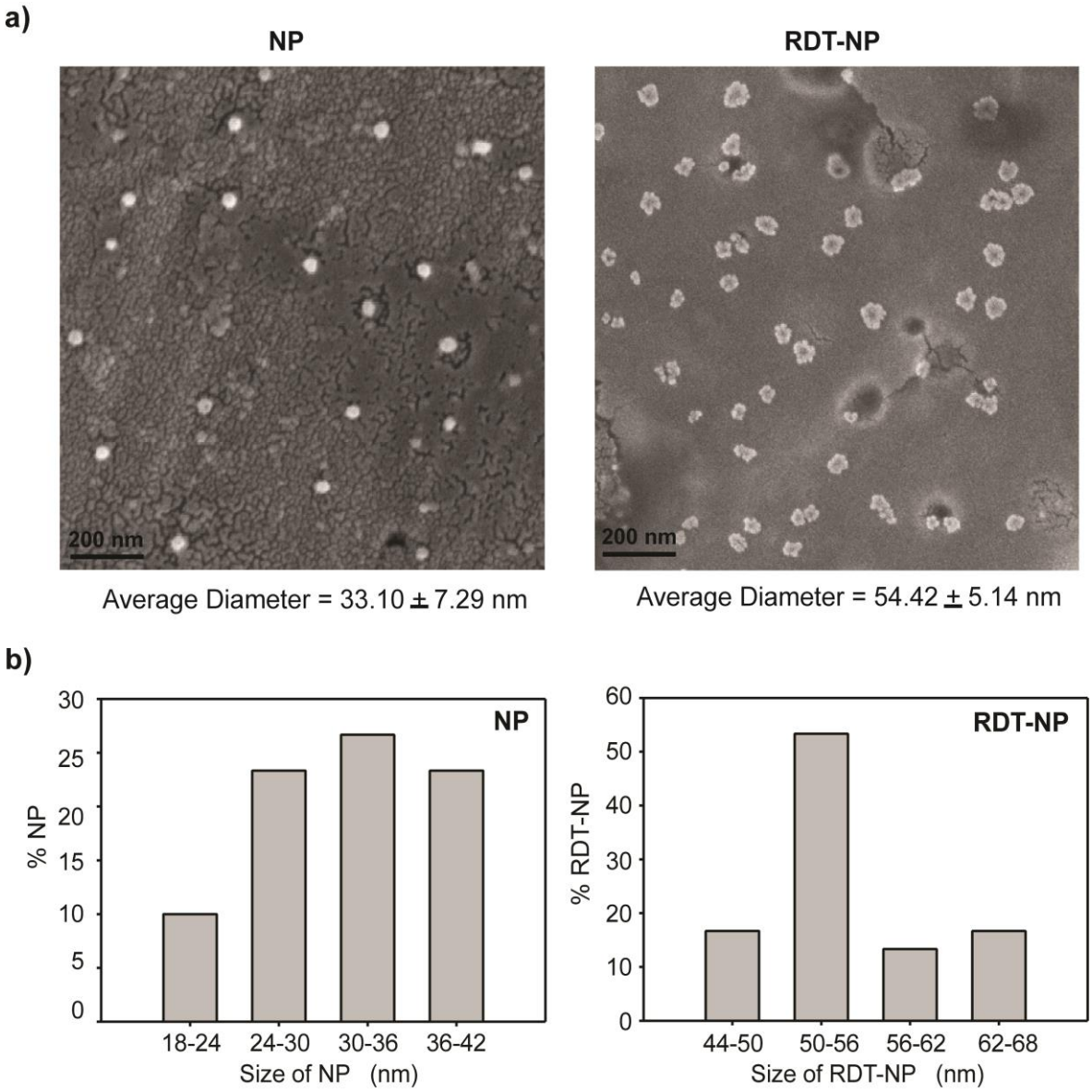

Figure 4.12: FESEM to characterize NPs and RDT-NPs. (a) FESEM images of NPs and RDT-coated NPs. (b) Histogram showing size distribution of NPs and RDT NPs as observed in FESEM images.

Size distributions of these NPs were also measured by DLS. Average hydrodynamic diameter of NPs and RDT-NPs were 154.9 nm and 157.5 nm for NPs and RDT-NPs, respectively (Figure 4.13a, b). Size calculated from DLS is higher than FESEM or TEM analysis. Such size difference is due to layer of hydration around NPs which affects DLS measurement. Such layer of hydration is absent in samples of FESEM or TEM. Additionally, PLGA nanoparticles would dehydrate and may shrink during sample preparation for FESEM or TEM. Cellular uptake of NPs depends upon the size of NPs (178). Coated and uncoated PLGA NPs, prepared in this work, is in the optimal size range for endocytosis (178).

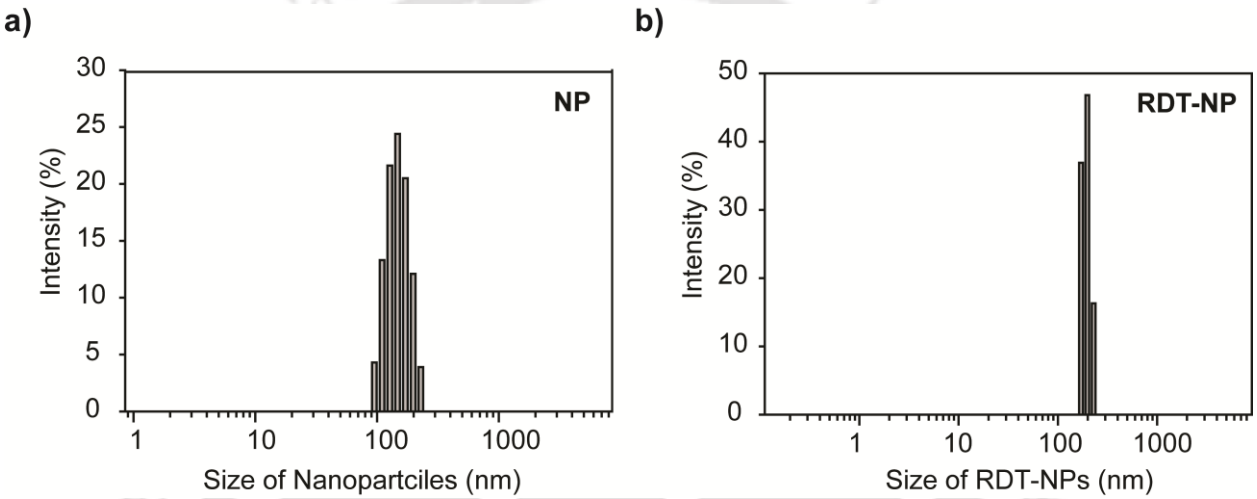

Figure 4.13: Hydrodynamic diameter measured by DLS. Histogram shows size distribution of (a) NPs and (b) RDT-NPs.

The surface charge of nanoparticles is calculated by zeta potential. The zeta potential of NPs and RDT-NPs are found to be −0.127 mV and +0.717 mV, respectively. These NPs are close to neutral. It has been reported that positively charged NPs enhances cellular uptake due to interaction with negatively charged cell membrane (178). However, positive surface charge is not crucial when specific receptor-mediated endocytosis is used for cellular uptake of NPs. In this case, the interactions between the homing molecules on NPs with the receptor on cell surface would play the major role.

4.1.4 Cellular uptake of RDT-NPs

Stability of dye loaded nanoparticles:

NPs loaded with dye, Rhodamine 123 were used for tracing cellular uptake of NPs. Rhodamine 123 may leach out of the PLGA NPs on prolonged storage in an aqueous environment. That will affect the endocytosis assays. So, the stability of dye-loaded nanoparticles was checked using spectrofluorimetry and fluorescent microscope.

Stability of dye-loaded nanoparticles measured using spectrofluorimetry:

To estimate the extent of leaching, we incubated Rhodamine 123-loaded NPs in serum-free culture media, at 37 °C, for different durations, with mild shaking. Subsequently, NPs were separated by centrifugation and resuspended in PBS. Fluorescent intensity of these NPs was measured by spectrofluorimetry.

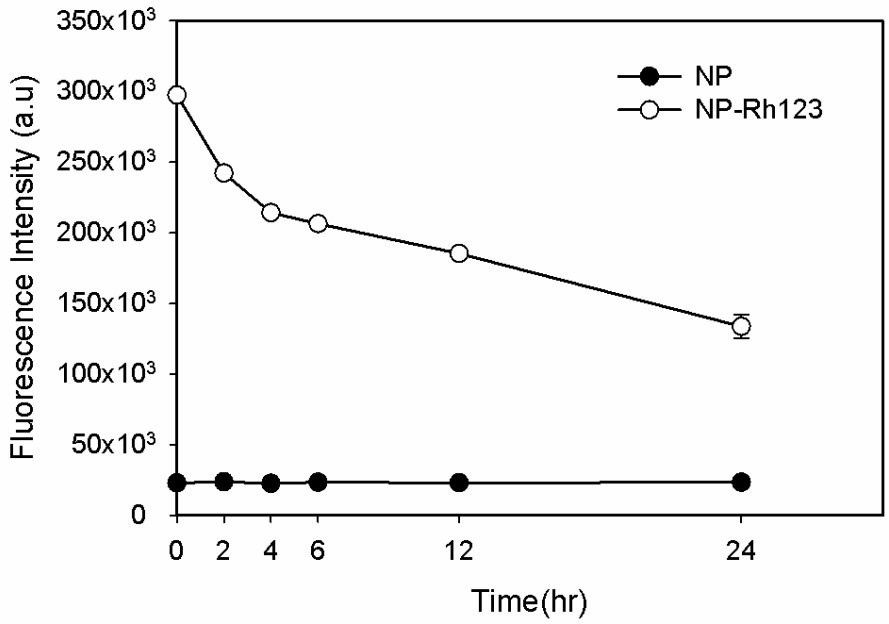

Figure 4.14: Stability of Rhodamine 123 inside NPs was determined by spectrofluorimetry. Fluorescence intensity of Rhodamine 123 loaded NPs (NP-Rh123) and only NPs without any dye (NP) was measured after incubation in serum-free media for different durations.

We observed that with time fluorescence intensity of these NPs decreased (Figure 4.14). However, these NPs retained measurably high fluorescence intensity of 1.5 x 10^5 units even after 24 h of incubation. For cellular uptake studies, we have used freshly prepared NPs and dye-loaded NPs never stayed more than 6 h in an aqueous environment.

Stability of dye loaded nanoparticles determined using Fluorescent microscope:

The fluorescent intensity of the dye, Rhodamine 123 inside NPs was visualized by fluorescent microscope. Rhodamine 123-loaded NPs (250 µg/ml) were incubated in serum-free media at 37 ˚C for different time durations. Subsequently, NPs were separated by centrifugation and resuspended in water. 50 µl samples were dropped on a glass slide and dried at room temperature. Images were taken at 10X magnification by using Eclipse Ti fluorescent microscope (Nikon). B-2E/C filter was used for green fluorescence of Rhodamine 123. We observed that fluorescence of these NPs were visible even after 24 h of incubation in serum-free media (Figure 4.15).

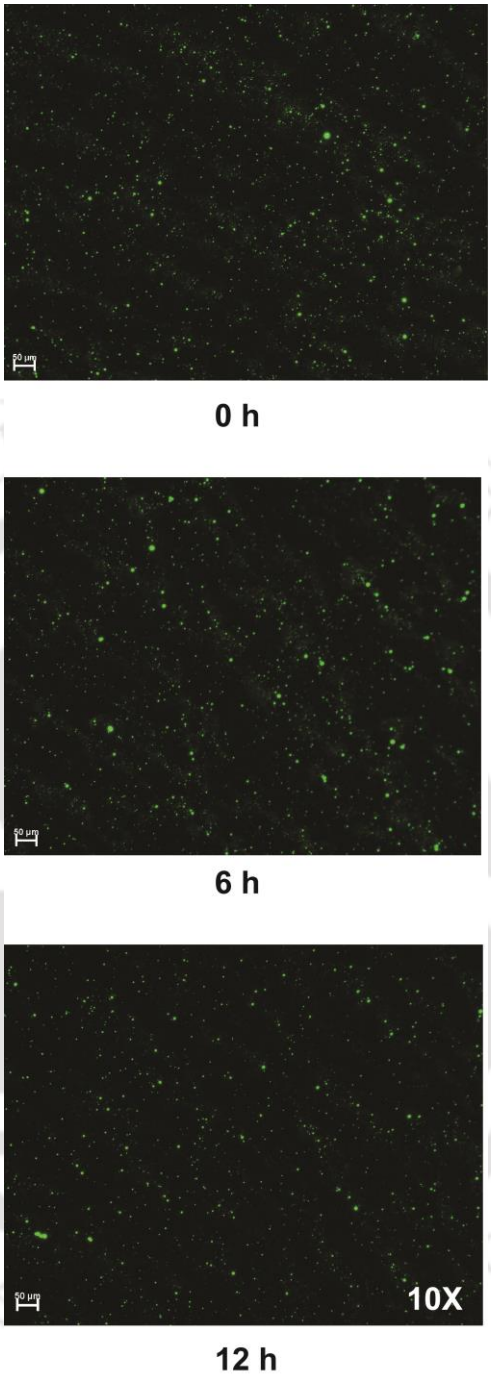

Figure 4.15: Stability of Rhodamine 123 inside NPs was determined by Fluorescent microscope. Fluorescence intensity of Rhodamine 123 loaded NPs was visualized after incubation in serum-free media for different durations. In fluorescence microscope (Nikon Eclipse TiU), B-2E/C filter was used for green fluorescence of Rhodamine 123. Images were taken at 10X magnification.

Cellular uptake of uncoated NPs:

Polymeric NPs can enter without any receptor-mediated process, by fluid-phase endocytosis (177). Therefore, we checked cellular uptake of PLGA NPs in our experimental system and optimized dose and time required for uptake experiments. The uptake of nanoparticles was determined using flow cytometer. The U 87-MG cells were treated with different concentration (0-250 µg/ml) of NPs (Figure 4.16) and at the different time interval (0-6 h) (Figure 4.17) in serum-free medium. It was observed that cells treated with 50 µg/ml concentration of NPs for 2 h are well enough to study cellular uptake of nanoparticles.

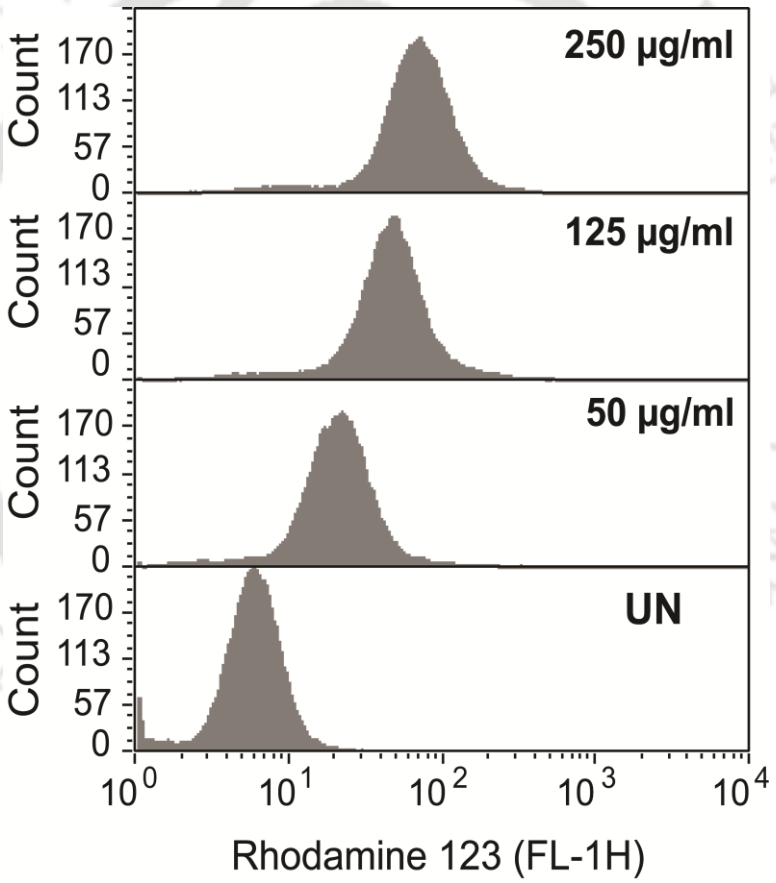

Figure 4.16: Uptake of uncoated PLGA NPs detected by flow cytometer. These NPs were loaded with Rhodamine 123. U 87-MG cells were treated with NPs in a different doses. Histogram of Rhodamine 123 intensity showing enhance uptake of NPs with increasing concentration of NPs (Treatment duration: 2 h). UN: untreated U-87 MG cells.

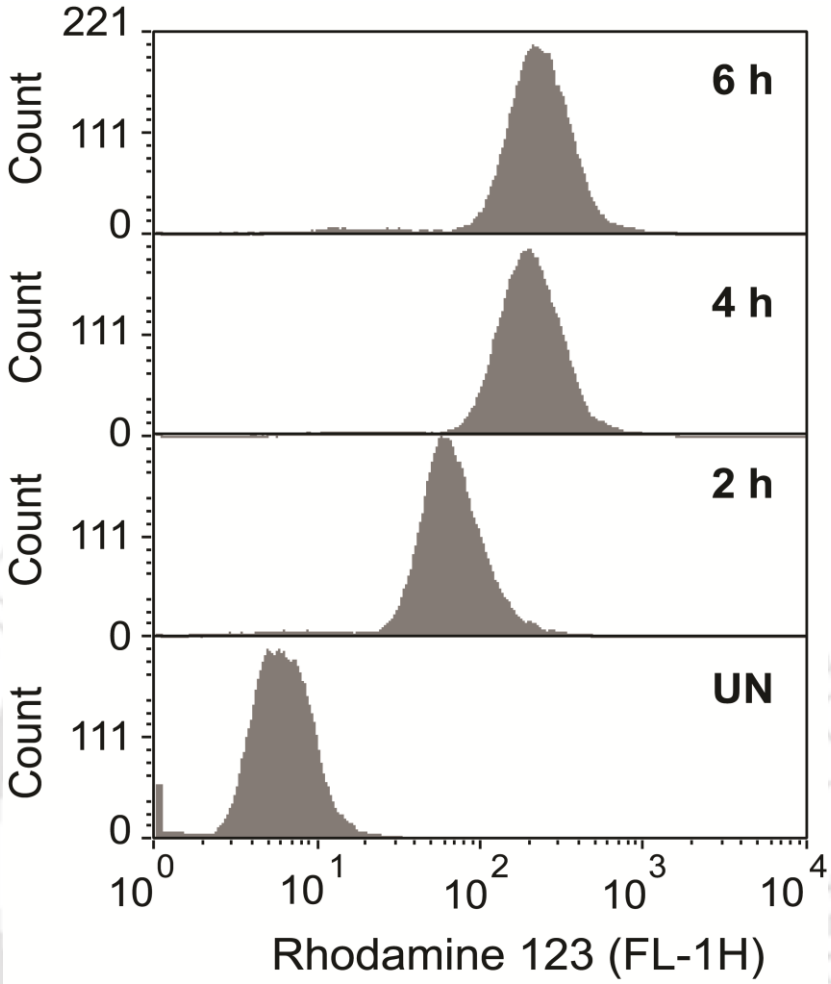

Figure 4.17: Uptake of uncoated PLGA NPs detected by flow cytometer. These NPs were loaded with Rhodamine 123. U 87-MG cells were treated with NPs in a different time intervals. Histogram of Rhodamine 123 intensity showing time-dependent uptake of NPs. 50 µg/ml of NPs were used for the study. UN: untreated U-87 MG cells.

Expression of HB-EGF in U 87-MG:

DT binds with human HB-EGF. We have checked the expression of HB-EGF in U 87-MG cells. The RNA was isolated from U 87-MG cells using Tri-reagent. Subsequently, cDNA was synthesized using verso cDNA synthesis kit. Then, Reverse transcription-PCR (RT-PCR) was performed to check the expression of HB-EGF. We observed that HB-EGF was expressed in U 87-MG cells (Figure 4.18).

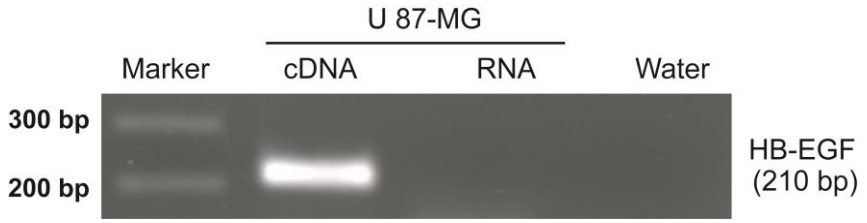

Figure 4.18: Expression of HB-EGF in U 87-MG. RT-PCR was performed using HB-EGF specific primers and the size of PCR product was 210 bp.

Earlier also, it has been reported that human glioma cell line, U-87 MG expresses HB-EGF on cell surface (89). Therefore, we choose U 87-MG cells as a model for study cellular uptake of RDT-NPs. Mouse cells also express HB-EGF. But, DT does not bind to mouse HB-EGF due to sequence variation (2). So, mouse HB-EGF is not sensitive to DT. Therefore, mouse cell line, RAW 264.7, is used as a negative control in these experiments.

Cellular uptake of RDT-coated NPs:

We have performed *in vitro* assays to study cellular uptake of RDT-NPs. In this experiment, three types of NPs, uncoated NPs, BSA-coated NPs (BSA-NPs) and RDT-coated NPs (RDT-NPs), were used. BSA does not have any specific receptor on U-87 MG and RAW 264.7 cells. So, BSA-NPs serve as a negative control in our experiments. We treated both U-87 MG and RAW 264.7 cells with different NPs (50 µg/ml) for 2 h at 37 °C and measured extent of endocytosis by flow cytometer.

Both coated and uncoated NPs are internalized by U-87 MG cells. However, the extent of endocytosis of RDT-NPs was much higher than uncoated and BSA-coated NPs (Figure 4.19). However, both RDT-NPs and BSA-NPs have similar uptake in RAW 264.7 cells (Figure 4.20). These observations indicate that probably RDT-NPs are preferentially internalized by U-87 MG cells through HB-EGF-mediated endocytosis.

In this work, our objective is to investigate whether RDT can facilitate receptor-mediated cellular uptake of nanoparticles. The serum added to culture medium is a cocktail of large number of molecules, many of which are not characterized. It is generally accepted that the molecules present in serum may affect a cell-based experiment in an unexpected fashion. Such interference may make it difficult to draw appropriate conclusions from a cell-based assay. Therefore, these experiments were performed in serum-free medium.

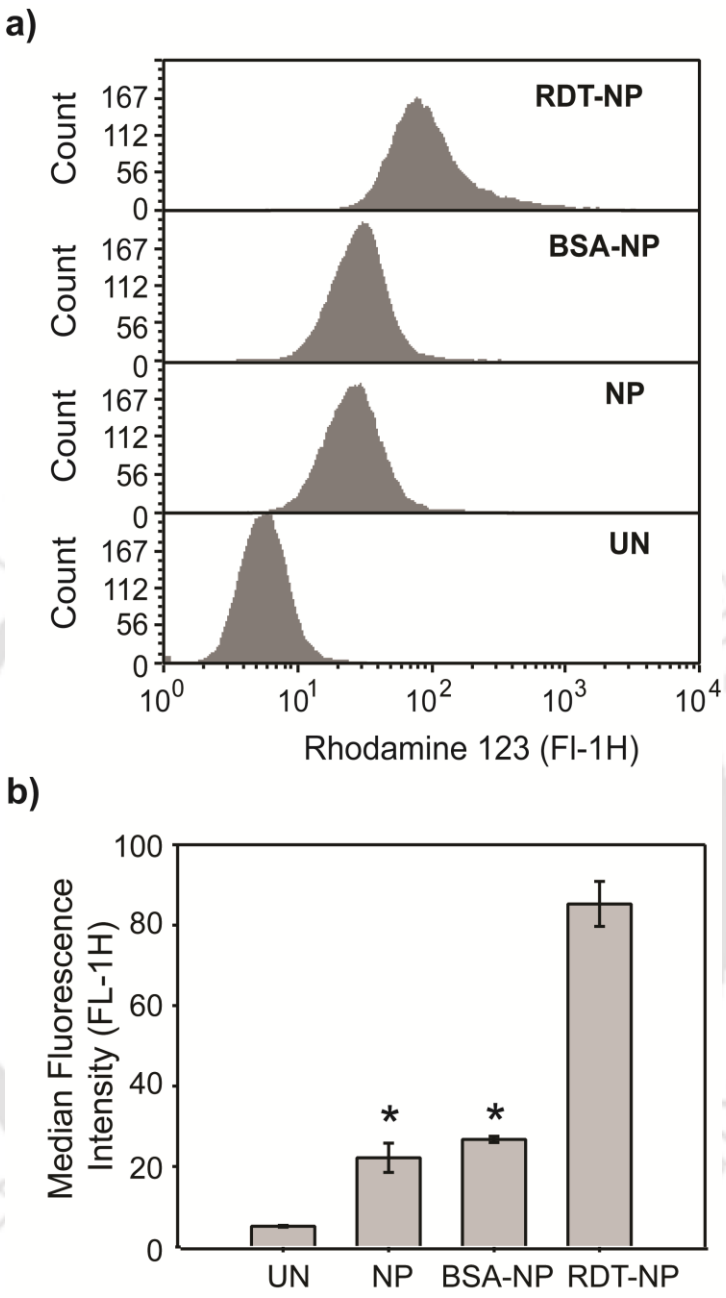

Figure 4.19: Cellular uptake of NPs in U-87 MG cells. Uptake of RDT-coated NPs was greater than BSA-coated NPs and uncoated NPs. These NPs are loaded with Rhodamine 123. (a) Histogram of Rhodamine 123 intensity in different treatment groups in a representative experiment. (b) Median fluorescence intensity of Rhodamine 123 in cells treated with different NPs as calculated from three independent experiments. UN: untreated U-87 MG cells. One-way ANOVA with pairwise comparison: *do not have any significant difference ($p > 0.05$).

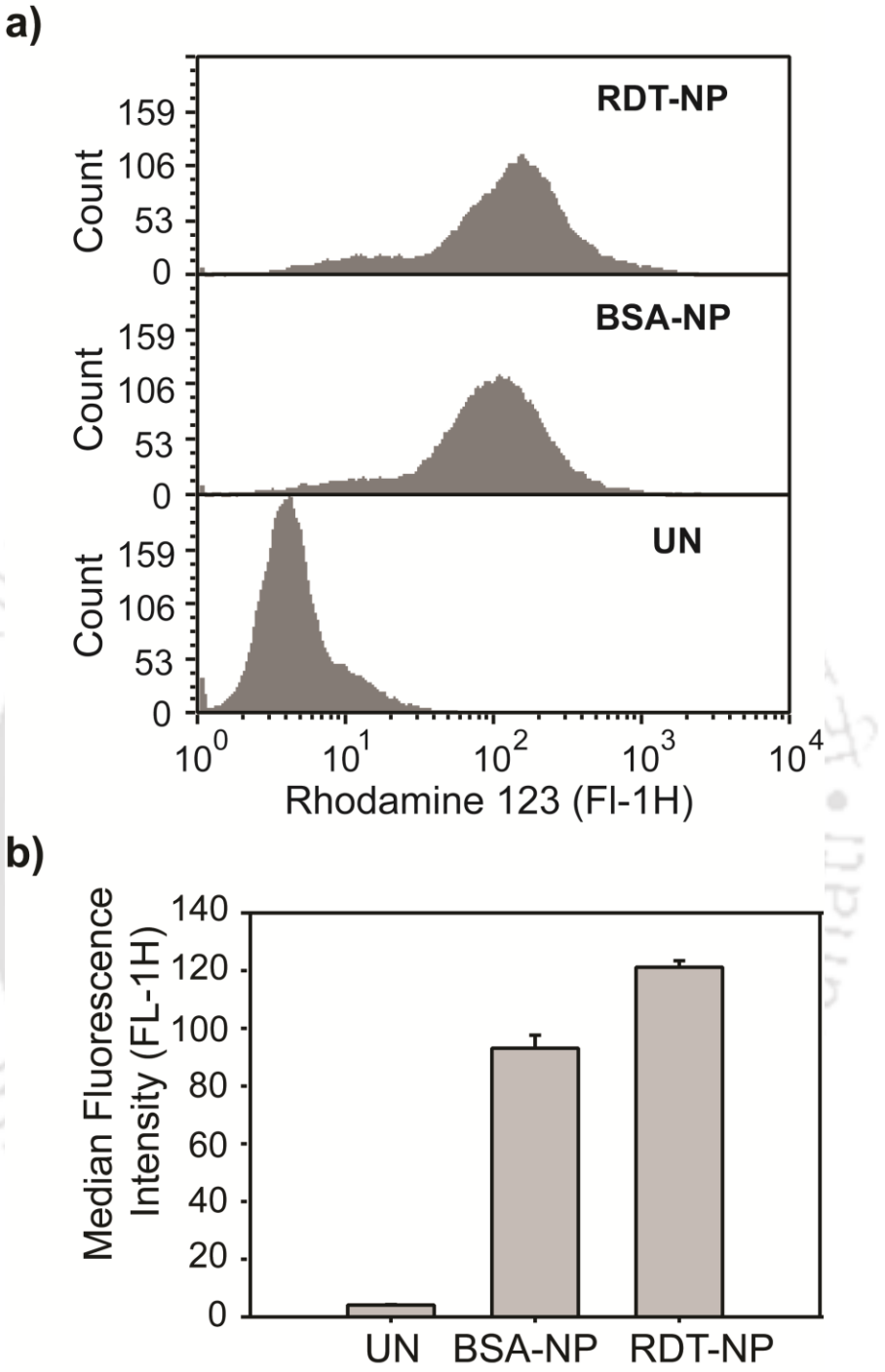

Figure 4.20: Cellular uptake of NPs in RAW 264.7 cells. Uptake of RDT-coated NPs is similar to BSA-coated NPs and uncoated. These NPs are loaded with Rhodamine 123. (a) Histogram of Rhodamine 123 intensity in different treatment groups in a representative experiment. (b) Median fluorescence intensity of Rhodamine 123 in cells treated with different NPs as calculated from three independent experiments. UN: untreated RAW 264.7 cells.

Cellular uptake of RDT-NPs was further detected by fluorescent microscope. U-87 MG cells were treated with Rhodamine 123 loaded BSA- or RDT-coated NPs (50 µg/ml) for 2 h. The results show increased green fluorescence in RDT-NPs treated cells as compared to BSA-NPs (Figure 4.21). This may be due to RDT binds specifically to a cell surface, HB-EGF and internalized through receptor-mediated endocytosis. BSA doesn't have a specific receptor on the cell surface. So, BSA-NPs were internalized only through fluid phase endocytosis.

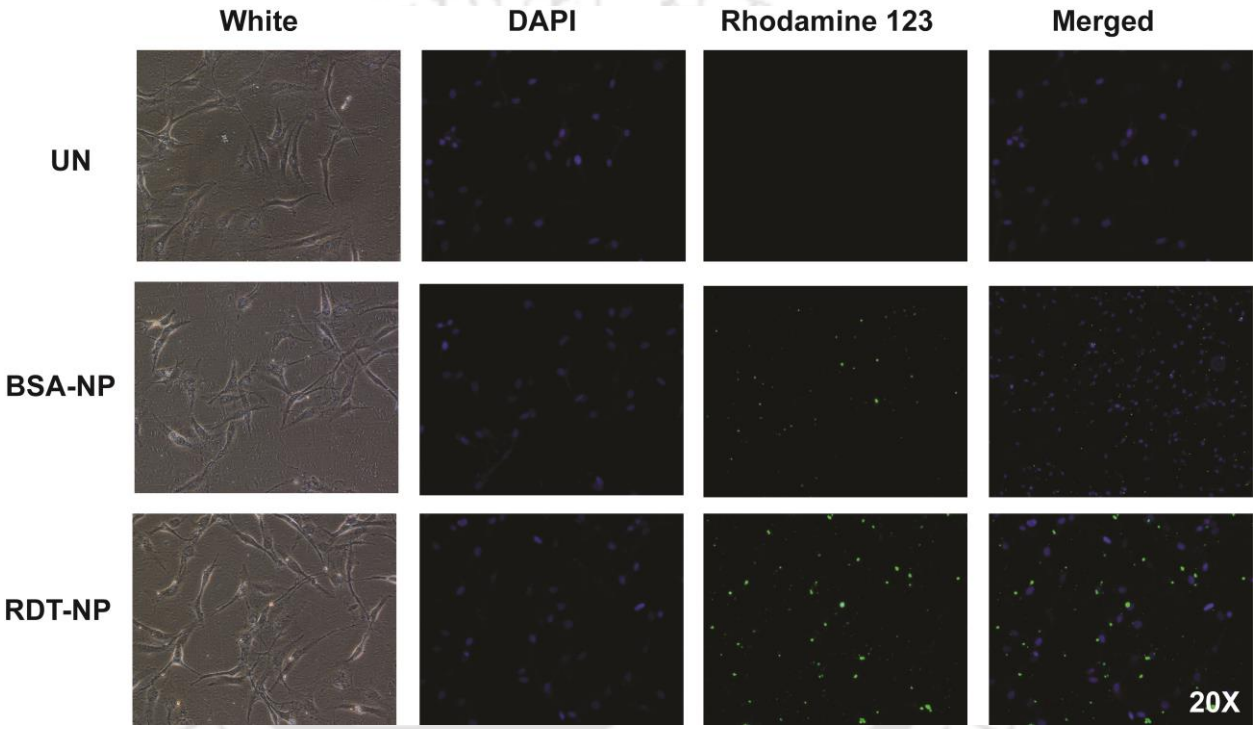

Figure 4.21: Enhanced cellular uptake of RDT-NPs in U 87-MG cells. U-87 MG cells were treated with Rhodamine 123 loaded BSA- or RDT-coated NPs. In fluorescence microscope (Nikon Eclipse TiU), nucleus was counter-stained with DAPI. UV-2E/C filter was used. B-2E/C filter for green fluorescence was used for Rhodamine 123. Images were taken at 20X magnification.

4.1.5 Receptor-mediated cellular uptake of RDT- coated NPs

Further, we performed a competitive assay to confirm that enhanced uptake of RDT-NPs involves HB-EGF-mediated endocytosis. We have performed endocytosis assay in presence and absence of excess free RDT. Free RDT will compete with RDT on the surface of NPs for binding to cell surface HB-EGF. This should lead to decrease in binding of RDT-coated NPs to HB-EGF and should reduce endocytosis of RDT-coated NPs. The extent of endocytosis was estimated using Spectrofluorometer.

In this experiment, U 87-MG cells were prior incubated in presence and absence of excess, free RDT (8 µg/ml) for 30 minutes, followed by treatment of BSA-NPs and RDT-NPs. After the treatment, cells were properly washed with PBS (pH 7.4), so that RDT-NPs bound to cell surface can be removed. Cells were trypsinized, centrifuged and cell lysate was prepared.

Fluorescence intensity of Rhodamine 123 in cell lysates was measured using Spectrofluorometer. We observed that the fluorescence intensity of Rhodamine 123 was higher in case of RDT-NPs treated U-87 MG cells as compared to BSA-NPs treated cells (Figure 4.22). This implies that the extent of endocytosis of RDT-NPs in U-87 MG cells was much higher than BSA-NPs. When cells pre-incubated with free RDT, the difference in the extent of endocytosis was not observed between BSA-NPs and RDT-NPs (Figure 4.22). This may be due to free RDT binding to a cell surface, HB-EGF. This does not allow RDT-NPs to binds and internalized.

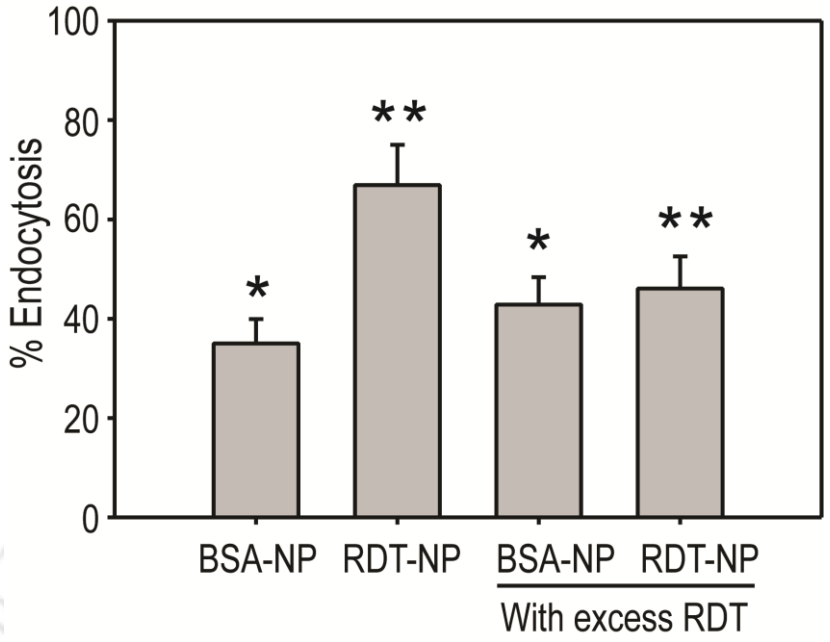

Figure 4.22: Competitive assay showing excess RDT reduces uptake of RDT-NPs. U-87 MG cells were treated with either BSA-coated or RDT-coated NPs in presence or absence of excess RDT, at 37 ˚C for 2 h. Cells were lysed and fluorescence intensity of Rhodamine 123 was measured by Spectrofluorometer to estimate the extent of endocytosis. One way ANOVA with pairwise comparison. **have significant difference ($p<0.01$); *do not have significant difference ($p>0.05$).

To understand the mechanism of internalization of RDT-NPs, different physical and chemical inhibitors of endocytosis were used. In general, low temperature reduces endocytosis (181). Chlorpromazine is an inhibitor of Clathrin-dependent receptor-mediated endocytosis (182) and Filipin inhibits Caveolae-dependent receptor-mediated endocytosis (183). The IC_{50} values of chlorpromazine and filipin for U 87-MG cells were determined by MTT assay. In 96- well plate, U-87 MG cells were treated with either chlorpromazine or filipin in different doses for 48 h in serum-free medium. The calculated IC_{50} values of chlorpromazine and filipin were 10 µM and 9.5 µM, respectively (Figure 4.23a, b).

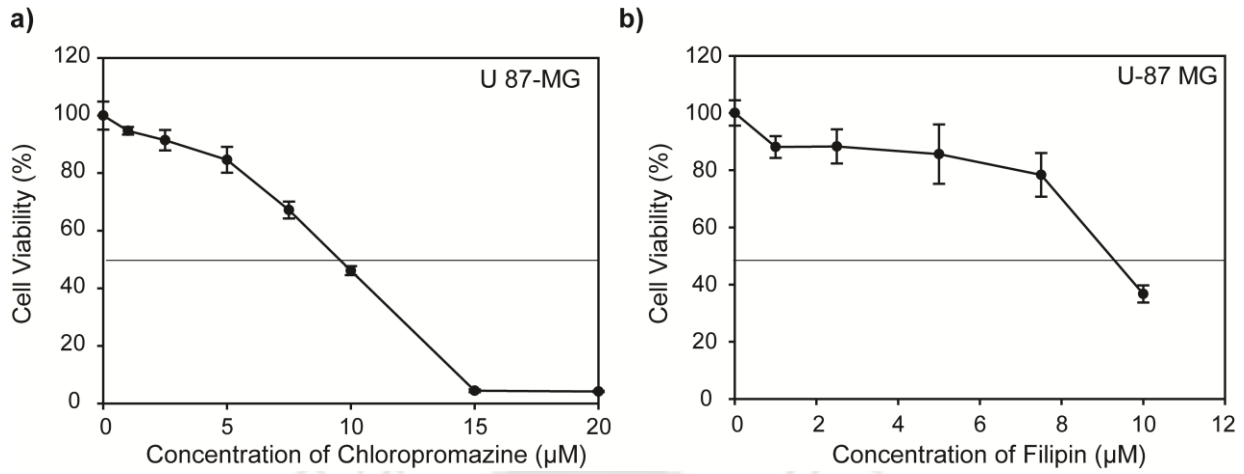

Figure 4.23: Cytotoxicity of endocytosis inhibitor. U-87 MG cells were treated with different concentrations of (a) Chlorpromazine and (b) Filipin for 48 h and cell viability was measured by MTT assay. The gray horizontal line represents 50% cell viability.

We have checked working of chlorpromazine as an inhibitor of Clathrin-mediated endocytosis. In our experimental system, it is known that cellular uptake of transferrin is by Clathrin-mediated endocytosis (184). We treated U 87-MG cells with Transferrin-FITC (0.1 µm and 0.25 µM) in presence or absence of chlorpromazine (5 µM). After 2 h of incubation, cells were lysed by sonication, centrifuged and cell lysate was prepared. The fluorescence intensity of transferrin-FITC was measured using Spectrofluorometer. We observed that uptake of transferrin-FITC was lowered in chlorpromazine treated cells (Figure 4.24). This result confirms that chlorpromazine at 5 µM inhibits Clathrin-mediated endocytosis in U 87-MG cells. We planned to perform a similar experiment for filipin but couldn't execute it due to non-availability of required reagent in time.

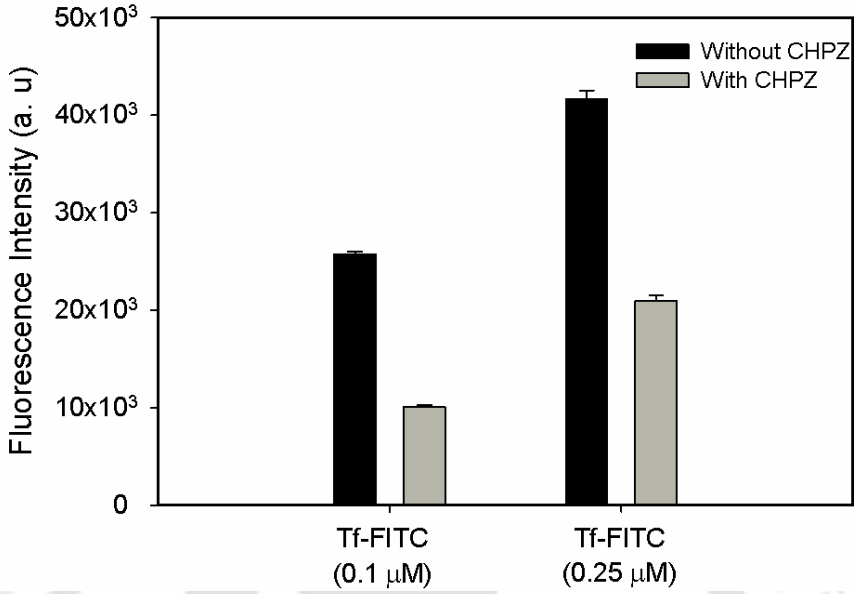

Figure 4.24: Chloropromzine (CHPZ) blocks uptake of Transferrin-FITC in U-87 MC cells. Transferin is known to be taken up by Clathrin-mediated endocytosis.

U-87 MG cells were treated with Rhodamine 123-loaded RDT-NPs and BSA-NPs at 37 °C and 4 °C. It was observed that the extent of cellular uptake is reduced by several folds for both BSA- and RDT-NPs at 4 °C (Figure 4.25).

We have treated U-87 MG cells, with RDT-NPs and BSA-NPs, in the presence of chlorpromazine and filipin. It has been reported that chlorpromazine inhibits receptor-mediated endocytosis of DT whereas filipin doesn't affect receptor-mediated endocytosis of DT (183). In our experiment, chlorpromazine inhibited cellular uptake of RDT-NPs (Figure 4.25). However, chlorpromazine did not affect uptake of BSA-NPs as it does not involve any receptor-mediated endocytosis. Additionally, filipin failed to reduce cellular uptake of RDT-NPs (Figure 4.25). These experiments confirmed that RDT-NPs were internalized by Clathrin-dependent, HB-EGF-mediated endocytosis.

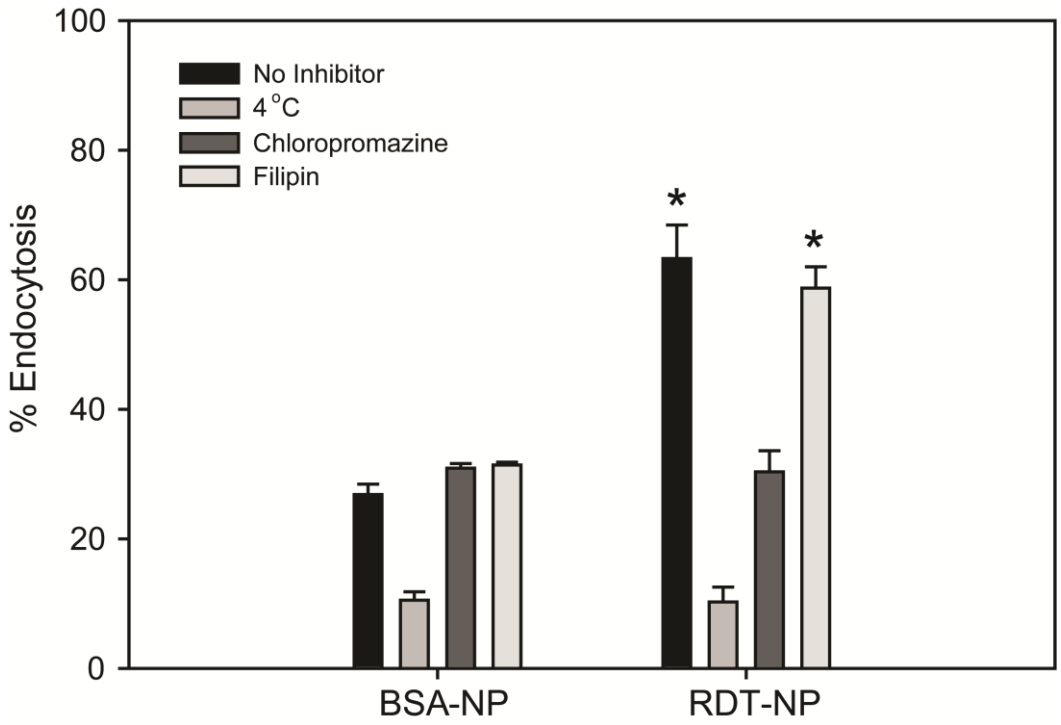

Figure 4.25: Effect of inhibition of endocytosis on uptake of RDT-NPs. U-87 MG cells treated with either BSA-coated or RDT-coated NPs in different conditions. Cells were washed, lysed and fluorescence intensity of Rhodamine 123 was measured to estimate the extent of endocytosis. One-way ANOVA with a pairwise comparison: *do not have a significant difference ($p > 0.05$) among these two.

4.1.6 Enhanced uptake of RDT-NPs increases potency of a drug

Irinotecan is a prodrug that gets hydrolyzed to generate SN-38 (185). SN-38 acts as a chemotherapeutic agent by inhibiting topoisomerase I, which results in cell death (186). This enzyme plays important role in DNA replication by cutting one strand of dsDNA and relaxes DNA molecules (187). Irinotecan (CPT-11) is FDA approved anti-cancer drug for the treatment of metastatic colorectal cancer and advanced pancreatic cancer (188, 189).

In this work, Irinotecan was loaded in RDT-coated NPs and delivered to U 87-MG cells *in vitro.* We have earlier showed that RDT-coated NPs have higher uptake in U 87-MG cells due to receptor-mediated endocytosis. We expected that such enhance uptake will also help to increase the cytotoxicity of Irinotecan when the drug is delivered using RDT-coated NPs.

During experiments, Irinotecan was assayed using UV-Vis spectrophotometer. For that, absorbance spectrum of Irinotecan was determined. The Irinotecan (10 µg/ml) was dissolved in 10 mM PBS (pH 7.4). Absorbance was recorded at wavelength 210 nm to 600 nm (Figure 4.26). The spectrum is similar to the spectra reported earlier (190, 191). In our experiments, Irinotecan was assayed at 255 nm and 370 nm.

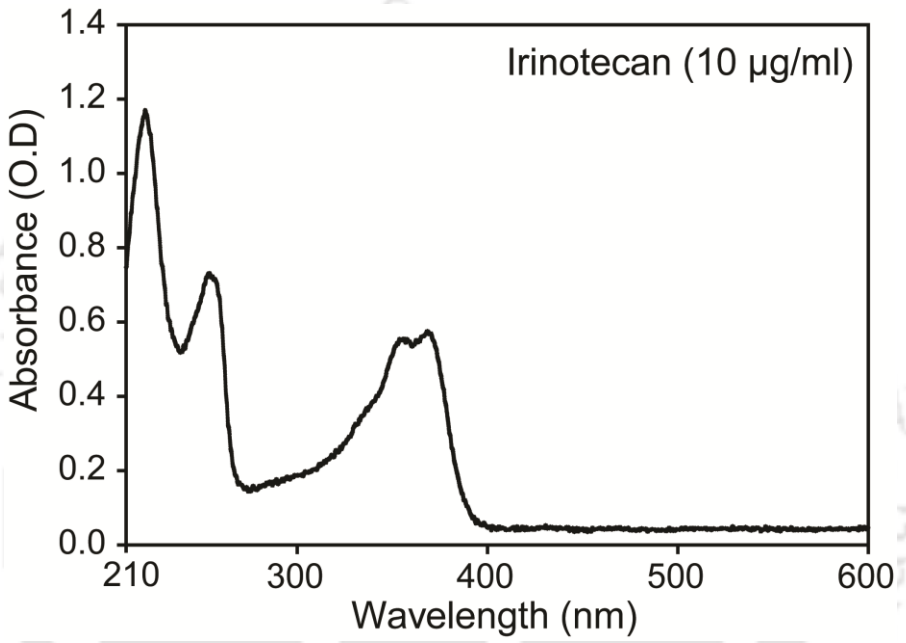

Figure 4.26: UV-Visible absorption spectrum of Irinotecan. The Irinotecan (10 µg/ml) was dissolved in 10 mM PBS (pH 7.4) and absorbance was recorded at wavelength 210 nm to 600 nm.

The poly(lactic-co-glycolic acid) is biodegradable and non-toxic. During synthesis of PLGA nanoparticles, we used toxic solvents chloroform to dissolve PLGA. If solvents are not removed properly, the PLGA NPs can be toxic to the cells. So, we performed cytotoxicity assay of BSA-coated and RDT-coated NPs. The effect of these nanoparticles on cell viability was measured by MTT assay. In 96 well plates, U-87 MG cells were treated with different concentration of BSA-coated NPs and RDT-coated NPs for 48 h in serum-free medium. We observed that RDT-NPs and BSA-NPs without drug do not have considerable cytotoxicity even at a higher dose 100 µg/ml (Figure 4.27).

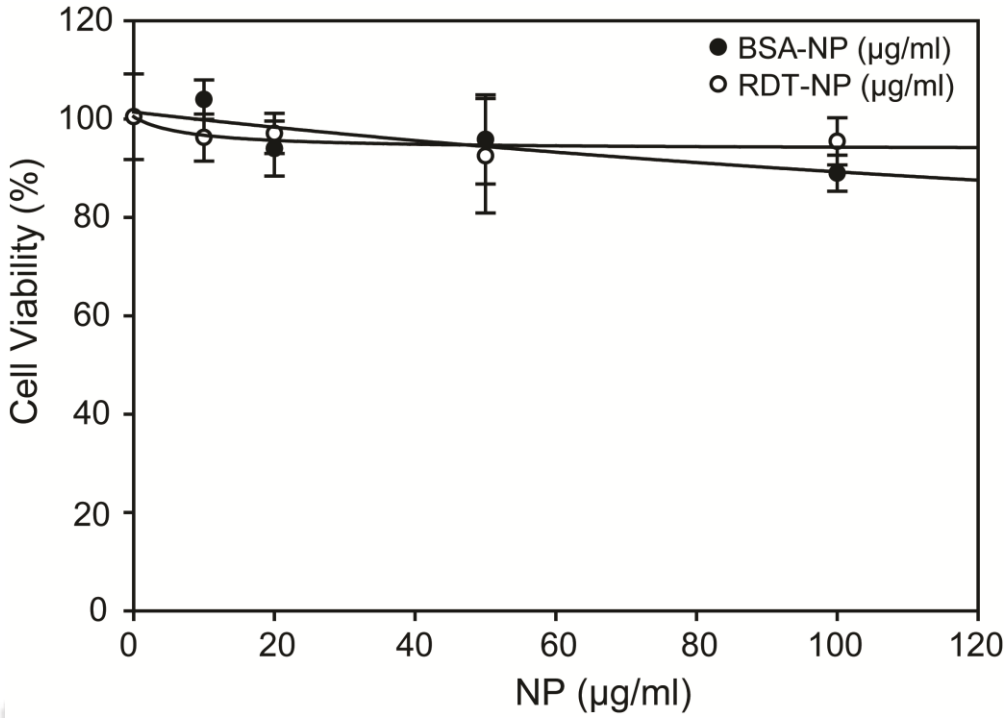

Figure 4.27: RDT-coated and BSA-coated NPs are non-toxic to U 87-MG cells. U-87 MG cells were treated with different concentrations of BSA- and RDT-coated NPs for 48 h and cell viability was measured by MTT assay. One-way ANOVA shows that there is no dose-dependent effect on the viability of cells for both types of NPs ($p > 0.01$).

The NPs were coated with either RDT or BSA. These protein coatings may affect *in vitro* release of drug from NPs. Therefore, we performed *in vitro* drug release assay. The releases of Irinotecan from Irinotecan-loaded NPs were measured using UV-Visible spectroscopy. The Irinotecan-loaded uncoated NPs, BSA-NPs, and RDT-NPs (2.5 mg) were dispersed in 1 ml PBS (pH 7.4) and incubated for different durations. The amount of Irinotecan released in solution was measured using UV spectrophotometer at absorbance 255 nm and 370 nm. A standard curve was made by measuring the absorbance of Irinotecan solution of different concentrations (Figure 4.28a, b). Percentage release of the drug, from NPs was calculated from the absorbance data using the standard curve (Figure 4.28c, d). It has been observed that protein coating does not affect in vitro release of the drug from NPs and most of the drug is released by 6 h.

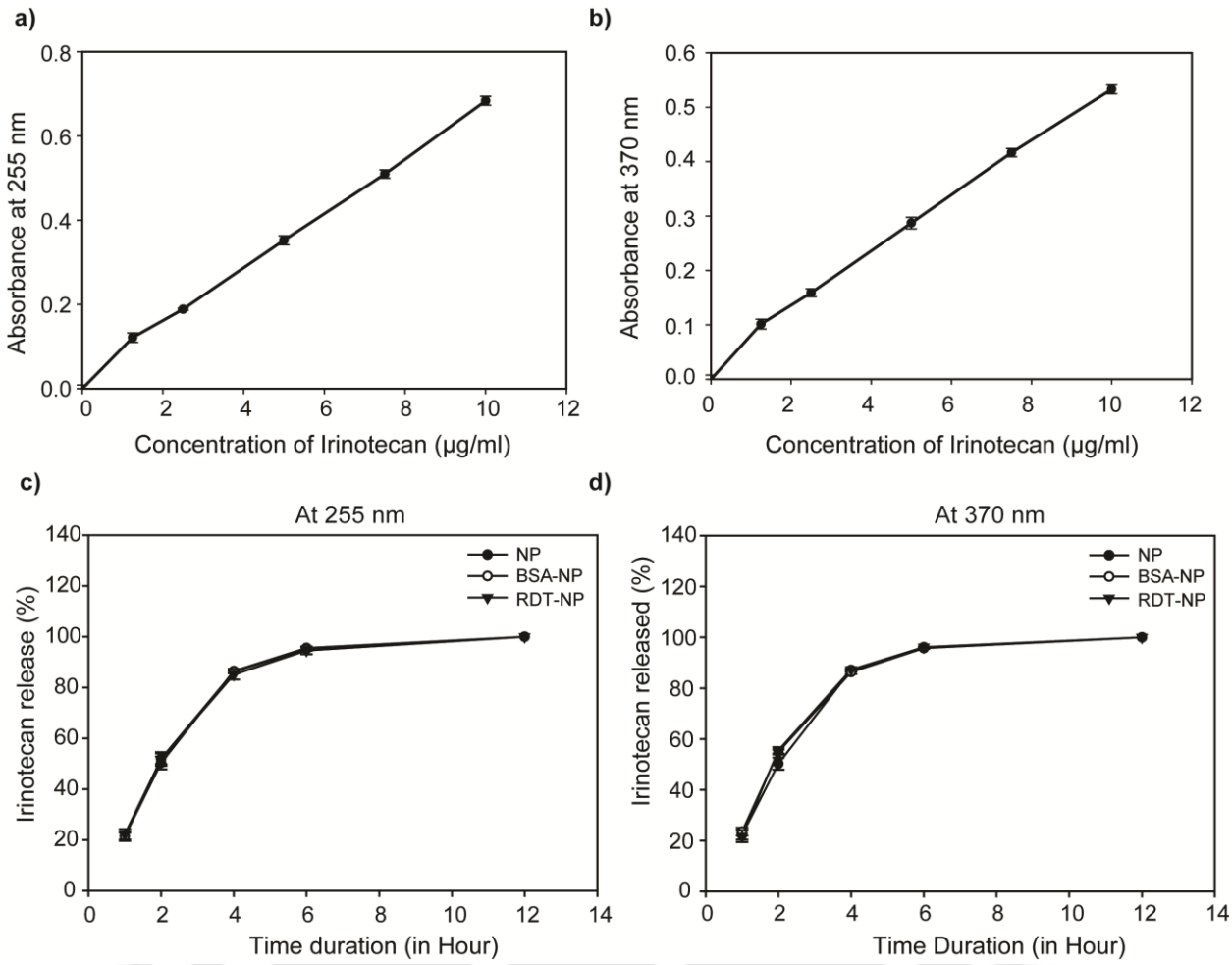

Figure 4.28: *In vitro* release of Irinotecan from coated and uncoated NPs. A standard curve shows the absorbance of Irinotecan solution at different concentrations a) 255 nm b) 370 nm. The concentration of Irinotecan in external medium (PBS) was measured both at (c) 255 nm and (d) 370 nm by UV-Visible absorption spectroscopy. The extent of drug release was calculated from that data.

Further, we studied the effect of enhanced uptake of Irinotecan through RDT-coated NPs on drug potency. We treated U 87-MG and RAW 264.7 cells, with Irinotecan-loaded RDT-NPs and Irinotecan loaded BSA-NPs for 48 h in serum-free media. These cells were also treated with free Irinotecan in solution. Cell viability was measured by MTT assay.

In U 87-MG cells, the IC_{50} of Irinotecan is 18.74 μM, but when delivered by RDT-coated NPs, the IC_{50} is 8.69 μM (Figure 4.29a). This means Irinotecan-loaded RDT-NPs is more cytotoxic to U-87 MG cells than free Irinotecan. However, BSA-coated NPs did not increase the cytotoxicity of the drug.

We observed that Irinotecan-loaded RDT-NPs and free Irinotecan in solution had a similar effect on RAW 264.7 cells (Figure 4.29b). Therefore, RDT-NPs do not change the effect of the drug in RAW 264.7 cells. Rather, at higher concentrations, irinotecan in solution has more effect than its nanoformulations. Such variation may arise due to slow release of the drug from NPs. We observed that Irinotecan has a similar effect on RAW 264.7 cells when delivered through BSA-NPs and RDT-NPs. Observations in Figure 4.29 confirm our postulate that delivery of Irinotecan using RDT-coated NPs would increase its potency in U 87-MG cells.

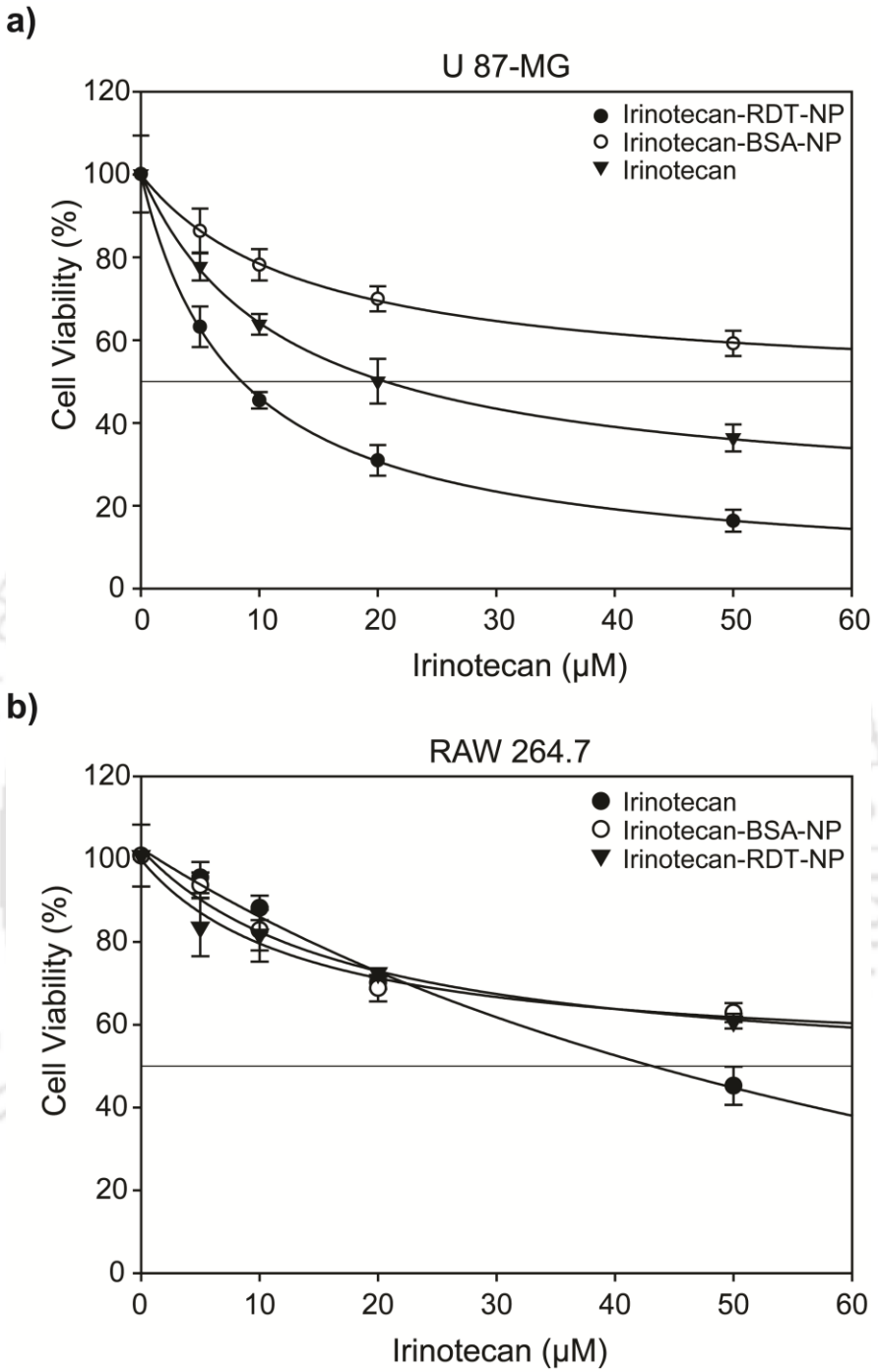

Figure 4.29: RDT-NP increases potency of irinotecan in U-87 MG cells. Effects of irinotecan in solution or loaded in RDT-NP and BSA-NP on viability of (a) U-87 MG and (b) RAW 264.7 cells. Cells were treated for 48 h in serum-free media and cell viability was measured by MTT assay. Data points were fitted to exponential decay equation to calculate IC_{50}. The gray horizontal line represents 50% cell viability.

Highlights of the work:

- RDT-coated NPs are synthesized of size less than 50 nm.
- Cellular uptake of RDT-NPs is higher than uncoated NPs in HB-EGF expressing cells.
- RDT-NPs are internalized through Clathrin-mediated endocytosis.
- RDT-NPs enhanced the potency of the drug in HB-EGF overexpressing cells.

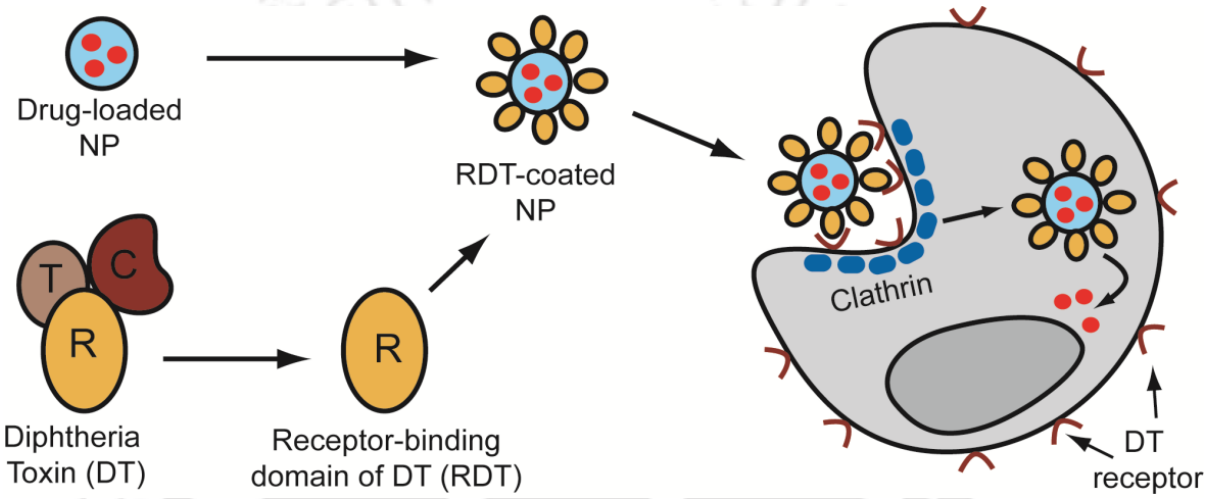

SECTION II:

Characterization of small peptide derived from RDT for receptor binding.

Design, Synthesis and Characterization of peptide

↓

Binding studies using peptides

↓

Cloning, Site directed mutagenesis
and expression of MBP tagged peptides

↓

Binding studies using MBP-peptides

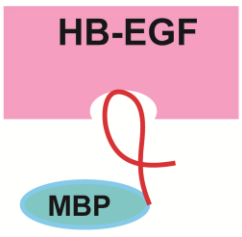

↓

Studies to check effect of MBP-tagged
peptides on function of HB-EGF

4.2.1 Design of peptides from Diphtheria toxin for binding to HB-EGF:

Diphtheria toxin binds to HB-EGF through its receptor binding domain. The crystal structure of HB-EGF-bound DT is available in PDB (ID: 1XDT). The receptor binding domain of DT has 155 amino acids with a flattened antiparallel β-barrel structure (5). Earlier, we have reported that RDT can bind to HB-EGF, independently of other two domains, with a similar binding affinity (89). In this work, we have attempted to design RDT-derived peptides that would bind to HB-EGF.

We explored the crystal structure of HB-EGF bound to DT to identify amino acid residues crucial for binding of DT to HB-EGF. We used Contact Map Analysis (CMA) server (http://ligin.weizmann.ac.il/cma/) for contact map analysis. We observed that a stretch of 26 amino acids from S505 to F530 of DT makes a large number of contacts with HB-EGF (Figure 4.30a). Residues from S505 to F530 of DT are part of the β-sheet on the binding-face of R-domain of DT and forms a β-hairpin (class 2:2, type I') as shown in Figure 4.30b. This β-hairpin structure binds at an extended groove on the binding face of HB-EGF (Figure 4.30c). Residues of this hairpin structure interact with HB-EGF through non-covalent bonding such as Van der Waals interactions, hydrogen bonds and salt-bridges (192).

Mutagenesis studies have earlier shown that several residues between S505 and F530 of DT are important for binding to HB-EGF. It has been reported that K516 and F530 play a critical role in receptor recognition (98). Additionally, mutations at these sites, K516A and F530A exhibit receptor-blocking activity. In the region between S505 and F530 of DT, four other residues (Tyr-514, Val-523, Asn-524, and Lys-526) are involved in receptor binding (98). Based on these information's, we synthesized a peptide corresponding to S505-F530 of DT. Two additional glycines were added at the terminal during synthesis. We named this peptide as DTP28.

Gillet et. al (97) have mutated several amino acids (Y380K, Q387E, L390T, A395T, F389Y, and G510A) in the R-domain of Diphtheria toxin and created a recombinant R-domain of DT (DTR8) that has higher binding affinity than CRM197. One of these mutations G510A is within the region S505-F530. We designed a peptide identical to DTP28 but with this G to A mutation (Figure 4.31). We hoped that this mutation may improve binding of the peptide to HB-EGF. We called this peptide DTP28A.

It has been reported that RDT is immunogenic and have several CD4+ T-cell epitopes (193, 194). One of those T-cell epitopes lies within selected region corresponding S505 to F530 of

DT. Therefore, DTP28 may elicit an immune response on repeated *in vivo* use. Gillet *et al.* have shown that a mutation T517E disrupts the T-cell epitope without affecting the affinity for HB-EGF (97). Based on this, we designed another peptide DTP28AE that has both T to E and G to A mutations at respective places (Figure 4.31).

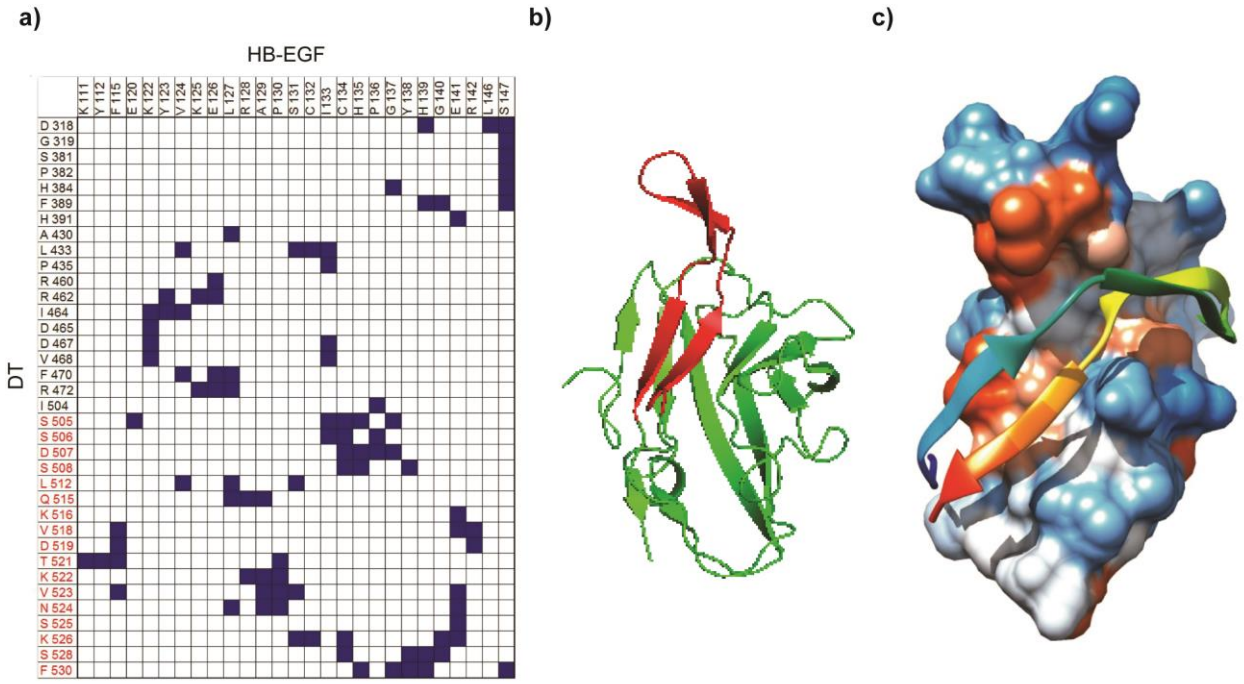

Figure 4.30: Design of peptides from Diphtheria toxin. a) Contact map of DT-HB-EGF complex based on the crystal structure, ID: 1XDT. Only those residues of R-domain that make contacts are shown. Residues from S505 to F530 are shown in red. b) Residues from S505 to F530 form a β-hairpin as shown in red c) Structure of the β-hairpin (S505 to F530) bound on HB-EGF as observed in 1XDT. The hairpin is shown by ribbon diagram and the surface represents HB-EGF. Color code for protein surface: blue = hydrophilic and orange-red = hydrophobic.

We have designed, another 28 amino acids long peptide that has three mutations: V511P, Q515G, and K526P. It is named as DTP28Neg (Figure 4.31). Two prolines were introduced in DTP28Neg to disturb the formation of β-hairpin structure. Glutamine at 515 is mutated to glycine, as this residue is known to be very crucial for binding of DT to HB-EGF (96, 97). The

DTP28Neg peptide is expected not to bind with HB-EGF and will serve as a negative control in an experiment.

Figure 4.31: Amino acid sequences of synthetic peptides. A glycine was added on both terminals during peptide synthesis in DTP28, DTP28A, DTP28AE, and DTP28Neg. Additional Glycine's are not shown here. Mutated residues are in red. Residue numbering of PDB ID: 1XDT is used.

Synthesis and Characterization of peptides:

DTP28, DTP28A, DTP28AE, and DTP28Neg peptides were synthesized by solid-phase synthesis.

The purity of all the peptides was checked by analytical HPLC. From retention time of HPLC chromatograms, it was concluded that the peptide DTP28A is low polar compare to others; whereas peptide DTP28AE and peptide DTP28Neg has comparable polarity, though theoretically peptide DTP28AE should be high polar in nature compare to others. The HPLC data is shown in Figure A1 (in Appendix).

Further, all the pure peptides were characterized by ESI-MS spectrometry. ESI-MS profile pictures of the peptides are shown in Figure A2 (in Appendix). The calculated and observed molecular weights of peptides are given in Table 4.1.

Additionally, all the pure peptides were also characterized by MALDI mass spectrometry. MALDI peaks of the peptides are shown in Figure A3 (in Appendix). The calculated and observed molecular weights of peptides are given in Table 4.2.

Table 4.1: ESI-MS spectrometry of the peptides

Peptide	M/z	Calculated	Observed
DTP28 ($C_{129}H_{210}N_{36}O_{42}$)	[M+2H]2+	1469.6318	1469.7802
	[M+3H]3+	980.0879	979.8572
	[M+4H]4+	735.3159	735.1407
	[M+5H]5+	588.4527	588.3120
DTP28A ($C_{130}H_{212}N_{36}O_{42}$)	[M+2H]2+	1476.6451	1476.3163
	[M+3H]3+	984.7634	984.5488
	[M+4H]4+	738.8225	738.6591
	[M+5H]5+	591.2580	591.1256
DTP28AE ($C_{131}H_{212}N_{36}O_{43}$)	[M+2H]2+	1490.6502	1490.3089
	[M+3H]3+	994.1001	993.8800
	[M+4H]4+	745.8251	745.6616
	[M+5H]5+	596.8600	596.9281
DTP28Neg ($C_{125}H_{198}N_{34}O_{41}$)	[M+2H]2+	1417.5564	1417.2328
	[M+3H]3+	945.3709	945.1569
	[M+4H]4+	709.2782	709.1163

Table 4.2: MALDI mass spectrometry of the peptides

Peptides	M/z	Calculated	Observed
DTP28 ($C_{129}H_{210}N_{36}O_{42}$)	[M+2H]+	2939.2637	2939.7560
DTP28A ($C_{130}H_{212}N_{36}O_{42}$)	[M+3H]+	2954.2903	2954.2890
DTP28AE ($C_{131}H_{212}N_{36}O_{43}$)	[M+2H]+	2981.3004	2981.0810
DTP28Neg ($C_{125}H_{198}N_{34}O_{41}$)	[M]+	2833.1128	2833.8160

Synthesis of peptides, HPLC and ESI-MS was performed by Mr. Tanmay Mondal at Department of chemistry, IIT Guwahati, under the supervision of Dr. Bhubaneswar Mandal, of Department of chemistry, IIT Guwahati.

The purity of these peptides was further checked by Tricine-SDS-PAGE. Tricine SDS-PAGE is commonly used to separate protein in the mass range 1-100 kDa. The purity of short peptides of molecular weight ~2.9 kDa was confirmed by Tricine SDS-PAGE as shown in Figure 4.32.

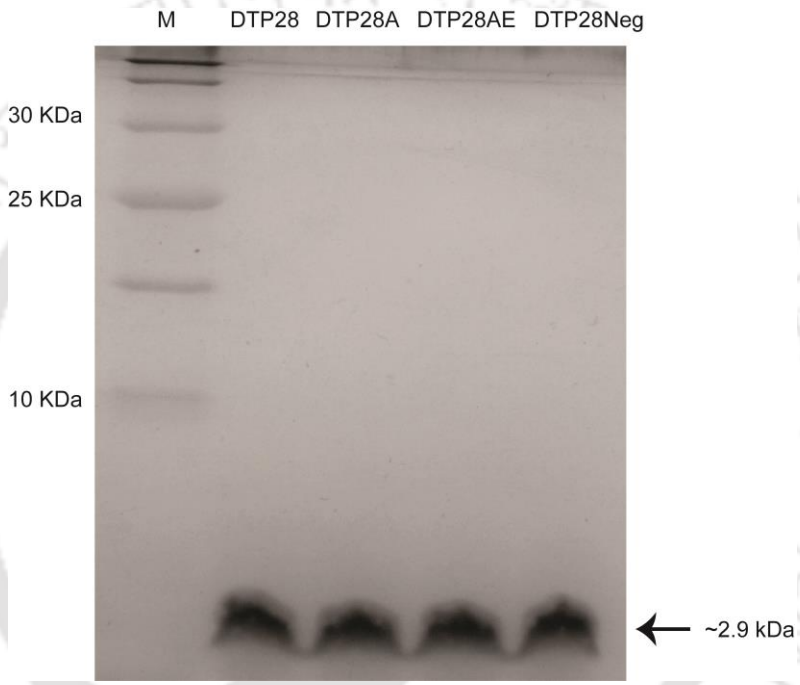

Figure 4.32: Purity of peptides checked by Tricine SDS-PAGE. The synthesized peptides DTP28, DTP28A, DTP28AE and DTP28Neg were separated in 16% acrylamide -6M Urea gel. The molecular weight of peptide is ~2.9 kDa. M: Protein molecular weight marker. The gel was visualized by silver staining.

We used Circular Dichroism (CD) to understand the probable secondary structure of these synthetic peptides. The β-hairpin structures of peptides usually shows a broad, negative CD band at ~218 nm and a positive band at ~200 nm. Whereas random coils show negative CD band near 202 nm (195, 196). All the four synthesized peptides showed a negative CD band at 200-202 nm and did not have any CD band with positive $\Delta\varepsilon$ (Figure 4.33).

CD spectra of some β-sheet rich proteins deviate from the usual CD spectrum for β-sheet and resemble that of unordered proteins with a negative band near 200 nm (197, 198). CD spectra of certain β-hairpin peptides also show a negative band near 200 nm (199, 200). Additionally, the CD spectrum of a peptide is an ensemble-average over different conformations in solution. Therefore, if only small fractions of DTP28, DTP28A, and DTP28AE fold in the expected β-hairpins, we would not be able to detect those by CD. Therefore, observations of our circular dichroism experiments alone cannot be used to reliably comment on the secondary structure of these peptides.

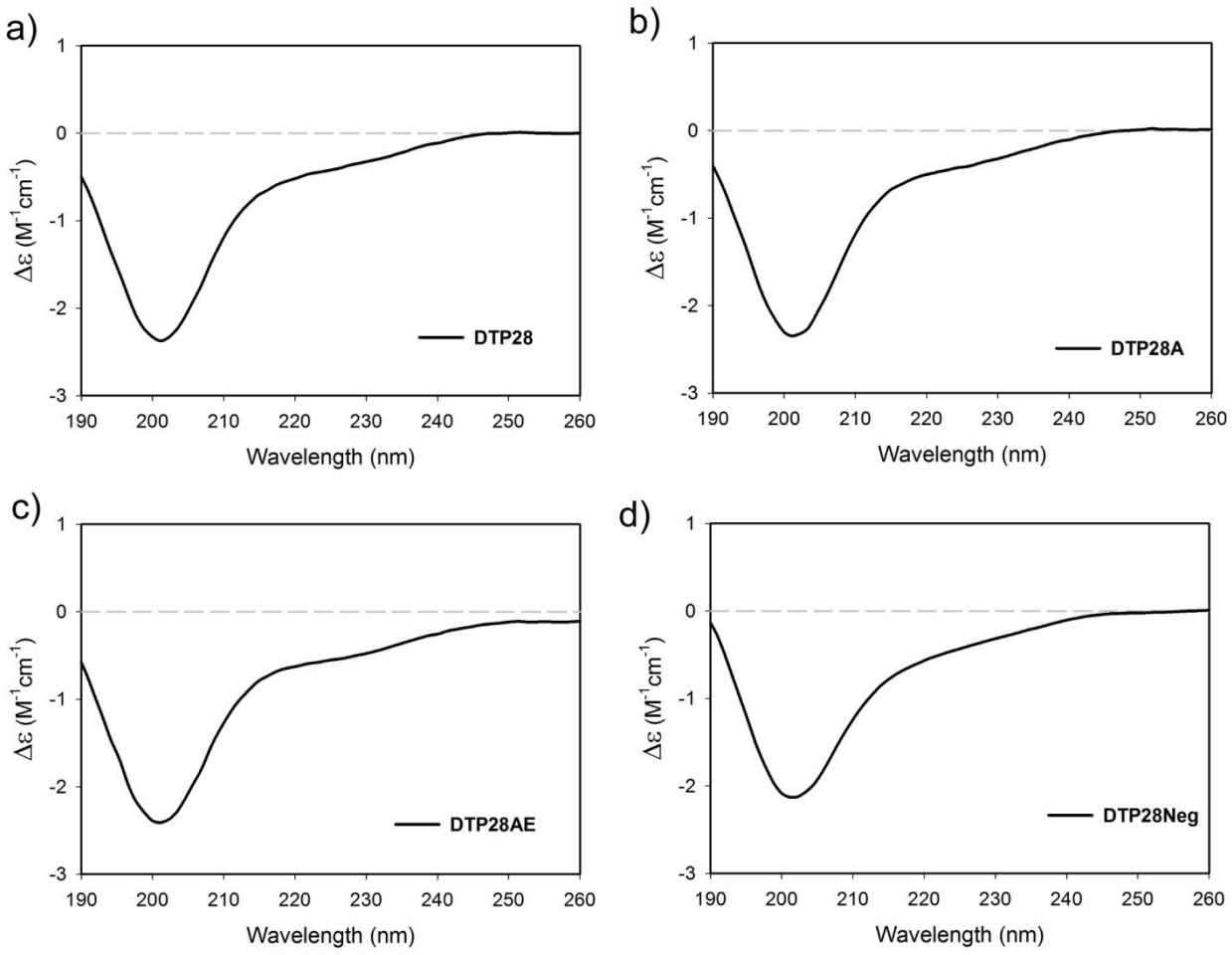

Figure 4.33: Structure prediction of peptides using Circular Dichroism. 15 µM peptides are dissolved in 1% ethanol and scan at a far-UV range. Secondary structures of (a) DTP28,(b) DTP28A, (c) DTP28AE and (d) DTP28Neg peptides.

Computational analysis of peptides:

We performed molecular docking and molecular dynamic simulations, to investigate whether these peptides have any possibility to bind HB-EGF.

The molecular docking of DT-derived peptides with HB-EGF receptor was performed using CABS-dock. The CABS-dock web server provides an interface to dock a peptide to protein (171). The structural information of the peptide and the binding site on receptor is not a necessity. It doesn't require pre-localization of binding sites. Therefore, it is performing blind docking. CABS-dock performs a simulation to search for the possible binding sites of the peptide on a receptor. Structure of R-domain was derived from the crystal structure 1XDT. This structure was used as one input for docking. The amino acid sequences of DTP28, DTP28A, DTP28AE, and DTP28Neg were used as another input for docking. CABS-dock produced 10 best results for docking for each peptide. These docked structures were further analyzed.

The best model for DTP28, DTP28A, DTP28AE are shown in Figure 4.34. In all these three cases, these peptides had folded in β-hairpin-like structures and had got docked in the correct binding groove (Figure 4.34). In almost half of the cases, these peptides folded in hairpin-like structures and were docked at the designated binding-grove on HB-EGF. However, DTP28Neg had not folded into β-hairpin conformation due to the presence of prolines. All the possible structure of DTP28Neg was in random conformation and failed to bind to the designated grove of HB-EGF (Figure 4.34d and e).

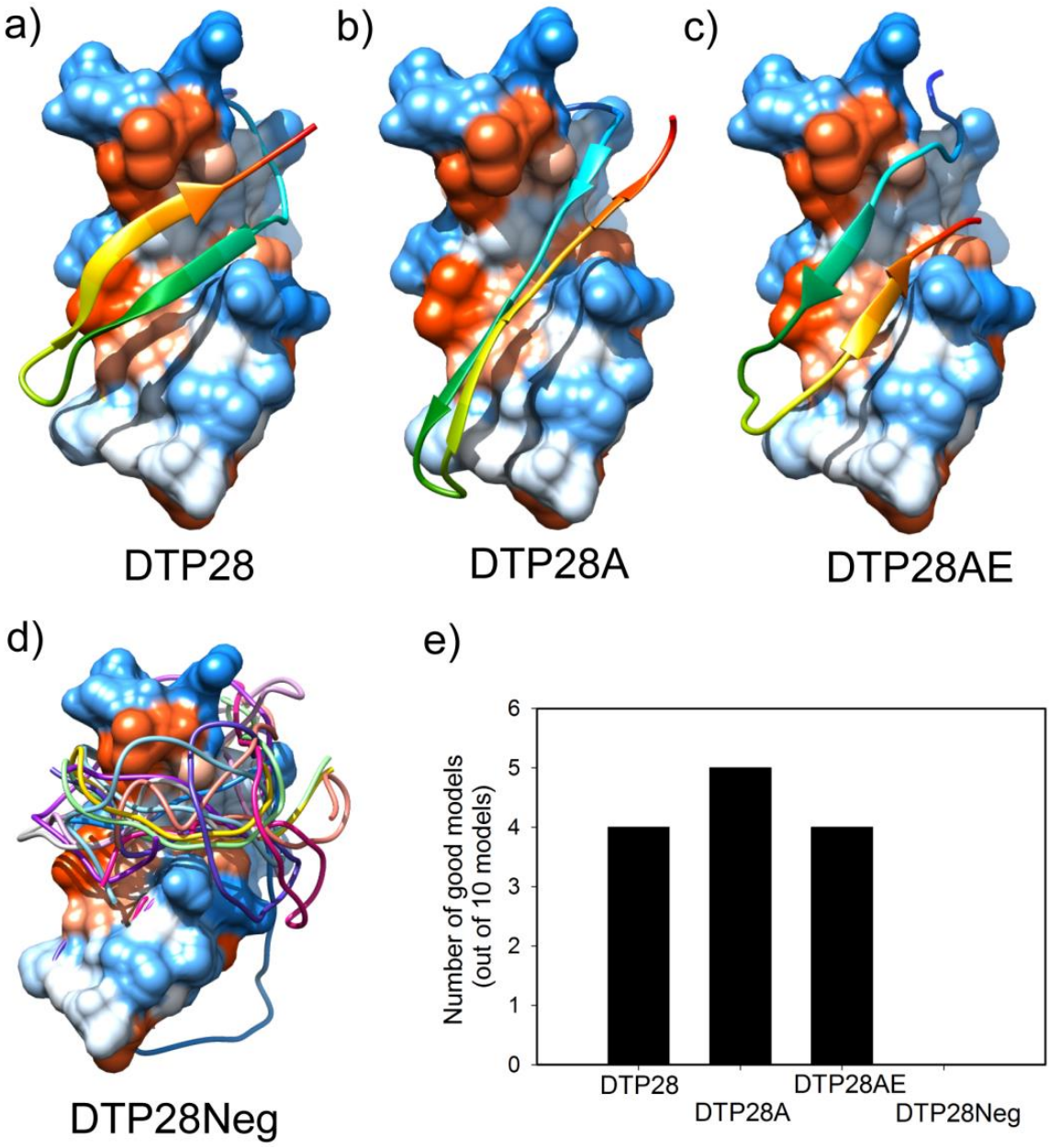

Figure 4.34: In silico docking of peptides to HB-EGF. CABS-dock was used to perform docking peptides on HB-EGF. The best models of (a) DTP28, (b) DTP28A, and (c) DTP28AE are shown. (d) Shows all the models selected by CABS-dock for DTP28Neg. (e) Shows the number of good models obtained for these peptides. Good models are those where peptides had folded in hairpin-like structures. It bound on a designated binding groove of HB-EGF. The peptides are shown as ribbons and the surface represents HB-EGF. Color code for protein surface: blue = hydrophilic and orange-red = hydrophobic.

The stability and dynamics of the β-hairpin of DTP28 were analyzed using molecular dynamic simulations (MDS). We have separately performed MDS for RDT and the β-hairpin region, S505 to F530, of RDT by Gromacs tool. We have compared dynamics of this β-hairpin of the whole protein, RDT and as a separate peptide. After completion of simulations, output data were analyzed to find root mean square deviation (RMSD), radius of gyration (Rg) and root mean square fluctuation (RMSF).

We used RMSD to measure deviations of backbone atoms from the position in the crystal structure 1XDT, during MDS. In a way, RMSD value is inversely related to the stability of the peptide. The RMSD values for the β-hairpin in both the structures are reasonably small and do not show any drastic fluctuations. The RMSD of backbone atoms of the β-hairpin in RDT varied around an average value of 0.19 nm (range: 0.11 to 0.28 nm). The average RMSD for the β-hairpin in DTP28 is 0.45 nm (range: 0.19 to 0.56 nm) (Figure 4.35a). The lower RMSD values for the β-hairpin in RDT in comparison to DTP28 are expected as other parts of the protein limits movement of the hairpin. Here, we conclude that the β-hairpin is stable as a part of the whole protein, as well as a separate peptide.

The radius of gyration (Rg) is defined as the root mean square distance of the collection of atoms from their common center of gravity. It is a measure of compactness of structure. Low fluctuation in Rg indicates stably folded protein/peptide. It was observed that the radius of gyration of the β-hairpin is small in RDT as well in DTP28 (Figure 4.35b).

Furthermore, fluctuation of each residue of the β-hairpin was calculated. The antiparallel β-strands show little fluctuation and the loop region shows higher fluctuation than the β-strands (Figure 4.35c). This is expected as the β-strands are stabilized by hydrogen bonds and have less mobility than the loop region. The peptide showed high RMSF at the N-terminal end of that region does not have any defined secondary structure and is waving out.

The relative movements of different parts of the β-hairpin can be easily identified in Figure 4.35d, where multiple structures, sampled at various time points, are overlapped. It clearly shows that the most of the fluctuations are at the terminal regions of the β-hairpin, while the β-strands show lower fluctuations and hold their relative positions. The images were produced from program UCSF Chimera. All these studies indicate that once folded in the expected β-hairpin structure, DTP28 may stably retain that structure.

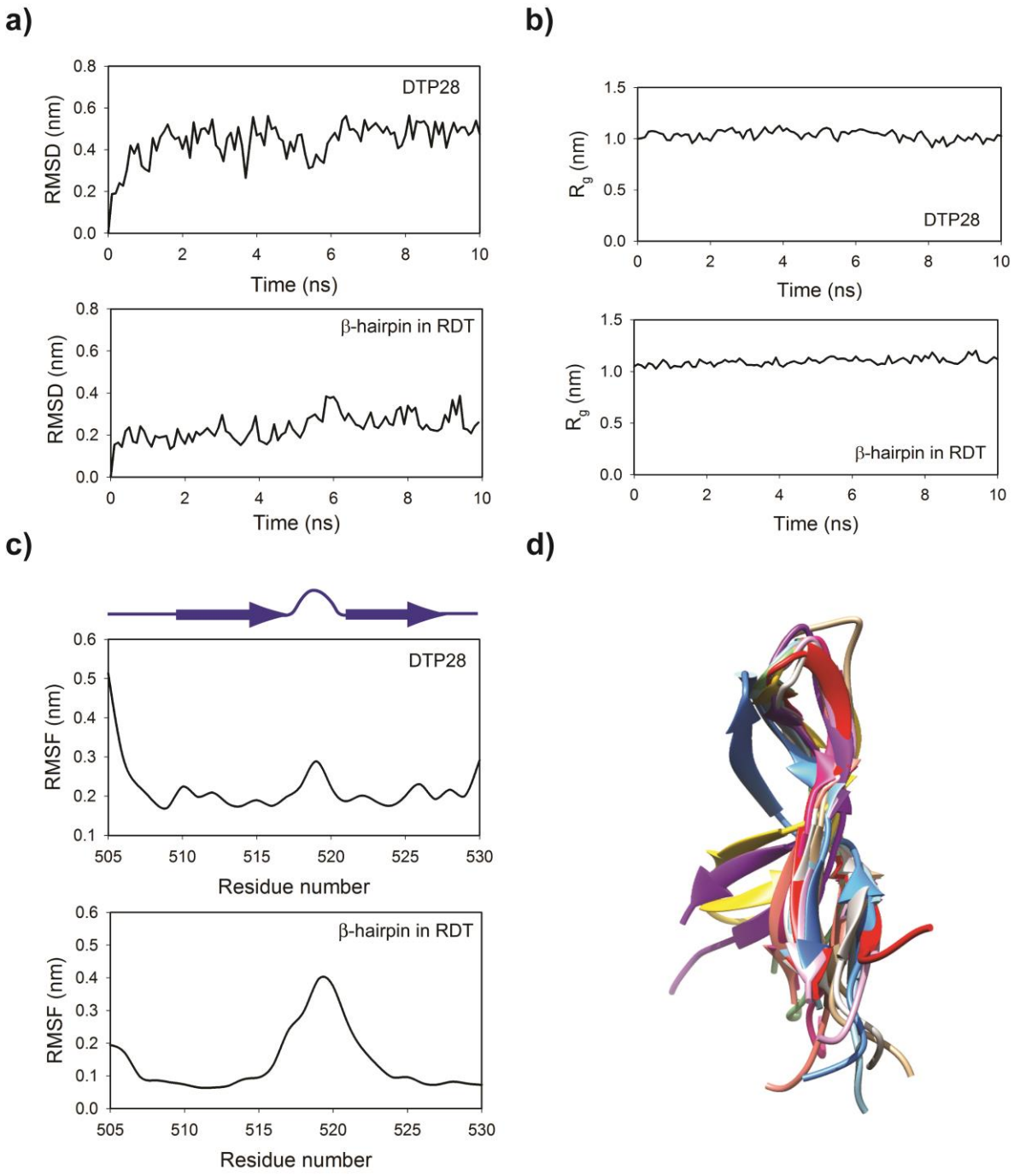

Figure 4.35: Stability of the β-hairpin. Results of molecular dynamic simulation were analyzed to calculate a) RMSD, b) Radius of gyration and c) RMSF for the β-hairpin (S505 – F530) as an independent peptide and as a part of RDT. d) Shows the overlap of different structures of the β-hairpin, when considered as a peptide, at time points where RMSD is high. The Red color ribbon represents the structure of β-hairpin in the X-ray crystallographic structure 1XDT. The images were produced from program UCSF Chimera.

Computational studies showed DTP28 is stable and can be used for experimental analysis. In this study, we have not checked the stability of mutated peptides. We checked binding of synthetic peptides to recombinant HB-EGF using solid phase ELISA.

4.2.2 Binding of peptides with HB-EGF

The binding of DTP28, DTP28A, and DTP28E to HB-EGF was measured by solid phase ELISA. The peptides were coated on microplate in different doses (0-2 µg/ml). After blocking, the recombinant human HB-EGF (200 ng/well) was added and incubated. Subsequently, bound HB-EGF was detected using anti-HB-EGF antibody followed by anti-mouse-HRP conjugated secondary antibody. ELISA was developed using OPD and absorbance measured at 492 nm. We have observed that DTP28, DTP28A and DTP28AE bind to recombinant HB-EGF in a dose dependent manner (Figure 4.36a). However, the negative control peptide DTP28Neg failed to bind with HB-EGF (Figure 4.36b).

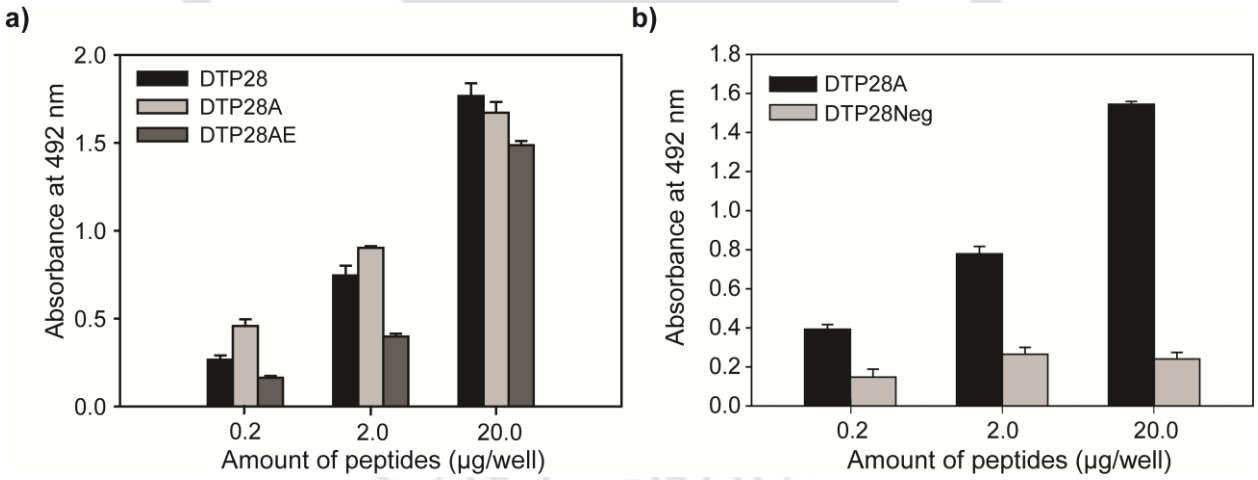

Figure 4.36: Solid phase ELISA to show that DT-derived peptides bind to HB-EGF. (a) The different amount of peptides, (a) DTP28, DTP28A, DTP28AE, and (b) DTP28Neg were coated on plate. Recombinant human HB-EGF was added and bound HB-EGF was detected using Anti-HB-EGF antibody and followed by anti-mouse-HRP conjugated secondary antibody. Each bar represents mean of data from three different wells.

A similar experiment was performed in which fixed amount of peptides (10 µg/well) were coated and varying the amount of HB-EGF (0-200 ng) was added. It was found that HB-EGF binds to the DTP28, DTP28A and DTP28E peptides in a dose-dependent manner (Figure 4.37).

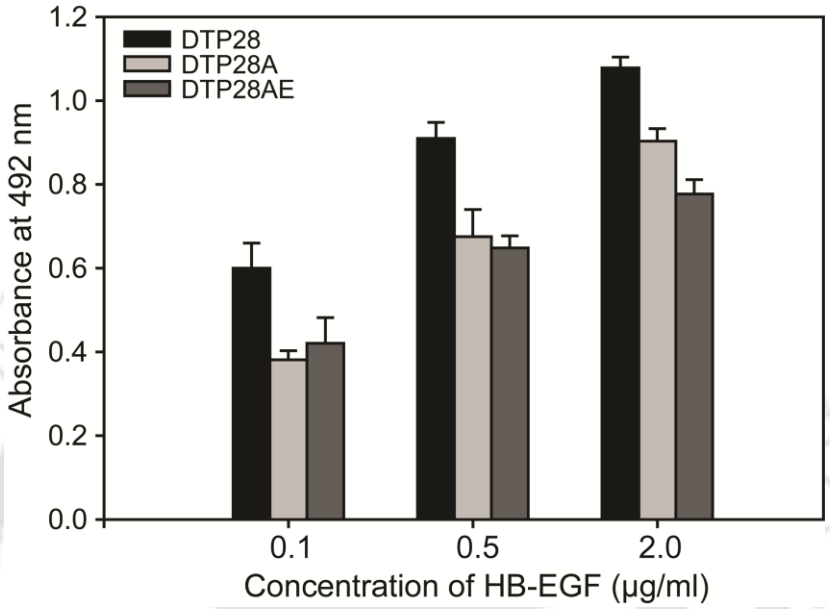

Figure 4.37: Solid phase ELISA to show that peptide binds to HB-EGF. The fixed concentration (10 µg/well) of peptides, DTP28, DTP28A, and DTP28AE were coated on plate. Recombinant human HB-EGF was added in varying concentration from 0-200 ng/well. Bound HB-EGF was detected using Anti-HB-EGF antibody and followed by anti-mouse-HRP conjugated secondary antibody. Each bar represents mean of data from three different wells.

Earlier, it has been reported that RDT binds to HB-EGF with high affinity (89). In a competitive ELISA, peptides DTP28, DTP28A, and DTP28AE were allowed to compete with RDT for binding to HB-EGF. The result shows RDT inhibits binding of these peptides to HB-EGF and extent of such inhibition increases with the concentration of RDT (Figure 4.38). This proves that these three synthetic peptides bind to the same site on HB-EGF where RDT binds.

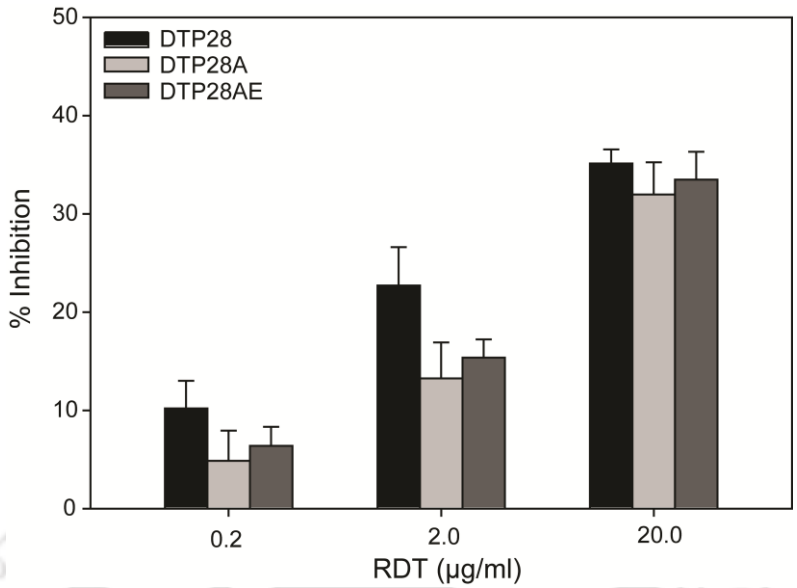

Figure 4.38: Competitive ELISA showing RDT reduces binding of peptides to HB-EGF. The peptides were coated on a microplate in a fixed concentration (2 µg/well). Recombinant human HB-EGF (200 ng/well) was added along with increasing amount of RDT (0-20 µg/ml). Bound HB-EGF was detected using anti-HB-EGF antibody and followed by anti-mouse-HRP conjugated secondary antibody. % Inhibition of binding was calculated from this ELISA data.

Further, we have studied the binding of these peptides to HB-EGF when fused with a large protein. For that, we have fused designed peptide to Maltose-binding Protein (MBP) and expressed those as recombinant MBP-tagged peptides in *E. coli.*

4.2.3 Cloning, site-directed mutagenesis, and expression of MBP tagged peptide

CRM197 and RDT have been earlier used for delivery of drug or nanoparticles in HB-EGF expressing cells (201). DT has also been used for cellular deliver proteins and peptides fused to it at its N-terminal (202, 203). Instead of whole protein, a peptide that binds to a cell surface molecule can be used for homing a cargo to the cell. Here, we investigated whether designed peptides would retain binding to HB-EGF when fused to a large protein.

Low molecular weight peptides are not suitable for experiments like SPR based affinity measurement. Peptides tagged with large molecular weight protein can help in determining

binding affinity using SPR. The designed peptides, DTP28, DTP28A, DTP28AE, and DTP28Neg were fused with Maltose Binding Protein (MBP) and expressed as MBP-tagged recombinant proteins in *E. coli.* MBP has high molecular weight (~42 kDa) and it facilitates soluble expression of peptides/proteins tagged to it in E. coli (204).

The sequence encoding the DTP28 peptide was cloned in frame with MBP to express the MBP-DTP28 protein.

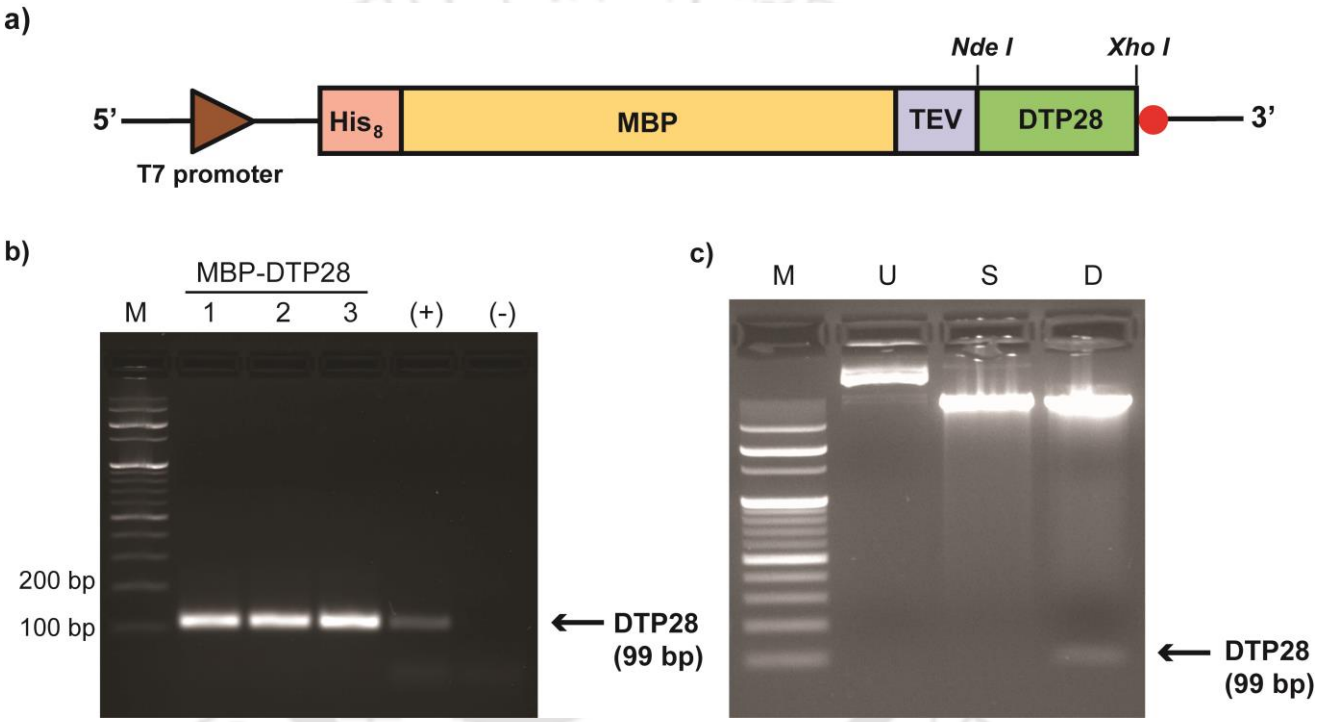

Figure 4.39: Cloning of DTP28 in MBP vector. (a) Design of the construct of MBP-DTP28. The gene for DTP28 (99 bp) is cloned into *Nde I* - *Xho I* site of the expression vector. His_8: Histidine tag and TEV protease cleavage site. (b) Three different clones were selected for colony PCR to check successful cloning of DTP28 in MBP vector. All three selected clones showed PCR amplification of DTP28. The pET-22b RDT plasmid is used as positive (+) control and water as negative (-) control (c) Double restriction digestion by *Nde* I and *Xho* I of the recombinant plasmid of DTP28 to confirm the presence of insert (DTP28). M: DNA ladder, U: undigested plasmid, S: single digested with *Nde I*, D: double digested with *Nde I* & *Xho I*.

The pET-22b-RDT recombinant plasmid was used as a template to amplify DTP28 gene insert using PCR. The details of PCR primers and annealing temperature are given in Table A7 (in Appendix). The MBP vector and insert were digested with *Nde I* and *Xho I* and ligated with Quick DNA ligase. The design of the recombinant construct is shown in Figure 4.37a. The recombinant construct was transformed in competent *E. coli* BL21 (DE3) using standard heat shock method. Recombinant clones were confirmed by colony PCR and double digestion (Figure 4.39b, c). Subsequently, the sequence of a positive recombinant clone was confirmed using DNA sequencing (Figure 4.44). It has been found that DTP28 is in right frame with TEV sequence and His-MBP tag at N-terminal. DTP28 cloned in frame with His-MBP has a molecular weight ~45 kDa. The annotated sequence with color code is shown in Figure 4.40.

a)

GAGAATCTTTATTTTCAGGGCGCCCATATGGGCTCATCGGATTCCATAGGCG
TTCTTGGGTACCAGAAAACAGTAGATCACACCAAGGTTAATTCTAAGCTATC
GCTATTTGGCTGACTCGAG

b)

E N L Y F Q G A H M G S S D S I G V L G Y Q K T V D H T K V N S K L S F G

Figure 4.40: Annotation of the partial sequence of recombinant MBP-tagged DTP28. (a) DNA sequence. Purple: TEV site, Green: *Nde* I site & *Xho* I site, Blue: sequence of DTP28, Red: stop codon. (b) Amino acid sequence of the same. Same color coding used.

The recombinant construct of MBP-DTP28 was transformed in *Escherichia coli* BL21 (DE3) by standard chemical transformation. The protein was expressed by induction with 0.4 mM IPTG for 4 h at 37˚ C. The whole cell lysate was prepared and separated by SDS-PAGE. The MBP-DTP28 protein has an approx. molecular weight of ~45 kDa as shown in Figure 4.41a. The recombinant His-MBP tagged DTP28 was purified by affinity chromatography, using nickel column (His-Trap column). MBP-DTP28 was eluted with 250 mM Imidazole. The MBP-DTP28 protein was analyzed by SDS-PAGE as shown in Figure 4.41b. Later, residual imidazole was removed by dialysis against PBS (pH 7.4).

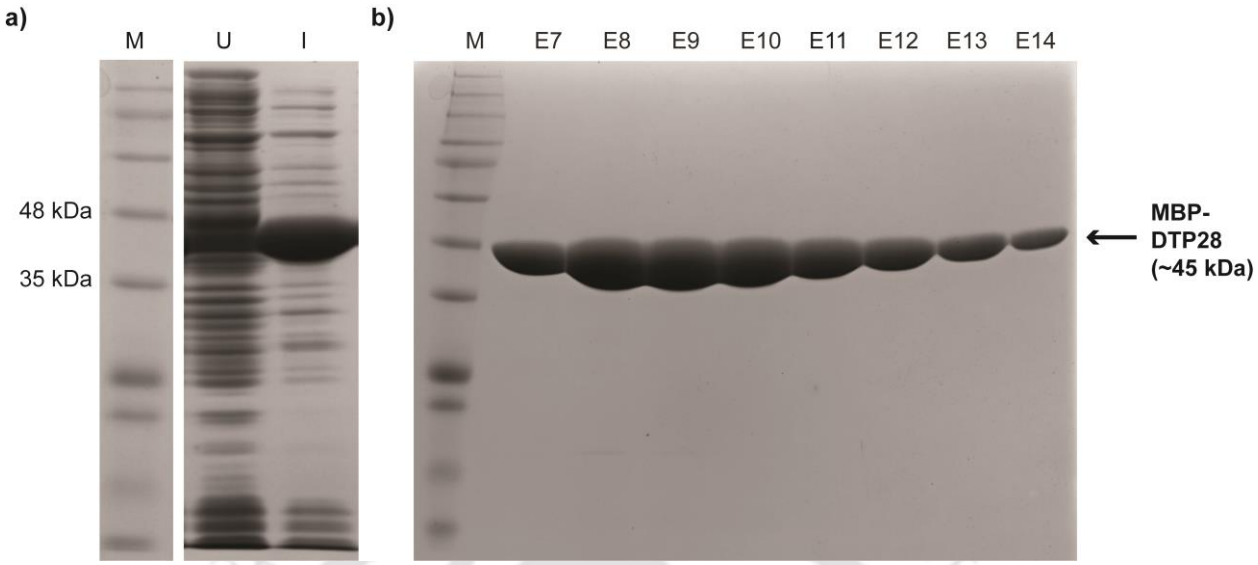

Figure 4.41: Expression and purification of recombinant MBP-tagged DTP28. (a) The recombinant construct of MBP-DTP28 was transformed in *E. coli* BL21 (DE3) and protein was expressed by induction with 0.4 mM IPTG for 4 hours at 37 ˚C. The whole cell lysate was prepared and separated by SDS-PAGE. M: protein molecular weight marker, U: whole cell lysate of untransformed *E.coli* BL21 (DE3), I: whole cell lysate of induced *E. coli* BL21 (DE3) cells. (b) Recombinant proteins were purified from the whole cell lysate using His-Trap FF affinity column. SDS-PAGE showing purified protein in elution fraction E7 to E14. Expression of MBP-DTP28 protein shows molecular weight ~45 kDa.

The recombinant construct of MBP tagged DTP28A, DTP28AE and DTP28Neg were created using PCR based site-directed mutagenesis (Q5 site-directed mutagenesis kit, NEB). The first mutant, MBP-DTP28A was created by mutating MBP-DTP28. G510A mutation was introduced as in DTP28 peptide. Another mutant, MBP-DTP28AE was created by mutating MBP-DTP28A. MBP-DTP28AE has two mutations, G510A and T517E as in DTP28AE peptide. MBP-DTP28Neg was created by mutating MBP-DTP28. DTP28Neg peptide has three mutations: V511P, Q515G, and K526P. The DNA sequences of MBP-tagged peptides with mutated color codes are given in Figure 4.42.

MBP-DTP28: 5‘- GGC . . . . . ATA GGC GTT ..... CAG AAA ACA GTA ..... TCT AAG CTA ..... GGC-3’

MBP-DTP28A: 5‘- GGC . . . . . ATA GCC GTT ..... CAG AAA ACA GTA ..... TCT AAG CTA .....GGC-3’

MBP-DTP28AE: 5‘- GGC . . . . . ATA GCC GTT ..... CAG AAA GAA GTA ..... TCT AAG CTA .....GGC-3’

MBP-DTP28Neg: 5‘- GGC . . . . . ATA GGC CCT ..... GGC AAA ACA GTA ..... TCTCCG CTA .....GGC-3’

Figure 4.42: DNA sequence of MBP-tagged peptides. The first mutant, MBP-DTP28A was created with G510A. The second mutant, MBP-DTP28AE was created with G510A and T517E. Another mutant, MBP-DTP28Neg was created with V511P, Q515G and K526P. Only the DNA sequences of the relevant regions are shown. Mutated bases are shown in Red color.

The substitution mutations were introduced by designing a mismatch in the center of the mutagenic primer. Primers were designed with 5’ ends annealing back to back. The details of PCR primers and annealing temperature are given in Table A7 in the Appendix. The recombinant MBP-DTP28 construct was used as a template for amplifying MBP-DTP28A. MBP-DTP28A construct was used as a template for amplifying MBP-DTP28AE. The amplification of plasmid construct is shown in Figure 4.43.

The amplified linear plasmid construct was treated with KLD mix for 15 min at room temperature. KLD mix contains kinase, ligase, and *Dpn I* enzymes which helps in efficient phosphorylation, intermolecular ligation/circularization and template removal in a single step. The KLD reaction mix is transformed in chemically competent *E. coli* BL21 (DE3). Subsequently, plasmids were isolated from recombinant clones of MBP-DTP28A and MBP-DTP28AE.

MBP-DTP28Neg was created in two steps. In the first step, two mutations V511P, Q515G were introduced using MBP-DTP28 construct as a template. After treatment of KLD mix, plasmid was isolated. Then, this plasmid was used as a template to introduce another mutation K526P in MBP-DTP28Neg. The details of PCR primers and annealing temperature are given in Table A7 in the Appendix. The PCR product is treated with KLD mix and transformed in chemically competent *E. coli* BL21 (DE3). Subsequently, plasmids were isolated from recombinant clones of MBP-DTP28Neg.

The mutated sequence of recombinant clones was confirmed using DNA sequencing. The T7 reverse primer was used during sequencing. The primer sequence is given in table A7 in the Appendix. The mutated sequence with color code is shown in Figure 4.42. Chromatograms of DNA sequencing are shown in Figure 4.44.

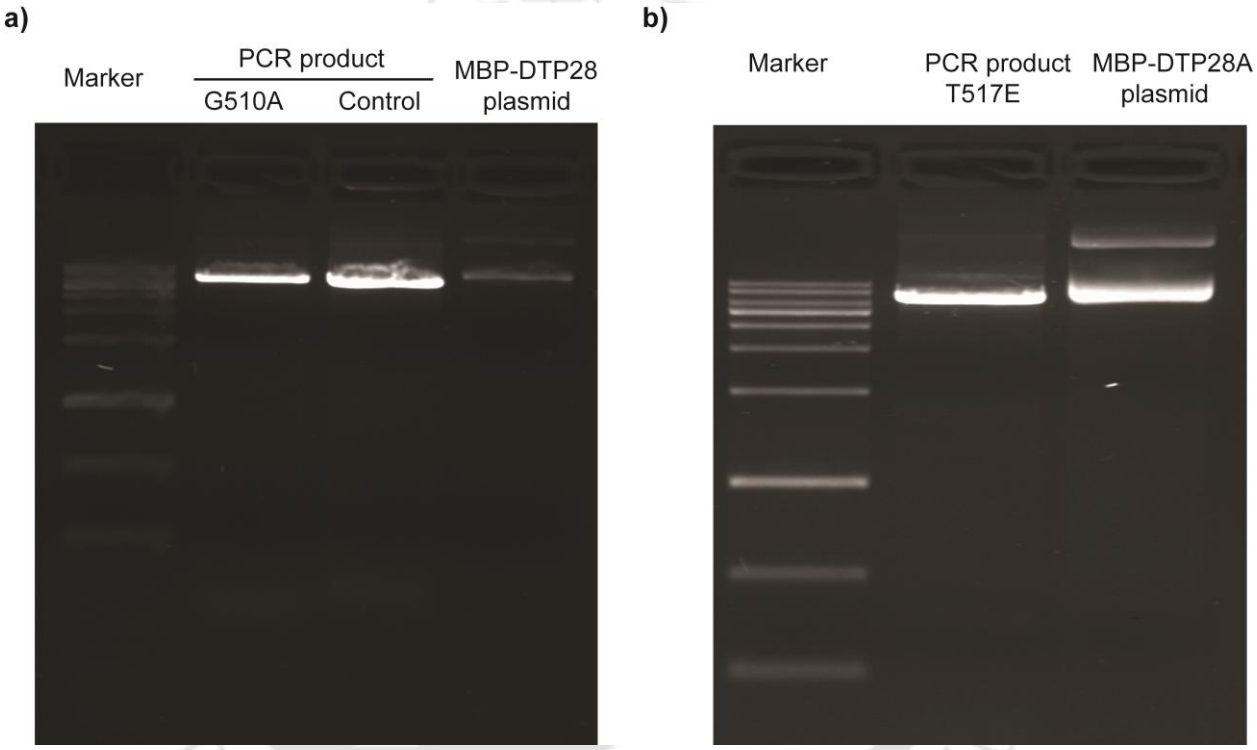

Figure 4.43: PCR-based site-directed mutagenesis. (a) PCR product of MBP-DTP28A with G510A mutation. MBP-DTP28 was used as template (b) PCR product of MBP-DTP28AE with G510A and T517E mutations. MBPDTP28A was used as template.

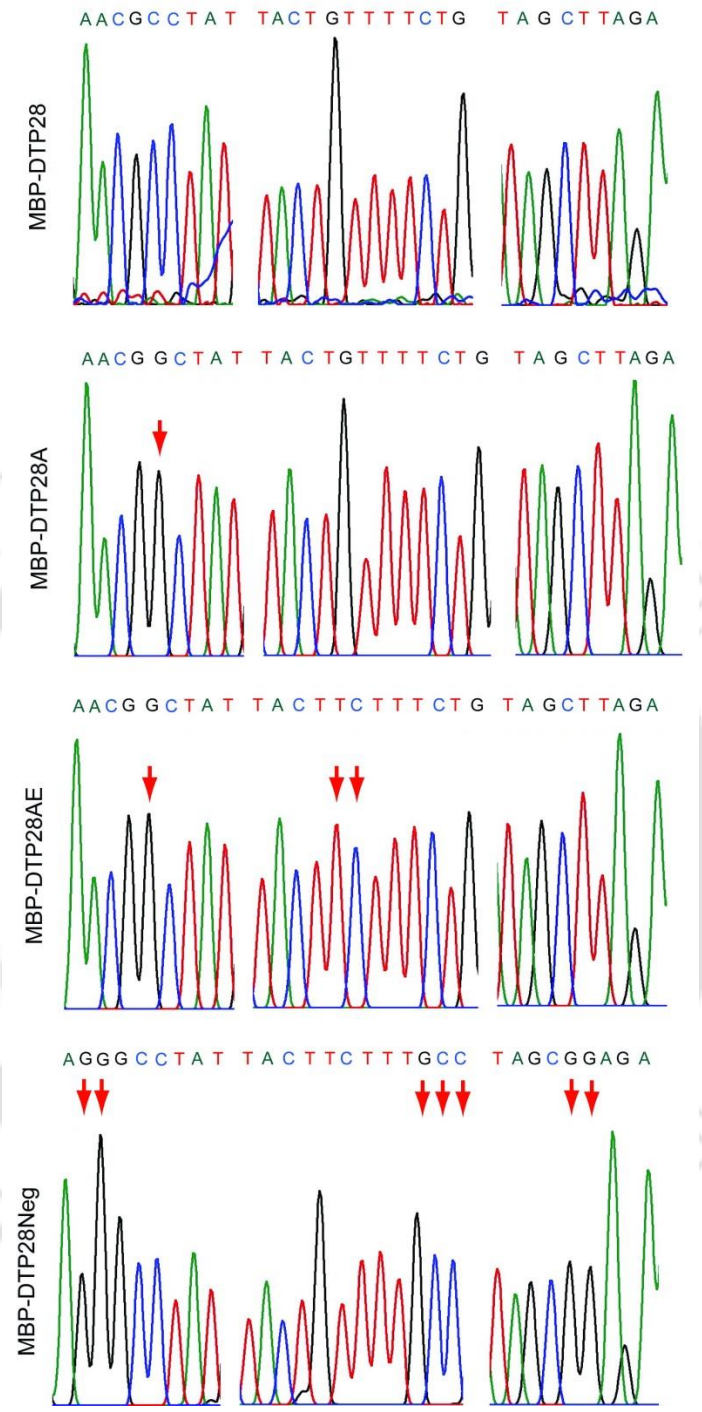

Figure 4.44: Clone confirmation of MBP-DTP28 and its mutants by sequencing. Chromatograms of DNA sequencing form clones to confirm mutations. Mutated bases are marked by an arrow. Note that sequencing was performed from the reverse direction. Therefore, the chromatogram represents reverse complement of the original sequences. Only the relevant sections of the chromatograms are shown here.

The recombinant constructs of MBP-DTP28A, MBP-DTP28AE, and MBP-DTP28Neg were transformed in *Escherichia coli* BL21 (DE3) by standard chemical transformation. The proteins were expressed by induction with 0.4 mM IPTG for 4 h at 37˚ C. The whole cell lysate was prepared. The recombinant His-MBP tagged DTP28A, DTP28AE and DTP28Neg were purified by affinity chromatography, using Nickel column (His-Trap column). Proteins were eluted with 250 mM Imidazole. Later, residual imidazole was removed by dialysis against PBS (pH 7.4). The purified MBP-DTP28, MBP-DTP28A, MBP-DTP28AE and MBP-DTP28Neg proteins were analyzed by SDS-PAGE (Figure 4.45). The expected molecular weight is ~45 kDa.

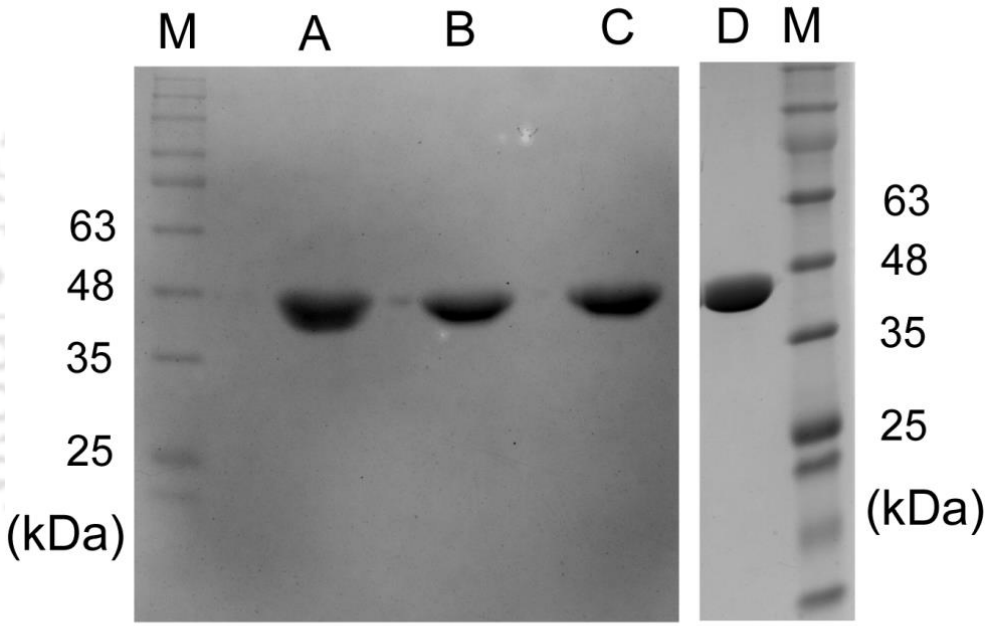

Figure 4.45: Purified mutated MBP-peptides. The MBP-tagged peptides were expressed by induction with IPTG and purified using His-trap FF affinity column. M: protein marker, A: MBP-DTP28, B: MBP-DTP28A, C: MBP-DTP28AE, D: MBP-DTP28Neg. Proteins were resolved by SDS-PAGE and expected molecular weight is ~45 kDa.

4.2.4 Binding of MBP-DTP28, MBP-DTP28A and MBP-DTP28AE to HB-EGF

Binding of MBP-DTP28, MBP-DTP28A, MBP-DTP28AE, and MBP-DTP28Neg proteins to HB-EGF was analyzed by solid-phase ELISA. Different amount of MBP-tagged peptides were coated on microplate (0-2 µg/ml). After blocking, the recombinant human HB-EGF (200 ng/well) was added. Subsequently, bound HB-EGF was detected using anti-HB-EGF antibody followed by anti-mouse HRP-conjugated secondary antibody. ELISA was developed using OPD and absorbance was measured at 492 nm. We have observed that MBP-DTP28, MBP-DTP28A, and MBP-DTP28AE bind to recombinant HB-EGF in a dose-dependent manner as shown in Figure 4.46a. However, MBP-DTP28Neg didn't bind to HB-EGF (Figure 4.46b).

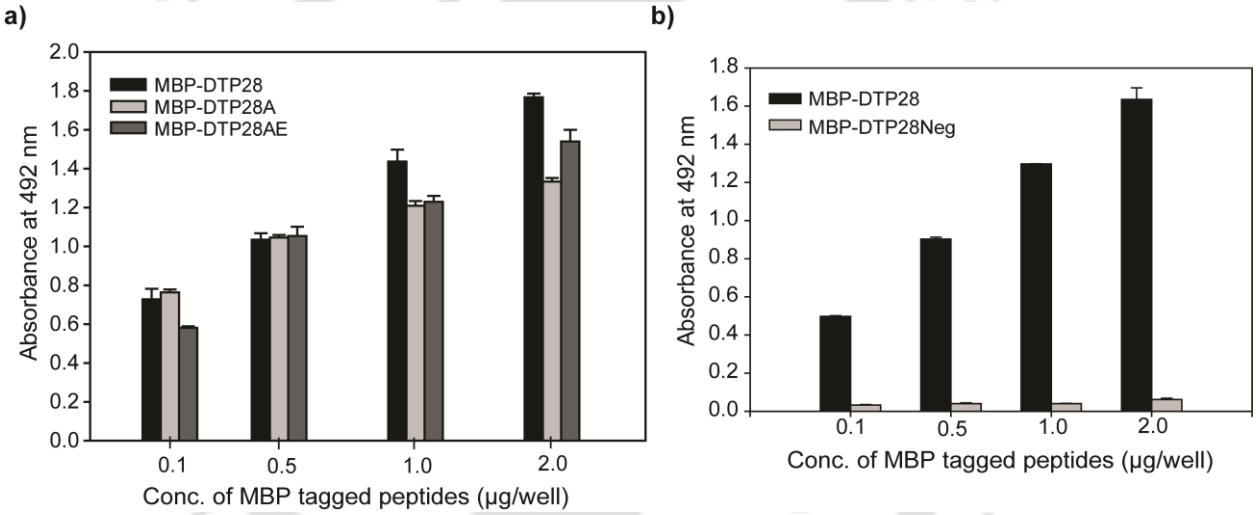

Figure 4.46: Binding of MBP tagged peptides to HB-EGF using solid phase ELISA. Different amount of MBP-peptides were coated on plate. Recombinant human HB-EGF was added and detected using anti-HB-EGF antibody and followed by anti-mouse HRP conjugated secondary antibody. a) Shows binding of MBP-DTP28, MBPDTP28A and MBP-DTP28AE to HB-EGF. b) Shows binding of MBP-DTP28 and MBP-DTP28Neg to HB-EGF. Each bar represents mean of data from three different wells.

Furthermore, data from SPR-based Biacore biosensor was used to measure binding affinities of these MBP-tagged peptides using Biacore X100 (GE Healthcare). The recombinant human HB-EGF was covalently immobilized on CM5 chip. Analyte such as MBP-DTP28, MBP-DTP28A, MBP-DTP28AE and only MBP were injected with varying concentration of 0 µM to 1 µM at 25 ˚C. The data recorded for 3 min of association and 10 min of dissociation. All three recombinant proteins showed dose-dependent binding to HB-EGF (Figure 4.47a, b, c). However, Recombinant MBP did not bind to with HB-EGF (Figure 4.47d). The data of SPR analysis were fitted to a 1:1 binding model using BIAevaluation Software (version 2.0) to estimate binding affinities. The Dissociation constants for MBP-DTP28, MBP-DTP28A, and MBP-DTP28AE are 4.85×10^{-8} M, 1.29×10^{-7} M and 2.78×10^{-7} M respectively. It has been earlier shown that dissociation constant for recombinant RDT and DT are 7×10^{-8} and 4×10^{-8}, respectively (89). Therefore, these MBP-tagged peptides have a reasonably good binding affinity for HB-EGF.

Considering that, these peptides represent only a short stretch of RDT, observed affinities in the range of 10^{-7} to 10^{-8} M is remarkable. These observations show that though the receptor-binding domain of DT is of 155 amino acids, this short stretch of 26 amino acids is an independent functional segment for binding of DT to HB-EGF.

The binding affinities of MBP-DTP28A and MBP-DTP28AE are similar to that of MBP-DTP28. So, we can conclude that G to A mutation at 510 is not crucial for binding to HB-EGF. The higher affinity observed by Gillet *et al.* may be due to the cumulative effect of six mutations introduced in the protein (97). We have also observed that T to E mutation at 517, introduced to disrupt the T-cell epitope, does not have a considerable effect on the affinity for HB-EGF.

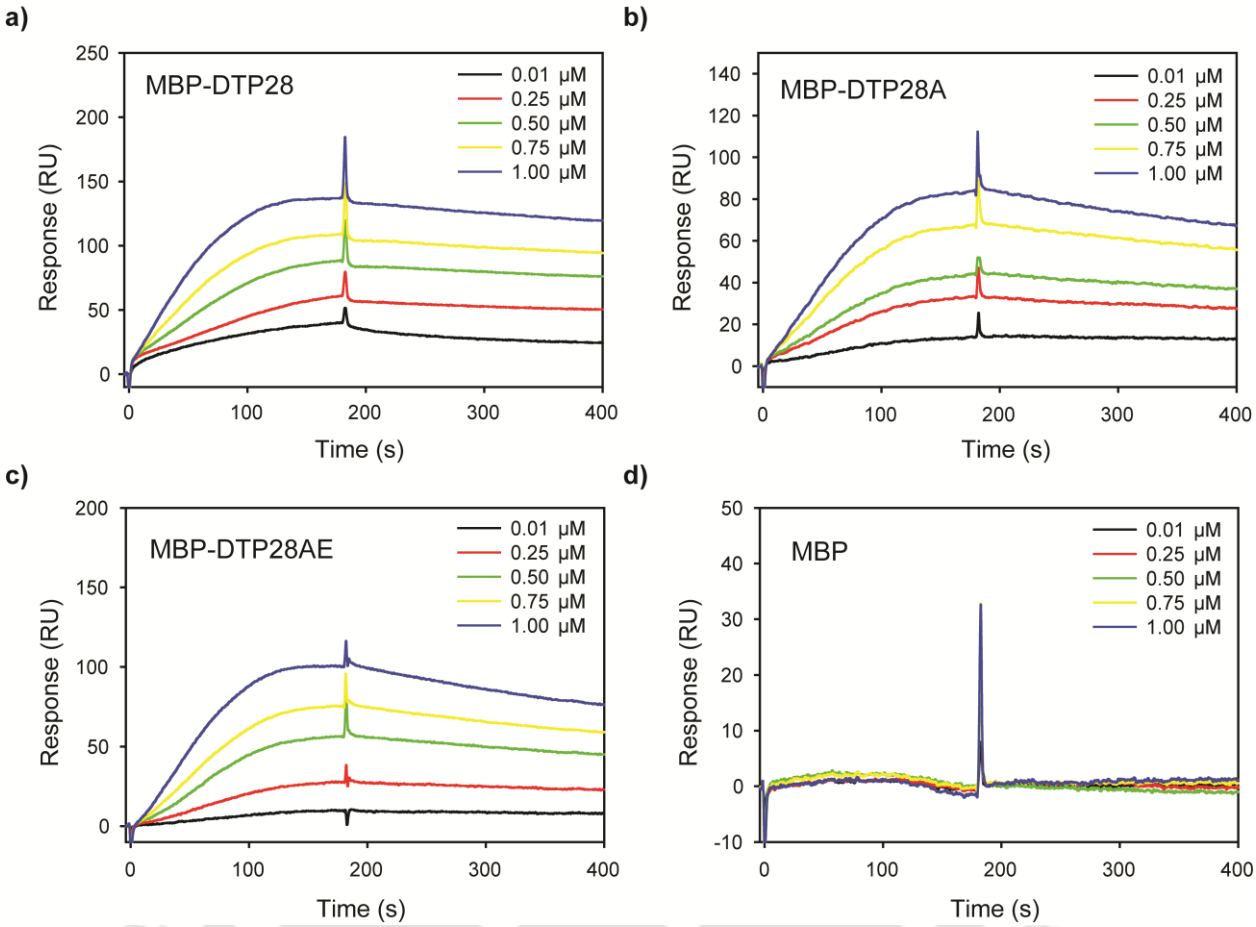

Figure 4.47: Binding affinities of MBP-tagged peptides to HB-EGF were measured using SPR-based Biacore X100 (GE Healthcare). The recombinant human HB-EGF was immobilized on CM5 chip. Binding was measured using multi-cycle kinetics, with five different concentrations (0.01 µM to 1 µM) of MBP-tagged peptides. (a) Sensogram for MBP-DTP28 (b) Sensogram for MBP-DTP28A (c) Sensogram for MBP-DTP28AE (d) Sensogram for MBP showing no binding to HB-EGF. Dissociation constants were estimated by fitting the data to a 1:1 binding model using BIAevaluation Software (version 2.0).

4.2.5 MBP-peptides inhibit MAPK signaling induced by HB-EGF

The soluble HB-EGF binds to ErbB1 and ErbB4 and activates MAPK pathways. This leads to cell proliferation and survival (205). It is well known that DT, RDT and CRM197 bind to the EGF-like domain of HB-EGF and blocks HB-EGF signaling (6, 89, 96). Here, we have tested the ability of MBP-tagged peptides to block or sequester soluble HB-EGF.

Western blot experiment was performed to check inhibition of HB-EGF signaling by MBP-peptides. Activation of EGFR by HB-EGF induces phosphorylation of Erk1/2. We have treated MDA-MB-468 cells with HB-EGF (0.5 nM), either alone or along with RDT (20 nM) or MBP-DTP28 (20 nM) or MBP (20 nM). HB-EGF induced phosphorylation of Erk1/2 (Lane-2, Figure 4.48a). Presence of MBP did not inhibit such phosphorylation (Lane-5, Figure 4.48a). But, RDT and MBP-DTP28 reduced HB-EGF induced phosphorylation of Erk1/2 in these cells (Lane 3 and 4 in Figure 4.48a).

A similar experiment was performed using mutant proteins, MBP-DP28A and MBP-DTP28AE. We treated MDA-MB-468 cells by HB-EGF (0.5 nM) alone or along with MBP-DTP28A (20 nM) or MBP-DTP28AE (20 nM). As observed in Figure 4.48b, these two mutated MBP-tagged peptides also inhibit HB-EGF induced phosphorylation of Erk1/2. These experiments showed that these MBP-tagged peptides can modulate mitogenic signaling of HB-EGF.

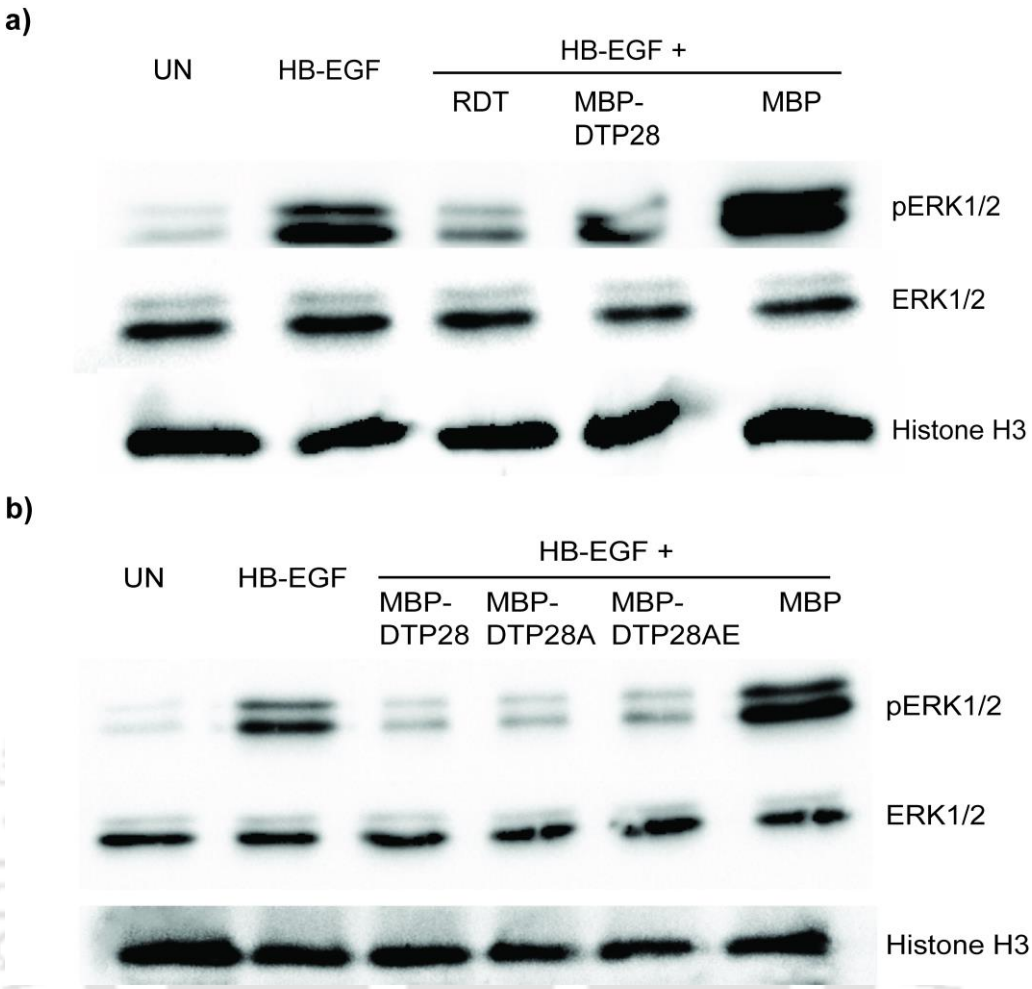

Figure 4.48: MBP-peptides inhibit HB-EGF mediated MAPK pathway. Western blots to detect phosphorylation of pERK1/2 in MDA-MB-468 cells. a) Cells were treated with HB-EGF alone or along with RDT/MBP/MBP-DTP28. b) Cells were treated with HB-EGF alone or along with MBP-DTP28/MBP-DTP28A/MBP-DTP28AE/MBP. RDT and MBP serve as positive and negative controls, respectively. Histone H3 was used as loading control.

Further, we have checked if MBP-tagged DTP28 and its mutants can inhibit HB-EGF induced increase in cell viability. The cell viability was measured using MTT assay. MDA-MB-468 cells were treated with different samples for 48 h in serum-free medium. Cells treated with only HB-EGF (1 nM) showed an increase in viable cells. However, no such increase in viability was observed, when cells were treated with HB-EGF (1 nM) along with MBP-tagged peptides (20 nM) (Figure 4.49). However, MBP (20 nM) did not affect the HB-EGF induced increase in cell

viability (Figure 4.49). This shows that MBP-tagged peptides, MBP-DTP28, MBP-DP28A, and MBP-DTP28AE can modulate mitogenic effect of HB-EGF.

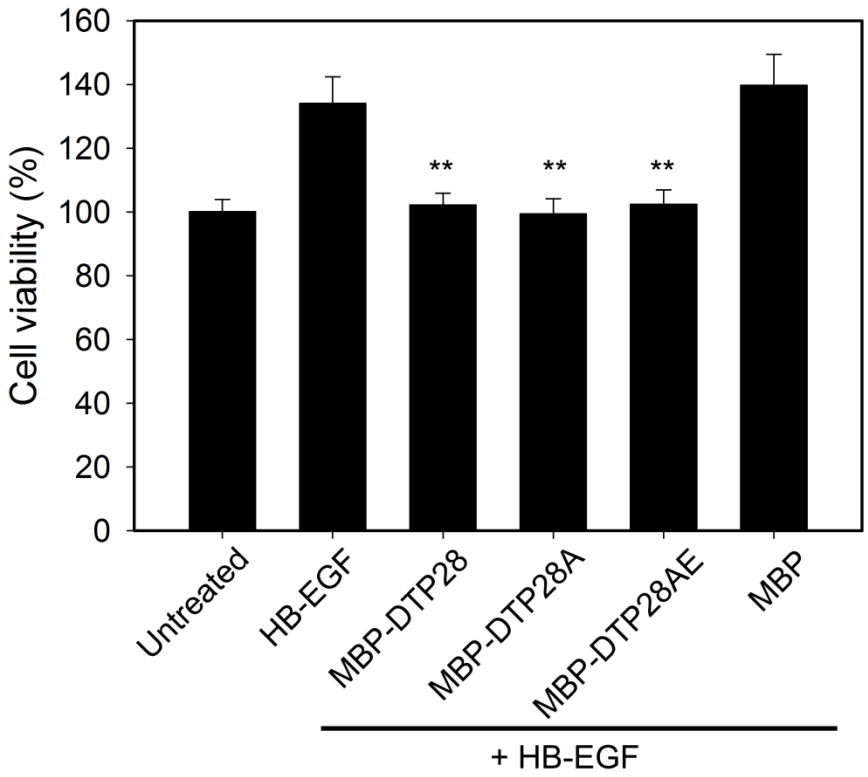

Figure 4.49: MBP-peptides inhibit HB-EGF induced increase in cell viability. The MDA-MB-468 cells were treated with HB-EGF in absence or presence of MBP or MBP-tagged peptides. The cell viability was measured by MTT assay. Each data point in the plot represents mean of six different wells. One way ANOVA with pairwise comparison was used. ** Significantly different from other treatment groups ($p<0.001$).

Highlights of the work:

- A short stretch corresponding to S505- F530 of DT can bind independently to HB-EGF.
- Computational study showed peptide, DTP28 might stably fold into a β-hairpin-like structure and bind to the binding groove on HB-EGF.
- The designed peptides, DTP28, DTP28A and DTP28AE bind to HB-EGF. The binding sites of these peptides might be the same binding site of the full-length RDT.
- MBP-tagged peptides bind to HB-EGF. These peptides are fused to a large protein that retains binding to HB-EGF.
- MBP-tagged peptides showed similar or slightly lesser affinities than RDT and full-length DT
- As short peptides, observed affinities in the range of 10^{-7} to 10^{-8} M is good.
- MBP-tagged peptides can modulate HB-EGF signaling and its mitogenic activity.

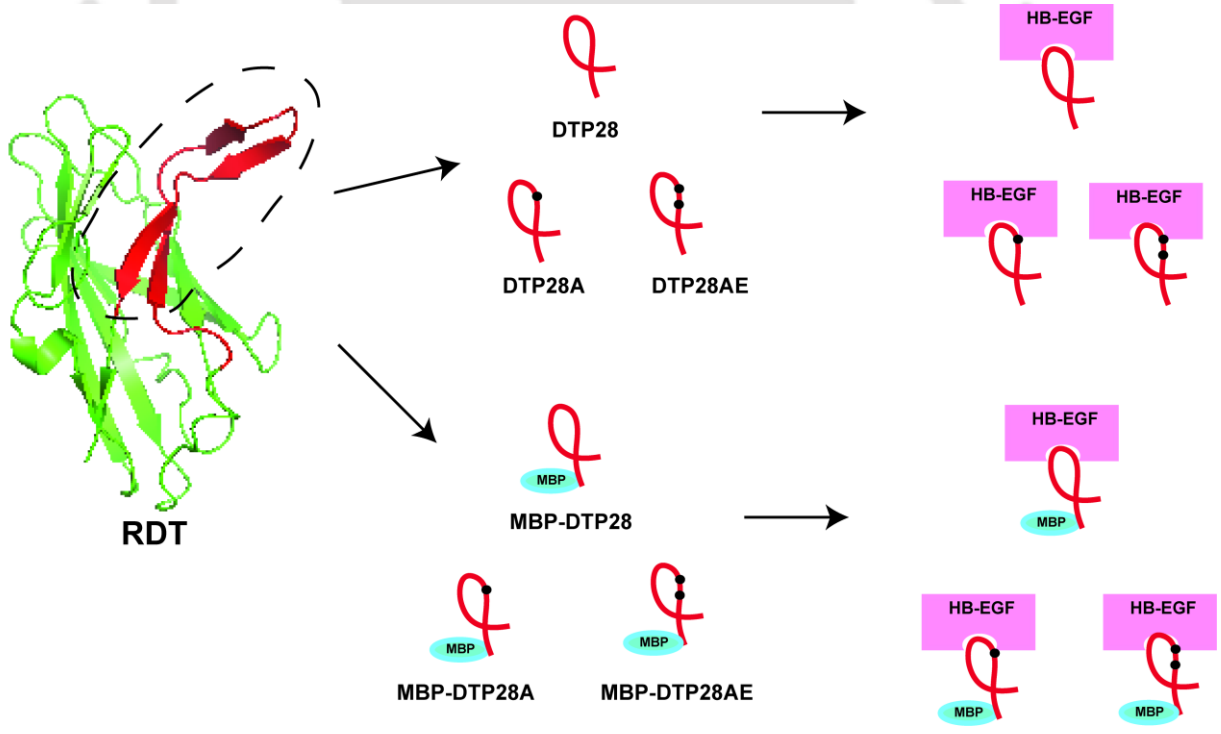

5 Conclusion & Scope for future work

Diphtheria toxin binds to cell surface HB-EGF and is internalized through receptor-mediated endocytosis. HB-EGF is overexpressed in several types of cancer. It is involved in oncogenic signaling leading to abnormal cell proliferation, cell migration, angiogenesis and development of drug resistance. Therefore, HB-EGF is a good target for therapeutic purpose. Targeting HB-EGF can attain two purposes: targeted drug delivery and blocking of oncogenic signaling. In the first part of our present study, we have used the recombinant receptor-binding domain of diphtheria toxin (RDT) to achieve specific and enhanced cellular uptake of nanoparticles. In the other part of the study, we have identified the short peptide derived from DT for receptor binding that binds to HB-EGF with reasonably moderate affinity.

We have used only the receptor-binding part of Diphtheria toxin, RDT, as a homing agent for targeted delivery of nanoparticles. An FDA approved, biodegradable, organic polymer, PLGA was used for the synthesis of these nanoparticles. The PLGA nanoparticles were synthesized using two different methods. We have observed that NPs synthesized using chloroform as a solvent are smaller in size. We have used this method in rest of the work. We have shown that these PLGA NPs were monodispersed, spherical and had a size of less than 50 nm. We have coated these NPs with recombinant RDT. RDT-coated NPs showed enhanced uptake in cells that express human HB-EGF. Furthermore, by competitive assay and by using specific inhibitors, we confirmed that internalization of RDT-NPs is through clathrin-dependent, receptor-mediated endocytosis. These observations also showed that the receptor-binding domain of Diphtheria toxin could trigger clathrin-dependent receptor-mediated endocytosis, even in absence of other domains of the toxin. Receptor-mediated endocytosis allows cell-specific, enhanced uptake of a payload. This may improve the potency of a drug. We have loaded RDT-coated NPs with Irinotecan, an anticancer drug. We observed that RDT-NPs increased the potency of the drug in cells that express human HB-EGF.

In the present work, we have shown that the recombinant receptor-binding domain of Diphtheria toxin can be used as a homing agent for targeted receptor-mediated delivery of NPs. We hope

the same protein may be conjugated to a drug for targeted drug delivery. However, further studies are required to understand stability, bio-distribution, tissue penetration, and organ/tissue-specific preferential accumulation of RDT-tagged drug delivery systems in a live organism. Few modifications are also required for future clinical translation of RDT-mediated cell-specific drug delivery systems. The covalent conjugation of RDT to NPs may enhance the stability of the drug delivery system. This will be more suitable for long-term *in vivo* uses. Possible *in vivo* use of RDT may be restricted by its immunogenicity. Several approaches, like PEGylation, site-directed mutagenesis to remove T-cell/B-cell epitopes, are used to reduce immunogenicity of therapeutic proteins, like immunotoxins and antibodies. Such techniques may also be used to reduce immunogenicity of RDT.

The other approach would be to reduce the size of RDT without compromising the receptor-binding ability. We can circumvent the problem of immunogenicity if we can identify RDT-based peptides that bind to HB-EGF. Peptides are usually less immunogenic and have higher tissue penetration than a large protein. If one can synthesize such a peptide, it can be used for targeting HB-EGF.

The second part of the current study is a step in that direction. We analyzed the structural aspects of DT-HB-EGF binding and identified a continuous stretch of 26 amino acids, corresponding to S505- F530 of DT that may bind to HB-EGF. We synthesized this peptide by solid-phase synthesis. It is called DTP28. We have also created two of its variants, namely DTP28A and DTP28AE. DTP28A has a G-to-A mutation that is expected to increase its affinity for HB-EGF. DTP28AE has another mutation (T-to-E) to reduce its immunogenicity to disturbing a T-cell epitope. Our computational studies showed that these peptides might bind to the designated binding site on HB-EGF. Using solid-phase ELISA we confirmed that these three peptides bind to HB-EGF. The binding sites of these peptides might be the same binding site of the full-length RDT. We have also investigated whether these peptides would retain binding to HB-EGF when fused to a large protein. That would allow one to graft these peptides on another functional protein to achieve targeting to HB-EGF. We cloned DTP28 into an MBP-vector to generate MBP-tagged DTP28 (MBP-DTP28). By using site-directed mutagenesis, other mutants, MBP-DTP28A and MBP-DTP28AE, were generated. These recombinant proteins were expressed in *E. coli* and were purified by affinity chromatography. We have shown that MBP-tagged peptides bind to HB-EGF. Further, we have found that these MBP-tagged peptides have a similar or slightly lesser affinity to HB-EGF, than RDT and full-length DT. However, considering that, these peptides represent only a short stretch of RDT; observed affinities in the

range of 10^{-7} to 10^{-8} M are remarkable. MBP-DTP28A and MBP-DTP28AE have an affinity similar to that of MBP-DTP28. This shows that a G510A mutation alone is not crucial for binding to HB-EGF and T517E mutation does not have a considerable effect on the affinity for HB-EGF. We have also investigated that MBP-tagged peptides can modulate the mitogenic activity of HB-EGF.

Here we have shown that this 26 amino acid-long stretch (S505- F530) in the receptor-binding domain is adequate for binding to HB-EGF. However, we do not know whether such a peptide can induce receptor-mediated endocytosis. Further studies are required to investigate this issue. We have shown that these peptides bind to HB-EGF. Therefore, it will be interesting to conjugate these peptides to drugs and investigate HB-EGF-targeted drug delivery using these peptide-drug conjugates. One may also attempt to use these peptides to achieve targeted delivery of nanoparticles to cells expressing HB-EGF. Additionally, the designed peptide can be fused with other proteins for cell-specific delivery. These peptides may be chemically modified to increase their stability.

Though it is expected that these peptides may be lesser immunogenic than RDT, one needs to perform extensively in vitro and *in vivo* immunogenicity assays. If required one can systematically mutate the peptides to reduce immunogenicity without compromising binding affinity. Similarly, one can also mutate these peptides to enhance the binding affinity for HB-EGF.

Bibliography

1. Collier RJ (1975) Diphtheria toxin: mode of action and structure. *Bacteriol Rev* 39(1):54-85.
2. Mitamura T, Higashiyama S, Taniguchi N, Klagsbrun M, & Mekada E (1995) Diphtheria toxin binds to the epidermal growth factor (EGF)-like domain of human heparin-binding EGF-like growth factor/diphtheria toxin receptor and inhibits specifically its mitogenic activity. *The Journal of biological chemistry* 270(3):1015-1019.
3. Collier RJ (2001) Understanding the mode of action of diphtheria toxin: a perspective on progress during the 20th century. *Toxicon* 39(11):1793-1803.
4. Bennett MJ & Eisenberg D (1994) Refined structure of monomeric diphtheria toxin at 2.3 A resolution. *Protein science : a publication of the Protein Society* 3(9):1464-1475.
5. Choe S*, et al.* (1992) The crystal structure of diphtheria toxin. *Nature* 357(6375):216-222.
6. Brooke JS, Cha JH, & Eidels L (1998) Diphtheria toxin:receptor interaction: association, dissociation, and effect of pH. *Biochem Biophys Res Commun* 248(2):297-302.
7. Miyazono K (2012) Ectodomain shedding of HB-EGF: a potential target for cancer therapy. *Journal of biochemistry* 151(1):1-3.
8. Sandvig K & Olsnes S (1980) Diphtheria toxin entry into cells is facilitated by low pH. *The Journal of cell biology* 87(3 Pt 1):828-832.
9. Oppenheimer NJ & Bodley JW (1981) Diphtheria toxin. Site and configuration of ADP-ribosylation of diphthamide in elongation factor 2. *The Journal of biological chemistry* 256(16):8579-8581.
10. Iwamoto R*, et al.* (1994) Heparin-binding EGF-like growth factor, which acts as the diphtheria toxin receptor, forms a complex with membrane protein DRAP27/CD9, which up-regulates functional receptors and diphtheria toxin sensitivity. *The EMBO journal* 13(10):2322-2330.
11. Moya M, Dautry-Varsat A, Goud B, Louvard D, & Boquet P (1985) Inhibition of coated pit formation in Hep2 cells blocks the cytotoxicity of diphtheria toxin but not that of ricin toxin. *The Journal of cell biology* 101(2):548-559.

12. Donovan JJ, Simon MI, Draper RK, & Montal M (1981) Diphtheria toxin forms transmembrane channels in planar lipid bilayers. *Proceedings of the National Academy of Sciences of the United States of America* 78(1):172-176.
13. Ratts R*, et al.* (2003) The cytosolic entry of diphtheria toxin catalytic domain requires a host cell cytosolic translocation factor complex. *The Journal of cell biology* 160(7):1139-1150.
14. Ren J*, et al.* (1999) Interaction of diphtheria toxin T domain with molten globule-like proteins and its implications for translocation. *Science (New York, N.Y.)* 284(5416):955-957.
15. Yamaizumi M, Mekada E, Uchida T, & Okada Y (1978) One molecule of diphtheria toxin fragment A introduced into a cell can kill the cell. *Cell* 15(1):245-250.
16. Kochi SK & Collier RJ (1993) DNA fragmentation and cytolysis in U937 cells treated with diphtheria toxin or other inhibitors of protein synthesis. *Experimental cell research* 208(1):296-302.
17. Kimura R, Iwamoto R, & Mekada E (2005) Soluble form of heparin-binding EGF-like growth factor contributes to retinoic acid-induced epidermal hyperplasia. *Cell Struct Funct* 30(2):35-42.
18. Iwamoto R, Mine N, Mizushima H, & Mekada E (2017) ErbB1 and ErbB4 generate opposing signals regulating mesenchymal cell proliferation during valvulogenesis. *Journal of cell science* 130(7):1321-1332.
19. Lian H*, et al.* (2012) Heparin-binding EGF-like growth factor induces heart interstitial fibrosis via an Akt/mTor/p70s6k pathway. *PloS one* 7(9):e44946.
20. Shirakata Y*, et al.* (2005) Heparin-binding EGF-like growth factor accelerates keratinocyte migration and skin wound healing. *Journal of cell science* 118(Pt 11):2363-2370.
21. Das SK*, et al.* (1994) Heparin-binding EGF-like growth factor gene is induced in the mouse uterus temporally by the blastocyst solely at the site of its apposition: a possible ligand for interaction with blastocyst EGF-receptor in implantation. *Development (Cambridge, England)* 120(5):1071-1083.
22. Mine N, Iwamoto R, & Mekada E (2005) HB-EGF promotes epithelial cell migration in eyelid development. *Development (Cambridge, England)* 132(19):4317-4326.
23. Iwamoto R*, et al.* (2003) Heparin-binding EGF-like growth factor and ErbB signaling is essential for heart function. *Proceedings of the National Academy of Sciences of the United States of America* 100(6):3221-3226.

24. Means AL*, et al.* (2003) Overexpression of heparin-binding EGF-like growth factor in mouse pancreas results in fibrosis and epithelial metaplasia. *Gastroenterology* 124(4):1020-1036.
25. Vinante F & Rigo A (2013) Heparin-binding epidermal growth factor-like growth factor/diphtheria toxin receptor in normal and neoplastic hematopoiesis. *Toxins (Basel)* 5(6):1180-1201.
26. Shimura T*, et al.* (2012) Nuclear translocation of the cytoplasmic domain of HB-EGF induces gastric cancer invasion. *BMC Cancer* 12:205.
27. Huang G, Besner GE, & Brigstock DR (2012) Heparin-binding epidermal growth factor-like growth factor suppresses experimental liver fibrosis in mice. *Lab Invest* 92(5):703-712.
28. Sauer L, Gitenay D, Vo C, & Baron VT (2010) Mutant p53 initiates a feedback loop that involves Egr-1/EGF receptor/ERK in prostate cancer cells. *Oncogene* 29(18):2628-2637.
29. Zhou ZN*, et al.* (2014) Autocrine HBEGF expression promotes breast cancer intravasation, metastasis and macrophage-independent invasion *in vivo*. *Oncogene* 33(29):3784-3793.
30. Miyamoto S, Yagi H, Yotsumoto F, Kawarabayashi T, & Mekada E (2006) Heparin-binding epidermal growth factor-like growth factor as a novel targeting molecule for cancer therapy. *Cancer Sci* 97(5):341-347.
31. Ongusaha PP*, et al.* (2004) HB-EGF is a potent inducer of tumor growth and angiogenesis. *Cancer research* 64(15):5283-5290.
32. Sato S, Drake AW, Tsuji I, & Fan J (2012) A potent anti-HB-EGF monoclonal antibody inhibits cancer cell proliferation and multiple angiogenic activities of HB-EGF. *PloS one* 7(12):e51964.
33. Miyamoto S*, et al.* (2011) A novel anti-human HB-EGF monoclonal antibody with multiple antitumor mechanisms against ovarian cancer cells. *Clinical cancer research : an official journal of the American Association for Cancer Research* 17(21):6733-6741.
34. Iwamoto R*, et al.* (2016) Characterization of a Novel Anti-Human HB-EGF Monoclonal Antibody Applicable for Paraffin-Embedded Tissues and Diagnosis of HB-EGF-Related Cancers. *Monoclon Antib Immunodiagn Immunother* 35(2):73-82.
35. Nishikawa K*, et al.* (2012) Development of anti-HB-EGF immunoliposomes for the treatment of breast cancer. *Journal of controlled release : official journal of the Controlled Release Society* 160(2):274-280.

36. Okamoto A*, et al.* (2014) Antibody-modified lipid nanoparticles for selective delivery of siRNA to tumors expressing membrane-anchored form of HB-EGF. *Biochem Biophys Res Commun* 449(4):460-465.
37. Higashiyama S, Lau K, Besner GE, Abraham JA, & Klagsbrun M (1992) Structure of heparin-binding EGF-like growth factor. Multiple forms, primary structure, and glycosylation of the mature protein. *The Journal of biological chemistry* 267(9):6205-6212.
38. Naglich JG, Metherall JE, Russell DW, & Eidels L (1992) Expression cloning of a diphtheria toxin receptor: identity with a heparin-binding EGF-like growth factor precursor. *Cell* 69(6):1051-1061.
39. Nakamura K, Iwamoto R, & Mekada E (1995) Membrane-anchored heparin-binding EGF-like growth factor (HB-EGF) and diphtheria toxin receptor-associated protein (DRAP27)/CD9 form a complex with integrin alpha 3 beta 1 at cell-cell contact sites. *The Journal of cell biology* 129(6):1691-1705.
40. Blobel CP (2005) ADAMs: key components in EGFR signalling and development. *Nat Rev Mol Cell Biol* 6(1):32-43.
41. Nanba D, Mammoto A, Hashimoto K, & Higashiyama S (2003) Proteolytic release of the carboxy-terminal fragment of proHB-EGF causes nuclear export of PLZF. *The Journal of cell biology* 163(3):489-502.
42. Higashiyama S, Abraham JA, Miller J, Fiddes JC, & Klagsbrun M (1991) A heparin-binding growth factor secreted by macrophage-like cells that is related to EGF. *Science (New York, N.Y.)* 251(4996):936-939.
43. Higashiyama S, Abraham JA, & Klagsbrun M (1993) Heparin-binding EGF-like growth factor stimulation of smooth muscle cell migration: dependence on interactions with cell surface heparan sulfate. *The Journal of cell biology* 122(4):933-940.
44. Nishi E, Prat A, Hospital V, Elenius K, & Klagsbrun M (2001) N-arginine dibasic convertase is a specific receptor for heparin-binding EGF-like growth factor that mediates cell migration. *The EMBO journal* 20(13):3342-3350.
45. Takemura T*, et al.* (2001) Induction of collecting duct morphogenesis in vitro by heparin-binding epidermal growth factor-like growth factor. *J Am Soc Nephrol* 12(5):964-972.
46. Iwamoto R & Mekada E (2006) ErbB and HB-EGF signaling in heart development and function. *Cell Struct Funct* 31(1):1-14.

47. Xie H, *et al.* (2007) Maternal heparin-binding-EGF deficiency limits pregnancy success in mice. *Proceedings of the National Academy of Sciences of the United States of America* 104(46):18315-18320.
48. Minami S, Iwamoto R, & Mekada E (2008) HB-EGF decelerates cell proliferation synergistically with TGFalpha in perinatal distal lung development. *Dev Dyn* 237(1):247-258.
49. Flamant M, Bollee G, Henique C, & Tharaux PL (2012) Epidermal growth factor: a new therapeutic target in glomerular disease. *Nephrol Dial Transplant* 27(4):1297-1304.
50. Miyamoto S, *et al.* (2004) Heparin-binding EGF-like growth factor is a promising target for ovarian cancer therapy. *Cancer research* 64(16):5720-5727.
51. Marikovsky M, *et al.* (1993) Appearance of heparin-binding EGF-like growth factor in wound fluid as a response to injury. *Proceedings of the National Academy of Sciences of the United States of America* 90(9):3889-3893.
52. Takemura T, Kondo S, Homma T, Sakai M, & Harris RC (1997) The membrane-bound form of heparin-binding epidermal growth factor-like growth factor promotes survival of cultured renal epithelial cells. *The Journal of biological chemistry* 272(49):31036-31042.
53. Stoll SW, Rittie L, Johnson JL, & Elder JT (2012) Heparin-binding EGF-like growth factor promotes epithelial-mesenchymal transition in human keratinocytes. *J Invest Dermatol* 132(9):2148-2157.
54. Leroy MC, Perroud J, Darbellay B, Bernheim L, & Konig S (2013) Epidermal growth factor receptor down-regulation triggers human myoblast differentiation. *PloS one* 8(8):e71770.
55. Chen X, *et al.* (1995) Induction of heparin-binding EGF-like growth factor expression during myogenesis. Activation of the gene by MyoD and localization of the transmembrane form of the protein on the myotube surface. *The Journal of biological chemistry* 270(31):18285-18294.
56. Zhang H, Chalothorn D, Jackson LF, Lee DC, & Faber JE (2004) Transactivation of epidermal growth factor receptor mediates catecholamine-induced growth of vascular smooth muscle. *Circ Res* 95(10):989-997.
57. Wang F, Sloss C, Zhang X, Lee SW, & Cusack JC (2007) Membrane-bound heparin-binding epidermal growth factor like growth factor regulates E-cadherin expression in pancreatic carcinoma cells. *Cancer research* 67(18):8486-8493.

58. El-Assal ON & Besner GE (2004) Heparin-binding epidermal growth factor-like growth factor and intestinal ischemia-reperfusion injury. *Seminars in pediatric surgery* 13(1):2-10.
59. Lian C*, et al.* (2016) Heparin-Binding Epidermal Growth Factor-Like Growth Factor as a Potent Target for Breast Cancer Therapy. *Cancer Biother Radiopharm* 31(3):85-90.
60. Shimura T*, et al.* (2008) Suppression of proHB-EGF carboxy-terminal fragment nuclear translocation: a new molecular target therapy for gastric cancer. *Clinical cancer research : an official journal of the American Association for Cancer Research* 14(12):3956-3965.
61. Tanaka Y*, et al.* (2005) Clinical significance of heparin-binding epidermal growth factor-like growth factor and a disintegrin and metalloprotease 17 expression in human ovarian cancer. *Clinical cancer research : an official journal of the American Association for Cancer Research* 11(13):4783-4792.
62. Wang F*, et al.* (2007) Heparin-binding EGF-like growth factor is an early response gene to chemotherapy and contributes to chemotherapy resistance. *Oncogene* 26(14):2006-2016.
63. Elenius K, Paul S, Allison G, Sun J, & Klagsbrun M (1997) Activation of HER4 by heparin-binding EGF-like growth factor stimulates chemotaxis but not proliferation. *The EMBO journal* 16(6):1268-1278.
64. Wee P & Wang Z (2017) Epidermal Growth Factor Receptor Cell Proliferation Signaling Pathways. *Cancers (Basel)* 9(5).
65. Schulze WX, Deng L, & Mann M (2005) Phosphotyrosine interactome of the ErbB-receptor kinase family. *Mol Syst Biol* 1:2005 0008.
66. Zarich N*, et al.* (2006) Grb2 is a negative modulator of the intrinsic Ras-GEF activity of hSos1. *Mol Biol Cell* 17(8):3591-3597.
67. Avruch J*, et al.* (2001) Ras activation of the Raf kinase: tyrosine kinase recruitment of the MAP kinase cascade. *Recent Prog Horm Res* 56:127-155.
68. McCubrey JA*, et al.* (2007) Roles of the Raf/MEK/ERK pathway in cell growth, malignant transformation and drug resistance. *Biochim Biophys Acta* 1773(8):1263-1284.
69. Yoon S & Seger R (2006) The extracellular signal-regulated kinase: multiple substrates regulate diverse cellular functions. *Growth Factors* 24(1):21-44.
70. Hemmings BA & Restuccia DF (2012) PI3K-PKB/Akt pathway. *Cold Spring Harb Perspect Biol* 4(9):a011189.

71. Mehta VB & Besner GE (2005) Heparin-binding epidermal growth factor-like growth factor inhibits cytokine-induced NF-kappa B activation and nitric oxide production via activation of the phosphatidylinositol 3-kinase pathway. *J Immunol* 175(3):1911-1918.
72. Vanhaesebroeck B & Alessi DR (2000) The PI3K-PDK1 connection: more than just a road to PKB. *Biochem J* 346 Pt 3:561-576.
73. Alao JP (2007) The regulation of cyclin D1 degradation: roles in cancer development and the potential for therapeutic invention. *Mol Cancer* 6:24.
74. Foss FM (2000) DAB(389)IL-2 (denileukin diftitox, ONTAK): a new fusion protein technology. *Clin Lymphoma* 1 Suppl 1:S27-31.
75. Peraino JS*, et al.* (2014) Diphtheria toxin-based bivalent human IL-2 fusion toxin with improved efficacy for targeting human CD25(+) cells. *J Immunol Methods* 405:57-66.
76. Piascik P (1999) FDA approves fusion protein for treatment of lymphoma. *J Am Pharm Assoc (Wash)* 39(4):571-572.
77. Weaver M & Laske DW (2003) Transferrin receptor ligand-targeted toxin conjugate (Tf-CRM107) for therapy of malignant gliomas. *J Neurooncol* 65(1):3-13.
78. Matar AJ*, et al.* (2012) Effect of pre-existing anti-diphtheria toxin antibodies on T cell depletion levels following diphtheria toxin-based recombinant anti-monkey CD3 immunotoxin treatment. *Transplant immunology* 27(1):52-54.
79. Robbins DH, Margulies I, Stetler-Stevenson M, & Kreitman RJ (2000) Hairy cell leukemia, a B-cell neoplasm that is particularly sensitive to the cytotoxic effect of anti-Tac(Fv)-PE38 (LMB-2). *Clinical cancer research : an official journal of the American Association for Cancer Research* 6(2):693-700.
80. Kreitman RJ*, et al.* (2001) Efficacy of the anti-CD22 recombinant immunotoxin BL22 in chemotherapy-resistant hairy-cell leukemia. *The New England journal of medicine* 345(4):241-247.
81. Aruna G (2006) Immunotoxins: a review of their use in cancer treatment. *Journal of stem cells & regenerative medicine* 1(1):31-36.
82. Giannini G, Rappuoli R, & Ratti G (1984) The amino-acid sequence of two non-toxic mutants of diphtheria toxin: CRM45 and CRM197. *Nucleic acids research* 12(10):4063-4069.
83. Dateoka S, Ohnishi Y, & Kakudo K (2012) Effects of CRM197, a specific inhibitor of HB-EGF, in oral cancer. *Medical molecular morphology* 45(2):91-97.
84. Gaillard PJ, Visser CC, & de Boer AG (2005) Targeted delivery across the blood-brain barrier. *Expert opinion on drug delivery* 2(2):299-309.

85. Tosi G*, et al.* (2015) Exploiting Bacterial Pathways for BBB Crossing with PLGA Nanoparticles Modified with a Mutated Form of Diphtheria Toxin (CRM197): In Vivo Experiments. *Molecular pharmaceutics* 12(10):3672-3684.
86. Kuo YC & Chung CY (2012) Transcytosis of CRM197-grafted polybutylcyanoacrylate nanoparticles for delivering zidovudine across human brain-microvascular endothelial cells. *Colloids and surfaces. B, Biointerfaces* 91:242-249.
87. Kuo YC & Liu YC (2014) Cardiolipin-incorporated liposomes with surface CRM197 for enhancing neuronal survival against neurotoxicity. *International journal of pharmaceutics* 473(1-2):334-344.
88. Hobel S, Appeldoorn CC, Gaillard PJ, & Aigner A (2011) Targeted CRM197-PEG-PEI/siRNA Complexes for Therapeutic RNAi in Glioblastoma. *Pharmaceuticals (Basel)* 4(12):1591-1606.
89. Kumar A, Das G, & Bose B (2014) Recombinant receptor-binding domain of diphtheria toxin increases the potency of curcumin by enhancing cellular uptake. *Molecular pharmaceutics* 11(1):208-217.
90. Nam SO*, et al.* (2016) Anti-tumor Effect of Intravenous Administration of CRM197 for Triple-negative Breast Cancer Therapy. *Anticancer research* 36(7):3651-3657.
91. Tang XH, Deng S, Li M, & Lu MS (2016) Cross-reacting material 197 reverses the resistance to paclitaxel in paclitaxel-resistant human ovarian cancer. *Tumour Biol* 37(4):5521-5528.
92. Tang XH, Li M, Deng S, & Lu MS (2014) Cross-reacting material 197, a heparin-binding EGF-like growth factor inhibitor, reverses the chemoresistance in human cisplatin-resistant ovarian cancer. *Anticancer Drugs* 25(10):1201-1210.
93. Tang XH, Deng S, Li M, & Lu MS (2012) The anti-tumor effect of cross-reacting material 197, an inhibitor of heparin-binding EGF-like growth factor, in human resistant ovarian cancer. *Biochem Biophys Res Commun* 422(4):676-680.
94. Hu Y*, et al.* (2015) CRM197 in Combination With shRNA Interference of VCAM-1 Displays Enhanced Inhibitory Effects on Human Glioblastoma Cells. *J Cell Physiol* 230(8):1713-1728.
95. Kunami N*, et al.* (2011) Antitumor effects of CRM197, a specific inhibitor of HB-EGF, in T-cell acute lymphoblastic leukemia. *Anticancer research* 31(7):2483-2488.
96. Suzuki K*, et al.* (2015) Identification of diphtheria toxin R domain mutants with enhanced inhibitory activity against HB-EGF. *Journal of biochemistry* 157(5):331-343.

97. Gillet D, Villiers B, Pichard S, Maillere B, & Sanson A (2015) Hb-egf inhibitor derived from the r domain of diphtheria toxin for the treatment of diseases associated with the activation of the hb-egf/egfr pathway. (Google Patents).
98. Shen WH, Choe S, Eisenberg D, & Collier RJ (1994) Participation of lysine 516 and phenylalanine 530 of diphtheria toxin in receptor recognition. *The Journal of biological chemistry* 269(46):29077-29084.
99. Marin JJ*, et al.* (2009) Importance and limitations of chemotherapy among the available treatments for gastrointestinal tumours. *Anticancer Agents Med Chem* 9(2):162-184.
100. Bae YH & Park K (2011) Targeted drug delivery to tumors: myths, reality and possibility. *Journal of controlled release : official journal of the Controlled Release Society* 153(3):198-205.
101. Torchilin VP (2010) Passive and active drug targeting: drug delivery to tumors as an example. *Handb Exp Pharmacol* (197):3-53.
102. Sultana S, Khan MR, Kumar M, Kumar S, & Ali M (2013) Nanoparticles-mediated drug delivery approaches for cancer targeting: a review. *J Drug Target* 21(2):107-125.
103. Akbarzadeh A*, et al.* (2013) Liposome: classification, preparation, and applications. *Nanoscale Res Lett* 8(1):102.
104. Bulbake U, Doppalapudi S, Kommineni N, & Khan W (2017) Liposomal Formulations in Clinical Use: An Updated Review. *Pharmaceutics* 9(2).
105. Huwyler J, Drewe J, & Krahenbuhl S (2008) Tumor targeting using liposomal antineoplastic drugs. *International journal of nanomedicine* 3(1):21-29.
106. Oerlemans C*, et al.* (2010) Polymeric micelles in anticancer therapy: targeting, imaging and triggered release. *Pharm Res* 27(12):2569-2589.
107. Madaan K, Kumar S, Poonia N, Lather V, & Pandita D (2014) Dendrimers in drug delivery and targeting: Drug-dendrimer interactions and toxicity issues. *J Pharm Bioallied Sci* 6(3):139-150.
108. Biswas S & Torchilin VP (2013) Dendrimers for siRNA Delivery. *Pharmaceuticals (Basel)* 6(2):161-183.
109. Leiro V, Santos SD, & Pego AP (2017) Delivering siRNA with Dendrimers: In Vivo Applications. *Curr Gene Ther* 17(2):105-119.
110. Rupp R, Rosenthal SL, & Stanberry LR (2007) VivaGel (SPL7013 Gel): a candidate dendrimer--microbicide for the prevention of HIV and HSV infection. *International journal of nanomedicine* 2(4):561-566.

111. Yavuz B, Pehlivan SB, & Unlu N (2013) Dendrimeric systems and their applications in ocular drug delivery. *ScientificWorldJournal* 2013:732340.
112. Prijic S & Sersa G (2011) Magnetic nanoparticles as targeted delivery systems in oncology. *Radiol Oncol* 45(1):1-16.
113. Li X*, et al.* (2009) Specific targeting of breast tumor by octreotide-conjugated ultrasmall superparamagnetic iron oxide particles using a clinical 3.0-Tesla magnetic resonance scanner. *Acta Radiol* 50(6):583-594.
114. Arvizo R, Bhattacharya R, & Mukherjee P (2010) Gold nanoparticles: opportunities and challenges in nanomedicine. *Expert opinion on drug delivery* 7(6):753-763.
115. Das S & Khuda-Bukhsh AR (2016) PLGA-loaded nanomedicines in melanoma treatment: Future prospect for efficient drug delivery. *Indian J Med Res* 144(2):181-193.
116. Wang J*, et al.* (2011) Folate-decorated hybrid polymeric nanoparticles for chemically and physically combined paclitaxel loading and targeted delivery. *Biomacromolecules* 12(1):228-234.
117. Hu K*, et al.* (2011) Lactoferrin conjugated PEG-PLGA nanoparticles for brain delivery: preparation, characterization and efficacy in Parkinson's disease. *International journal of pharmaceutics* 415(1-2):273-283.
118. Gryparis EC, Hatziapostolou M, Papadimitriou E, & Avgoustakis K (2007) Anticancer activity of cisplatin-loaded PLGA-mPEG nanoparticles on LNCaP prostate cancer cells. *European journal of pharmaceutics and biopharmaceutics : official journal of Arbeitsgemeinschaft fur Pharmazeutische Verfahrenstechnik e.V* 67(1):1-8.
119. Garinot M*, et al.* (2007) PEGylated PLGA-based nanoparticles targeting M cells for oral vaccination. *Journal of controlled release : official journal of the Controlled Release Society* 120(3):195-204.
120. Tosi G*, et al.* (2010) Sialic acid and glycopeptides conjugated PLGA nanoparticles for central nervous system targeting: In vivo pharmacological evidence and biodistribution. *Journal of controlled release : official journal of the Controlled Release Society* 145(1):49-57.
121. Gao J*, et al.* (2009) PE38KDEL-loaded anti-HER2 nanoparticles inhibit breast tumor progression with reduced toxicity and immunogenicity. *Breast cancer research and treatment* 115(1):29-41.
122. Firer MA & Gellerman G (2012) Targeted drug delivery for cancer therapy: the other side of antibodies. *J Hematol Oncol* 5:70.

123. Alley SC, Okeley NM, & Senter PD (2010) Antibody-drug conjugates: targeted drug delivery for cancer. *Curr Opin Chem Biol* 14(4):529-537.
124. Corrigan PA, Cicci TA, Auten JJ, & Lowe DK (2014) Ado-trastuzumab emtansine: a HER2-positive targeted antibody-drug conjugate. *Ann Pharmacother* 48(11):1484-1493.
125. Kantarjian H*, et al.* (2012) Inotuzumab ozogamicin, an anti-CD22-calecheamicin conjugate, for refractory and relapsed acute lymphocytic leukaemia: a phase 2 study. *Lancet Oncol* 13(4):403-411.
126. von Pawel J*, et al.* (2014) Phase II trial of mapatumumab, a fully human agonist monoclonal antibody to tumor necrosis factor-related apoptosis-inducing ligand receptor 1 (TRAIL-R1), in combination with paclitaxel and carboplatin in patients with advanced non-small-cell lung cancer. *Clin Lung Cancer* 15(3):188-196 e182.
127. Sun B, Ranganathan B, & Feng SS (2008) Multifunctional poly(D,L-lactide-co-glycolide)/montmorillonite (PLGA/MMT) nanoparticles decorated by Trastuzumab for targeted chemotherapy of breast cancer. *Biomaterials* 29(4):475-486.
128. Kou G*, et al.* (2007) Preparation and Characterization of Paclitaxel-loaded PLGA nanoparticles coated with cationic SM5-1 single-chain antibody. *Journal of biochemistry and molecular biology* 40(5):731-739.
129. Gupta B & Torchilin VP (2007) Monoclonal antibody 2C5-modified doxorubicin-loaded liposomes with significantly enhanced therapeutic activity against intracranial human brain U-87 MG tumor xenografts in nude mice. *Cancer immunology, immunotherapy : CII* 56(8):1215-1223.
130. Kurzrock R*, et al.* (2012) Safety, pharmacokinetics, and activity of GRN1005, a novel conjugate of angiopep-2, a peptide facilitating brain penetration, and paclitaxel, in patients with advanced solid tumors. *Molecular cancer therapeutics* 11(2):308-316.
131. Morisco A*, et al.* (2009) Micelles derivatized with octreotide as potential target-selective contrast agents in MRI. *Journal of peptide science : an official publication of the European Peptide Society* 15(3):242-250.
132. de Jong M, Breeman WA, Kwekkeboom DJ, Valkema R, & Krenning EP (2009) Tumor imaging and therapy using radiolabeled somatostatin analogues. *Accounts of chemical research* 42(7):873-880.
133. Okarvi SM (2008) Peptide-based radiopharmaceuticals and cytotoxic conjugates: potential tools against cancer. *Cancer treatment reviews* 34(1):13-26.
134. Barragan F*, et al.* (2012) Somatostatin subtype-2 receptor-targeted metal-based anticancer complexes. *Bioconjugate chemistry* 23(9):1838-1855.

135. Pierschbacher MD & Ruoslahti E (1984) Cell attachment activity of fibronectin can be duplicated by small synthetic fragments of the molecule. *Nature* 309(5963):30-33.
136. Xiong J, Balcioglu HE, & Danen EH (2013) Integrin signaling in control of tumor growth and progression. *The international journal of biochemistry & cell biology* 45(5):1012-1015.
137. He X*, et al.* (2015) RGD peptide-modified multifunctional dendrimer platform for drug encapsulation and targeted inhibition of cancer cells. *Colloids and surfaces. B, Biointerfaces* 125:82-89.
138. Bagley RG*, et al.* (2008) Human endothelial precursor cells express tumor endothelial marker 1/endosialin/CD248. *Molecular cancer therapeutics* 7(8):2536-2546.
139. Quan Q*, et al.* (2011) Imaging tumor endothelial marker 8 using an 18F-labeled peptide. *Eur J Nucl Med Mol Imaging* 38(10):1806-1815.
140. Kibria G, Hatakeyama H, & Harashima H (2011) A new peptide motif present in the protective antigen of anthrax toxin exerts its efficiency on the cellular uptake of liposomes and applications for a dual-ligand system. *International journal of pharmaceutics* 412(1-2):106-114.
141. Louch HA, Buczko ES, Woody MA, Venable RM, & Vann WF (2002) Identification of a binding site for ganglioside on the receptor binding domain of tetanus toxin. *Biochemistry* 41(46):13644-13652.
142. Townsend SA*, et al.* (2007) Tetanus toxin C fragment-conjugated nanoparticles for targeted drug delivery to neurons. *Biomaterials* 28(34):5176-5184.
143. Mathew A*, et al.* (2012) Curcumin loaded-PLGA nanoparticles conjugated with Tet-1 peptide for potential use in Alzheimer's disease. *PloS one* 7(3):e32616.
144. Park IK, Lasiene J, Chou SH, Horner PJ, & Pun SH (2007) Neuron-specific delivery of nucleic acids mediated by Tet1-modified poly(ethylenimine). *J Gene Med* 9(8):691-702.
145. Weisemann J, Stern D, Mahrhold S, Dorner BG, & Rummel A (2016) Botulinum Neurotoxin Serotype A Recognizes Its Protein Receptor SV2 by a Different Mechanism than Botulinum Neurotoxin B Synaptotagmin. *Toxins (Basel)* 8(5).
146. Andreu A, Fairweather N, & Miller AD (2008) Clostridium neurotoxin fragments as potential targeting moieties for liposomal gene delivery to the CNS. *Chembiochem : a European journal of chemical biology* 9(2):219-231.
147. Dobrenis K, Joseph A, & Rattazzi MC (1992) Neuronal lysosomal enzyme replacement using fragment C of tetanus toxin. *Proceedings of the National Academy of Sciences of the United States of America* 89(6):2297-2301.

148. Kawamura YI, *et al.* (2003) Cholera toxin activates dendritic cells through dependence on GM1-ganglioside which is mediated by NF-kappaB translocation. *Eur J Immunol* 33(11):3205-3212.
149. Gonzalez Porras MA, *et al.* (2016) A novel approach for targeted delivery to motoneurons using cholera toxin-B modified protocells. *J Neurosci Methods* 273:160-174.
150. Jacewicz M, Clausen H, Nudelman E, Donohue-Rolfe A, & Keusch GT (1986) Pathogenesis of shigella diarrhea. XI. Isolation of a shigella toxin-binding glycolipid from rabbit jejunum and HeLa cells and its identification as globotriaosylceramide. *J Exp Med* 163(6):1391-1404.
151. Obata F, *et al.* (2008) Shiga toxin 2 affects the central nervous system through receptor globotriaosylceramide localized to neurons. *The Journal of infectious diseases* 198(9):1398-1406.
152. Johansson D, *et al.* (2009) Expression of verotoxin-1 receptor Gb3 in breast cancer tissue and verotoxin-1 signal transduction to apoptosis. *BMC Cancer* 9:67.
153. Geyer PE, *et al.* (2016) Gastric Adenocarcinomas Express the Glycosphingolipid Gb3/CD77: Targeting of Gastric Cancer Cells with Shiga Toxin B-Subunit. *Molecular cancer therapeutics* 15(5):1008-1017.
154. Kovbasnjuk O, *et al.* (2005) The glycosphingolipid globotriaosylceramide in the metastatic transformation of colon cancer. *Proceedings of the National Academy of Sciences of the United States of America* 102(52):19087-19092.
155. Maak M, *et al.* (2011) Tumor-specific targeting of pancreatic cancer with Shiga toxin B-subunit. *Molecular cancer therapeutics* 10(10):1918-1928.
156. Distler U, *et al.* (2009) Shiga toxin receptor Gb3Cer/CD77: tumor-association and promising therapeutic target in pancreas and colon cancer. *PloS one* 4(8):e6813.
157. Amessou M, *et al.* (2008) Retrograde delivery of photosensitizer (TPPp-O-beta-GluOH)3 selectively potentiates its photodynamic activity. *Bioconjugate chemistry* 19(2):532-538.
158. Tarrago-Trani MT, Jiang S, Harich KC, & Storrie B (2006) Shiga-like toxin subunit B (SLTB)-enhanced delivery of chlorin e6 (Ce6) improves cell killing. *Photochem Photobiol* 82(2):527-537.
159. El Alaoui A, *et al.* (2008) Synthesis and properties of a mitochondrial peripheral benzodiazepine receptor conjugate. *ChemMedChem* 3(11):1687-1695.

160. Huey R, Hawthorne S, & McCarron P (2017) The potential use of rabies virus glycoprotein-derived peptides to facilitate drug delivery into the central nervous system: a mini review. *J Drug Target* 25(5):379-385.
161. Fu A, Wang Y, Zhan L, & Zhou R (2012) Targeted delivery of proteins into the central nervous system mediated by rabies virus glycoprotein-derived peptide. *Pharm Res* 29(6):1562-1569.
162. Kim SS*, et al.* (2010) Targeted delivery of siRNA to macrophages for anti-inflammatory treatment. *Mol Ther* 18(5):993-1001.
163. Chen W*, et al.* (2011) Targeted brain delivery of itraconazole via RVG29 anchored nanoparticles. *J Drug Target* 19(3):228-234.
164. Bradford MM (1976) A rapid and sensitive method for the quantitation of microgram quantities of protein utilizing the principle of protein-dye binding. *Analytical biochemistry* 72:248-254.
165. Kocbek P, Obermajer N, Cegnar M, Kos J, & Kristl J (2007) Targeting cancer cells using PLGA nanoparticles surface modified with monoclonal antibody. *Journal of controlled release : official journal of the Controlled Release Society* 120(1-2):18-26.
166. Chaubey NS, A. K.; Chattopadhyay, A.; Ghosh, S. S (2014) Silver nanoparticle loaded PLGA composite nanoparticles for improving therapeutic efficacy of recombinant IFN[gamma] by targeting the cell surface. *Biomater. Sci.* 2(8):1080– 1089.
167. Schneider CA, Rasband WS, & Eliceiri KW (2012) NIH Image to ImageJ: 25 years of image analysis. *Nat Methods* 9(7):671-675.
168. Mosmann T (1983) Rapid colorimetric assay for cellular growth and survival: application to proliferation and cytotoxicity assays. *J Immunol Methods* 65(1-2):55-63.
169. Schagger H (2006) Tricine-SDS-PAGE. *Nat Protoc* 1(1):16-22.
170. Louis-Jeune C, Andrade-Navarro MA, & Perez-Iratxeta C (2012) Prediction of protein secondary structure from circular dichroism using theoretically derived spectra. *Proteins* 80(2):374-381.
171. Kurcinski M, Jamroz M, Blaszczyk M, Kolinski A, & Kmiecik S (2015) CABS-dock web server for the flexible docking of peptides to proteins without prior knowledge of the binding site. *Nucleic acids research* 43(W1):W419-424.
172. Pettersen EF*, et al.* (2004) UCSF Chimera--a visualization system for exploratory research and analysis. *J Comput Chem* 25(13):1605-1612.
173. Pronk S*, et al.* (2013) GROMACS 4.5: a high-throughput and highly parallel open source molecular simulation toolkit. *Bioinformatics* 29(7):845-854.

174. Laemmli UK (1970) Cleavage of structural proteins during the assembly of the head of bacteriophage T4. *Nature* 227(5259):680-685.
175. Lowry OH, Rosebrough NJ, Farr AL, & Randall RJ (1951) Protein measurement with the Folin phenol reagent. *J Biol Chem* 193(1):265-275.
176. Danhier F*, et al.* (2012) PLGA-based nanoparticles: an overview of biomedical applications. *Journal of controlled release : official journal of the Controlled Release Society* 161(2):505-522.
177. Zhang S, Gao H, & Bao G (2015) Physical Principles of Nanoparticle Cellular Endocytosis. *ACS nano* 9(9):8655-8671.
178. Oh N & Park JH (2014) Endocytosis and exocytosis of nanoparticles in mammalian cells. *International journal of nanomedicine* 9 Suppl 1:51-63.
179. Saha C, Kaushik A, Das A, Pal S, & Majumder D (2016) Anthracycline Drugs on Modified Surface of Quercetin-Loaded Polymer Nanoparticles: A Dual Drug Delivery Model for Cancer Treatment. *PloS one* 11(5):e0155710.
180. Wang M*, et al.* (2015) Synchrotron radiation-based Fourier-transform infrared spectromicroscopy for characterization of the protein/peptide distribution in single microspheres. *Acta pharmaceutica Sinica. B* 5(3):270-276.
181. Steinman RM, Mellman IS, Muller WA, & Cohn ZA (1983) Endocytosis and the recycling of plasma membrane. *The Journal of cell biology* 96(1):1-27.
182. Wang LH, Rothberg KG, & Anderson RG (1993) Mis-assembly of clathrin lattices on endosomes reveals a regulatory switch for coated pit formation. *The Journal of cell biology* 123(5):1107-1117.
183. Orlandi PA & Fishman PH (1998) Filipin-dependent inhibition of cholera toxin: evidence for toxin internalization and activation through caveolae-like domains. *The Journal of cell biology* 141(4):905-915.
184. Daecke J, Fackler OT, Dittmar MT, & Krausslich HG (2005) Involvement of clathrin-mediated endocytosis in human immunodeficiency virus type 1 entry. *Journal of virology* 79(3):1581-1594.
185. Ramesh M, Ahlawat P, & Srinivas NR (2010) Irinotecan and its active metabolite, SN-38: review of bioanalytical methods and recent update from clinical pharmacology perspectives. *Biomedical chromatography : BMC* 24(1):104-123.
186. Komuro H*, et al.* (1994) Effects of CPT-11 (a unique DNA topoisomerase I inhibitor) on a highly malignant xeno-transplanted neuroblastoma. *Medical and pediatric oncology* 23(6):487-492.

187. Dean FB & Cozzarelli NR (1985) Mechanism of strand passage by Escherichia coli topoisomerase I. The role of the required nick in catenation and knotting of duplex DNA. *The Journal of biological chemistry* 260(8):4984-4994.
188. Fujita K, Kubota Y, Ishida H, & Sasaki Y (2015) Irinotecan, a key chemotherapeutic drug for metastatic colorectal cancer. *World journal of gastroenterology* 21(43):12234-12248.
189. Kipps E, Young K, & Starling N (2017) Liposomal irinotecan in gemcitabine-refractory metastatic pancreatic cancer: efficacy, safety and place in therapy. *Therapeutic advances in medical oncology* 9(3):159-170.
190. Hajian R & Guan Huat T (2012) *Spectrophotometric Studies on the Thermodynamics of the ds-DNA Interaction with Irinotecan for a Better Understanding of Anticancer Drug-DNA Interactions*.
191. Riviere K, Kieler-Ferguson HM, Jerger K, & Szoka FC, Jr. (2011) Anti-tumor activity of liposome encapsulated fluoroorotic acid as a single agent and in combination with liposome irinotecan. *Journal of controlled release : official journal of the Controlled Release Society* 153(3):288-296.
192. Louie GV, Yang W, Bowman ME, & Choe S (1997) Crystal structure of the complex of diphtheria toxin with an extracellular fragment of its receptor. *Molecular cell* 1(1):67-78.
193. Lee CW, Lee SF, & Halperin SA (2004) Expression and immunogenicity of a recombinant diphtheria toxin fragment A in Streptococcus gordonii. *Applied and environmental microbiology* 70(8):4569-4574.
194. Diethelm-Okita BM, Okita DK, Banaszak L, & Conti-Fine BM (2000) Universal epitopes for human CD4+ cells on tetanus and diphtheria toxins. *The Journal of infectious diseases* 181(3):1001-1009.
195. Pastor MT, Lopez de la Paz M, Lacroix E, Serrano L, & Perez-Paya E (2002) Combinatorial approaches: a new tool to search for highly structured beta-hairpin peptides. *Proceedings of the National Academy of Sciences of the United States of America* 99(2):614-619.
196. Mahalakshmi R, Shanmugam G, Polavarapu PL, & Balaram P (2005) Circular dichroism of designed peptide helices and beta-hairpins: analysis of Trp- and Tyr-rich peptides. *Chembiochem : a European journal of chemical biology* 6(12):2152-2158.
197. Sreerama N & Woody RW (2003) Structural composition of betaI- and betaII-proteins. *Protein science : a publication of the Protein Society* 12(2):384-388.

198. Wu J, Yang JT, & Wu CS (1992) Beta-II conformation of all-beta proteins can be distinguished from unordered form by circular dichroism. *Analytical biochemistry* 200(2):359-364.
199. Skwierawska A, Makowska J, Oldziej S, Liwo A, & Scheraga HA (2009) Mechanism of formation of the C-terminal beta-hairpin of the B3 domain of the immunoglobulin binding protein G from Streptococcus. I. Importance of hydrophobic interactions in stabilization of beta-hairpin structure. *Proteins* 75(4):931-953.
200. Skwierawska A, Oldziej S, Liwo A, & Scheraga HA (2009) Conformational studies of the C-terminal 16-amino-acid-residue fragment of the B3 domain of the immunoglobulin binding protein G from Streptococcus. *Biopolymers* 91(1):37-51.
201. Schenk GJ*, et al.* (2012) Efficient CRM197-mediated drug targeting to monocytes. *Journal of controlled release : official journal of the Controlled Release Society* 158(1):139-147.
202. Stenmark H, Moskaug JO, Madshus IH, Sandvig K, & Olsnes S (1991) Peptides fused to the amino-terminal end of diphtheria toxin are translocated to the cytosol. *The Journal of cell biology* 113(5):1025-1032.
203. Auger A*, et al.* (2015) Efficient Delivery of Structurally Diverse Protein Cargo into Mammalian Cells by a Bacterial Toxin. *Molecular pharmaceutics* 12(8):2962-2971.
204. Sorensen HP & Mortensen KK (2005) Soluble expression of recombinant proteins in the cytoplasm of Escherichia coli. *Microbial cell factories* 4(1):1.
205. Miyamoto S*, et al.* (2007) New approach to cancer therapy: heparin binding-epidermal growth factor-like growth factor as a novel targeting molecule. *Anticancer research* 27(6A):3713-3721.

Appendix

General reagents: Acetic acid, chloroform, di-sodium hydrogen phosphate, glycerol, hydrochloric acid, isopropyl alcohol, isoamyl alcohol, methanol, potassium acetate, sulphuric acid, ethanol, sodium chloride (all of AR grade) – from HiMedia, India and Merck, India.

Molecular biology grade reagents/ chemicals: Acrylamide, APS, bis-acryl amide, TEMED, APS, EDTA, IPTG, phenol, DAB, tween 20, triton X 100, PLGA, PVA, Rhodamine 123, Potassium bromide (KBr), NP40, Transferrin-FITC, Sodium deoxycholate, Bradford's reagent - from Sigma-Aldrich, USA. Tricine, Magnesium chloride, disodium citrate, boric acid, glycine, SDS, tris–base, imidazole, Nickel sulphate heptahydrate, Silver nitrate, ampicillin, chloramphenicol, tetracycline from Himedia, India.

Components for bacterial culture medium: Bacto-agar, yeast extract, tryptone- from Himedia, India.

Components for mammalian cell culture medium: DMEM from HiMedia, antibiotic and Trypsin (0.25%) fetal calf serum- from Invitogen,, sodium bicarbonate- from Sigma-Aldrich, U.S.A.

Enzymes: PCR master mix from HiMedia, India. *Nde I* and *Xho I*, from NEB, UK.. Quick DNA ligase from- NEB, UK, KLD mix in Q5 site directed mutagenesis kit from NEB, UK.

Blotting Membranes and Filters: PVDF membrane (0.2 µm) - from Milipore, U.S.A. 3mm filter paper - from Whatman, USA.

DNA and protein markers: 100 bp and 1 kb DNA ladder and protein molecular weight marker (11-175KD) - from HiMedia, India.

Plastic and Glasswares: micro pipette tips, micro centrifuge tubes, petri dishes and other plastic wares- from Tarson Products Pvt. Ltd., India. PCR tubes - from Axygen, USA; Glassware- from Borosil International, India.

Cell lines: All the cell lines were procured from National Centre for Cell Science, Pune, India.

Figure:

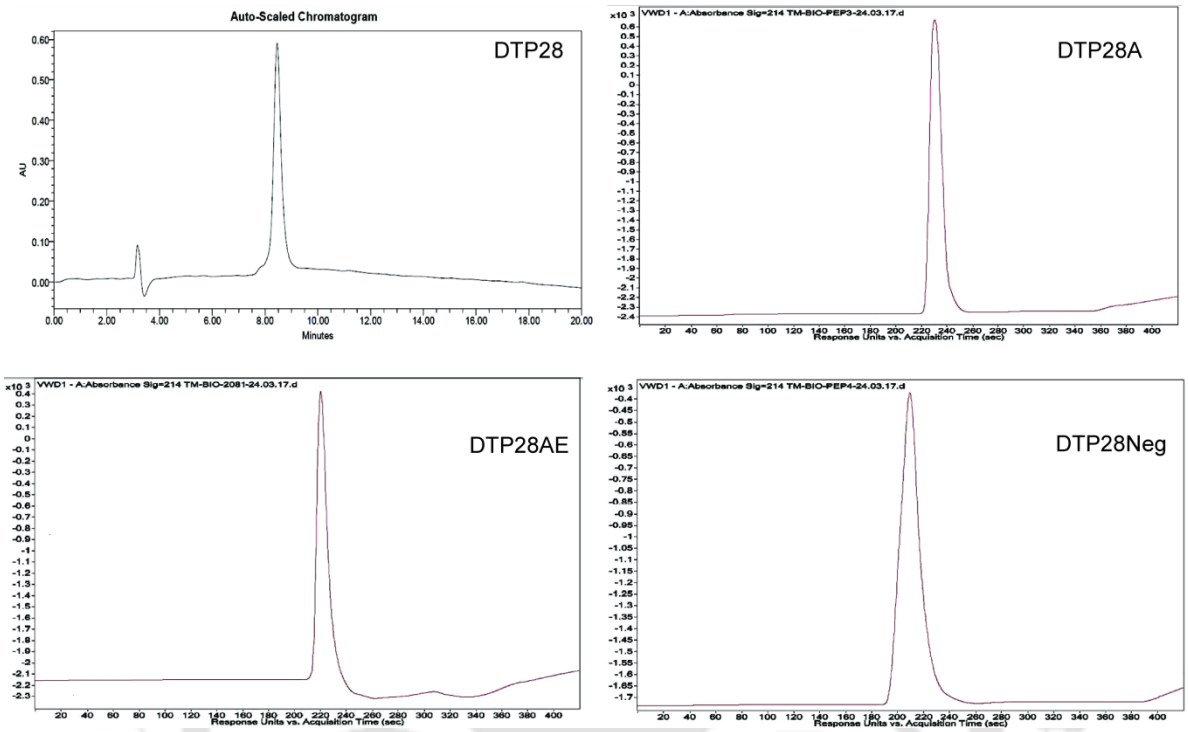

Figure A1: Characterization of peptide by HPLC for DTP28, DTP28A, DTP28AE, and DTP28Neg.

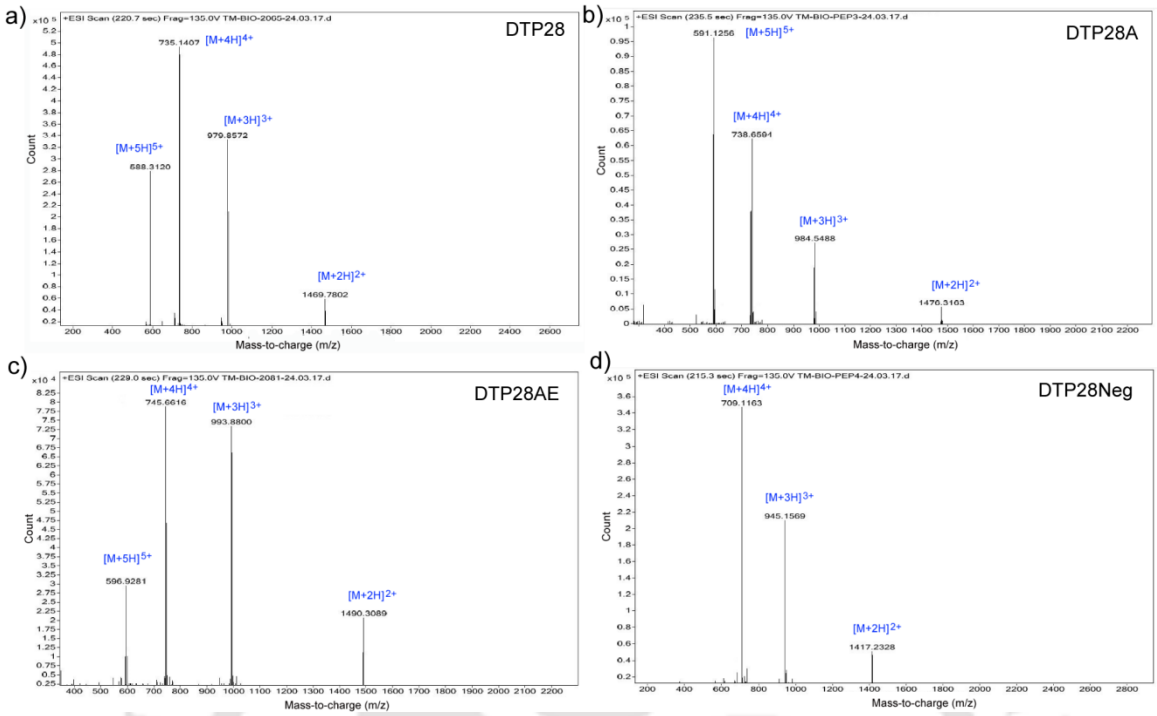

Figure A2: ESI Mass Spectrometry data for DTP28, DTP28A, DTP28AE, and DTP28Neg.

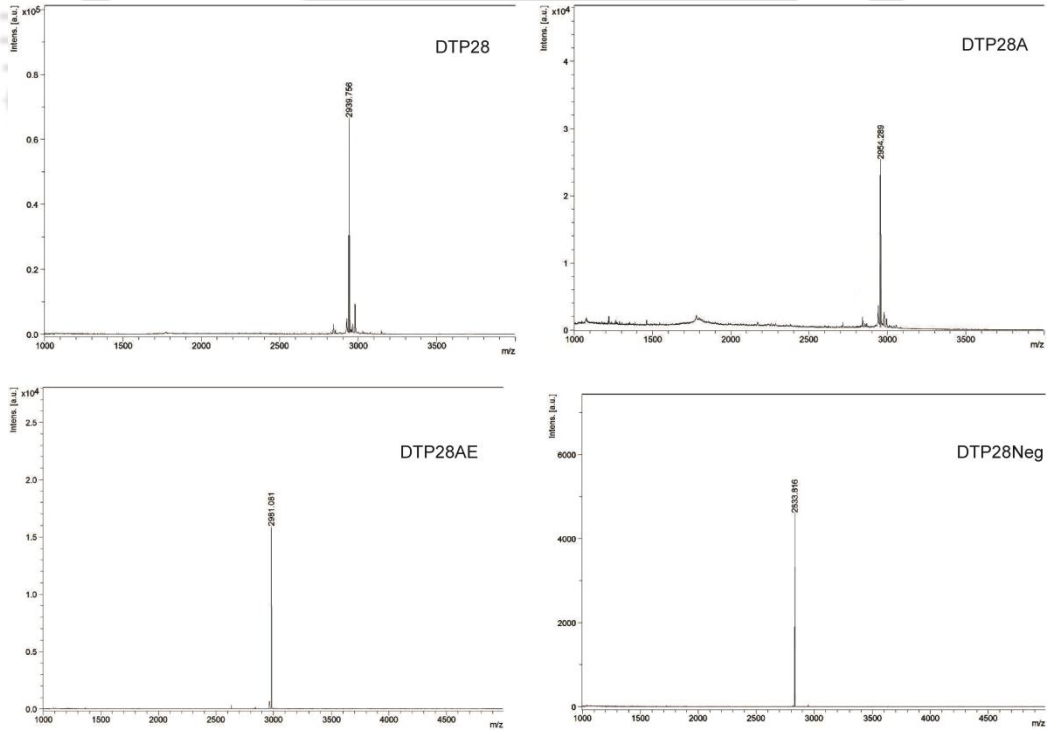

Figure A3: MALDI data for DTP28, DTP28A, DTP28AE, and DTP28Neg.

Table:

Table A1. List of Plasmid Vector

Name	Use	Promoter	Selection marker(s)	Cloning Site
pET-22b RDT (Novagen)	Bacterial expression Vector	P T7- lacO	Amp^R	ΔN-RDT cloned at *BamH I*/*Xho I* site.
MBP-DTP28	Bacterial expression Vector	P T7- lacO	Amp^R	DTP28 cloned at Nde I/Xho I site.

Table. A2. List of Bacterial Strain

Strain	Description
Escherichia coli DH5α (Novagen)	F′ϕ80d*lac*ZΔM15 Δ (*lac*ZYA- *arg*F) U169 *end*A1 *rec*A1 *hsd*R17 ($r_k^- m_k^+$) *deo*R *thi*-1 *pho*A *sup*E44 λ^- *gyr*A96 *rel*A1
Escherichia coli BL21 (DE3) (Novagen)	F^- *ompT hsdS*$_B$ ($r_B^- m_B^-$) *gal dcm* (DE3).Derivation of B834.(Parental strain:B834; Resistance :none)

Table. A3. Culture Medium for Bacteria

Media	Constituents	Concentration	pH
Luria broth (LB)	Bactotryptone	1.0%	7.2
	Yeast extract	0.5%	
	NaCl	0.5%	
2xTY	Bactotryptone	1.6%	7.2
	Yeast extract	1.0%	

	NaCl	0.5%	
TYA	Bactotryptone	1.0%	7.2
	Yeast extract	0.5%	
	NaCl	0.8%	
	Agar	1.5%	
TYA/AMP	TYA media		7.2
	Ampicillin	100 µg/ ml	
TYA/AMP/Glu	TYA/AMP media		7.2
	Glucose	1%	

Table. A4. Culture Medium for Animal Cell

Media	Constituents	pH
DMEM (Cat. No. AT007A-10x1L)	DMEM powder with high glucose for 1 liter, 3.7g $NaHCO_3$.	7.4, adjusted with 1N HCL
DMEM with serum	DMEM, 10% serum, 1 X Antibiotic.	7.4
Freezing Media	95% fetal bovine serum, 5% DMSO	7.4

Table. A5. List of Buffers and Solutions

Buffers / Solutions	Composition
Tris-EDTA (TE) buffer	0.01 M Tris-HCl (pH 7.4), 0.001 M Na_2-EDTA (pH 8.0)
TAE - Tris Acetate EDTA buffer, 50x (100ml)	24.2 g Tris base, 5.71 ml CH_3COOH, 10 ml of 0.5 M EDTA.

Phosphate buffer saline (PBS)	0.137 M NaCl, 2.68 mM KCl, 7.98 mM Na_2HPO_4, 1.4 mM KH_2PO_4, pH 7.2.
PBST	PBS containing 0.1% Tween -20
TBS	50mM tris base, 150mM NaCl
TBST	TBS containing 0.1% Tween -20
Trypsin- EDTA	0.05% Trypsin, 0.53mM EDTA in PBS
RIPA buffer	50 mM Tris-HCl, pH 7.5, 150 mM NaCl, 1% Nonidet P40, 0.5% sodium deoxycholate, 0.1% SDS.
Formaldehyde solution	3.7% formaldehyde solution by diluting the 37% formaldehyde stock with 1X PBS.

Solutions for competent cell preparation

Sterile $CaCl_2$	50 mM $CaCl_2$ is filter sterilized through a 0.22µ filter (HiMedia)
Sterile Glycerol (50%)	20 ml 100% Glycerol is added in 20 ml water and sterilized by autoclaving.

Buffers/solutions for protein purification

Stripping Buffer	20 mM sodium phosphate, 500 mM NaCl, 50 mM EDTA, pH 7.4.
Recharging Buffer	2.5 ml of 100 mM Nickel sulphate hepta-hydrate in distilled water.
Equilibration Buffer	20 mM sodium phosphate, 500 mM NaCl, 40 mM Imidazole, pH 7.4.
Binding Buffer	20 mM sodium phosphate, 500 mM NaCl, 40 mM Imidazole, pH 7.4.
Elution Buffer	20 mM sodium phosphate, 500 mM NaCl, 250 mM Imidazole, pH 7.4

Buffers/solutions for SDS-PAGE

30 % acrylamide-bisacrylamide solution (100ml)	29.2 g Acrylamide, 0.8 g Bisacrylamide
Tris.HCl, pH 6.8, 0.5 M (100 ml)	6.06 g of Tris base, pH adjusted to 6.8 with

	2 N HCl.
Tris.HCl, pH 8.8, 1.5 M (100 ml)	18.18 g of Tris base, pH adjusted to 8.8 with 2 N HCl.
Gel Running Buffer	25 mM Tris base, 250 mM, 0.1% SDS
Sample Loading Buffer (1X)	50 mM Tris-HCl pH 6.8, 2% SDS, 10% glycerol, 1% β-mercaptoethanol, 0.02 % bromophenol blue
Staining solution	50% Methanol, 10% Acetic acid, 40% Water, 0.25% CBB R250
Destaining solution	30% Methanol, 10% Acetic acid, 60% Water.

Buffers/solutions for Western Blot

Transfer buffer	25 mM Tris base, 39 mM Glycine, 20 % Methanol
Ponceau solution (Sigma)	0.1% Ponceau S in 5% acetic acid
Blocking Solution	3% BSA in TBST.
Washing buffer	PBST or TBST

Solutions for Lowry's Method of protein estimation

Lowry A	2% Na_2CO_3 in 0.1N NaOH
Lowry B1	2% Sodium potassium tartrate in water
Lowry B2	2% $CuSO_4.5H_2O$ in water
Lowry C	B1:A:B2 = 1:100:1

Buffers/solutions for Tricine SDS-PAGE

Anode buffer (10X)	1M Tris-HCl, pH 8.9
Cathode buffer (10X)	1M Tris-HCl, 1M Tricine, 1% SDS, pH 8.25
Gel buffer (3X)	3M Tris-HCl, 0.3% SDS, pH 8.45
AB-6	46.5 g of Acrylamide, 3 g of Bis-acrylamide
Resolving gel (16%/6M Urea)	3.33 ml AB-6, 3.33 ml gel buffer (3X), 1 ml Glycerol, 33.3 µl APS, 3.3 µl TEMED and

	3.6 g Urea
Stacking gel (4%)	0.33 ml AB-6, 1 ml gel buffer (3X), 30 µl APS, 3 µl TEMED and 2.7 ml water

Buffers/Solutions for Silver staining

Fixing solution	20 ml Ethanol, 5 ml Acetic acid, 25 ml water
Incubation solution	25 ml Ethanol, 2.4 g sodium acetate, 0.25 ml Glyceraldehyde, 0.1 g sodium thiosulphate, 25 ml water.
Silver solution	50 mg silver nitrate, 10 µl formaldehyde dissolve in 50 ml water
Developing solution	1.25 g Sodium carbonate dissolve in 50 ml water
Stop solution	0.73 g Disodium EDTA dissolve in 50 ml water

Buffers/Solutions for SPR

Amine-coupling reagent(A)	0.4 M 1-ethyl-3-(3-dimethylamino-propyl)carbodiimide hydrochloride in water, pH 7.4.
Amine-coupling reagent(B)	0.1 M N-hydroxysuccinimide in water,pH 7.4.
Ethanolamine solution	1.0 M ethanolamine-HCl, pH 8.5
Coupling Buffer	10 mM sodium acetate, pH 4.0, 4.5, 5.0, 5.5.
Regeneration Buffer	10 mM, pH 1.5, 2.0, 2.5, 3.0
Running Buffer	10 mM Na_2HPO_4–NaH_2PO_4, 150 mM NaCl, pH 7.4
Equilibration Buffer	10 mM Na_2HPO_4–NaH_2PO_4, 150mM NaCl, 0.05% Tween 20, pH 7.4

Buffers/Solutions for ELISA

Substrate solution	O-phenylenediamine (0.4 mg/ml) diluted in 0.05 M citric acid and 0.1 M Na_2HPO_4,pH 5.0 and 0.03% H_2O_2

Stop solution	8 N Sulphuric acids.

Table. A6. List of Antibody

Name	Sourse/ Type	Working condition	Working dilution	Use
Anti-human HB-EGF (R&D System, U.S.A, # MAB259)	Mouse/ monoclonal	RT/ 2 hr	1:1000	ELISA
Anti-Histidine-tagged protein (Calbiochem, Germany,# 0B05)	Mouse / monoclonal	RT/ 2 hr	1:1000	ELISA,
Anti-human phospho- p44/42 MAPK (Erk1/2) (Thr202/Tyr204) (Cell signaling, U.S.A, # 4370)	Rabbit/ monoclonal	4 °C/ ON	1:1000	WB
Anti-human p44/42 MAPK (Erk1/2) (Cell Signaling,U.S.A, # 4695)	Rabbit/ monoclonal	4 °C/ ON	1:1000	WB
Anti-human Histone H3 (Cell Signaling, U.S.A, # 4850)	Rabbit/ monoclonal	4 °C/ ON	1:2000	WB
Anti Mouse-HRP (Sigma, U.S.A, # A0412)	Goat	RT/ 2 hr	1:1000	ELISA
Anti Rabbit-HRP (Cell Signaling, U.S.A, # 7074)	Goat	RT/ 2 hr	1:5000	WB

RT: Room Temperature, ON: Over Night, W.B: Western Blot.

Table A7. List of Primers

Name	Sequence	Annealing Temp.(°C)	Final Conc (nM)
	Primers set for cloning		
DTP28	DTP28 FP: 5'-GCAACATATGGGCTCATCGGATTCCATAGGC-3' DTP28 RP: 5'-GCAACTCGAGTCAGCCAAATAGCGATAGCTTAG-3'	60 ˚C	200
	Note: Restriction enzyme sites are underlined		
	Primers set for site directed mutagenesis		
MBP-DTP28A	G510A FP: 5'-GATTCCATAG**C**CGTTCTTGG-3' G510A RP: 5'-CGATGAGCCCATATGGGC-3'	52 ˚C	200
MBP-DTP28AE	T517E FP: 5'-GGTACCAGAAA**GA**AGTAGATCAC-3' T517E RP: 5'-CAAGAACGGCTATGGAATCC-3'	51 ˚C	200
MBP-DTP28Neg	Neg F1: CATAGGC**CC**TCTTGGGTAC**GGC**AAAACAG Neg R1: GAATCCGATGAGCCCATATGGGCGC	59 ˚C	200
	Neg F2: GTTAATTCT**CC**GCTATCGCTAT Neg R2: CTTGGTGTGATCTACTGTTTTG	47 ˚C	200
	Note: Mutated bases are shown in bold.		
	Primer set for sequencing		
T7 primers	T7 Forw: TAATACGACTCACTATAGGG	53.2 ˚C	-
	T7 term: CTAGTTATTGCTCAGCGGT	54.5 ˚C	-

Primer set for HB-EGF expression

HB-EGF	HBEGFF : 5'-TTATCCTCCAAGCCACAAGC-3'	60 ˚C	200
	HBEGFR : 5'-CCCATGACACCTCTCTCCAT-3'		

Table. A8. List of Antibiotic

Name	Stock Conc.(mg/ml)	Solvent	Working Conc.(µg/ml)
Ampicillin	100	Water	100

Publications

1. **Agarwal M**, Sahoo AK, Bose B. Receptor-Mediated Enhanced Cellular Delivery of Nanoparticles Using Recombinant Receptor-Binding Domain of Diphtheria Toxin. Mol Pharm. 2017, 14(1):23-30.

2. **Agarwal M**, Mondal T, Bose B. Peptides Derived From A Short Stretch of The Receptor-Binding Domain of Diphtheria Toxin Bind To Its Receptor. (Manuscript submitted, currently under review)

Abstract:

1. **Agarwal M**, Bose B. Identification, Interactions and Biological Activities of Receptor-Binding Peptides Derived from Diphtheria Toxin. Research Conclave-2018, IIT Guwahati, India, March, 2018.

2. **Agarwal M**, Mondal T, Bose B. Identification of a Receptor-Binding Peptide Derived from Diphtheria Toxin. ISCBC-2018, Manipal University Jaipur, Rajasthan, India, January, 2018.

3. **Agarwal M,** Sahoo AK, Bose B. Synthesis and characterization of PLGA Nanoparticles for targeted drug delivery. ICSIMR-2017, IIT Guwahati, India, June, 2017.

4. **Agarwal M,** Sahoo AK, Bose B. Receptor binding domain of Diphtheria toxin for targeted delivery of Nanoparticles. ICETINN-2017, SMIT, Sikkim, India, March, 2017.

5. **Agarwal M,** Sahoo AK, Bose B. Diphtheria toxin-derived protein for targeted delivery of nanoparticles. ICONAN-2016, University Pierre and Marie Curie, Paris, France, September, 2016.